J. Fluid Mech. (2014), *vol.* 753, *pp.* 150–216.
doi:10.1017/jfm.2014.335

Numerical simulation of sand waves in a turbulent open channel flow

Ali Khosronejad and Fotis Sotiropoulos†

Saint Anthony Falls Laboratory, and Department of Civil Engineering, University of Minnesota, Minneapolis, MN 55414, USA

(Received 13 December 2013; revised 7 June 2014; accepted 9 June 2014; first published online 18 July 2014)

We develop a coupled hydro-morphodynamic numerical model for carrying out large-eddy simulation of stratified, turbulent flow over a mobile sand bed. The method is based on the curvilinear immersed boundary approach of Khosronejad *et al.* (*Adv. Water Resour.*, vol. 34, 2011, pp. 829–843). We apply this method to simulate sand wave initiation, growth and evolution in a mobile bed laboratory open channel, which was studied experimentally by Venditti & Church (*J. Geophys. Res.*, vol. 110, 2005, F01009). We show that all the major characteristics of the computed sand waves, from the early cross-hatch and chevron patterns to fully grown three-dimensional bedforms, are in good agreement with the experimental data both qualitatively and quantitatively. Our simulations capture the measured temporal evolution of sand wave amplitude, wavelength and celerity with good accuracy and also yield three-dimensional topologies that are strikingly similar to what was observed in the laboratory. We show that near-bed sweeps are responsible for initiating the instability of the initially flat sand bed. Stratification effects, which arise due to increased concentration of suspended sediment in the flow, also become important at later stages of the bed evolution and need to be taken into account for accurate simulations. As bedforms grow in amplitude and wavelength, they give rise to energetic coherent structures in the form of horseshoe vortices, which transport low-momentum near-bed fluid and suspended sediment away from the bed, giving rise to characteristic 'boil' events at the water surface. Flow separation off the bedform crestlines is shown to trap sediment in the lee side of the crestlines, which, coupled with sediment erosion from the accelerating flow over the stoss side, provides the mechanism for continuous bedform migration and crestline rearrangement. The statistical and spectral properties of the computed sand waves are calculated and shown to be similar to what has been observed in nature and previous numerical simulations. Furthermore, and in agreement with recent experimental findings (Singh *et al.*, *Water Resour. Res.*, vol. 46, 2010, pp. 1–10), the spectra of the resolved velocity fluctuations above the bed exhibit a distinct spectral gap whose width increases with distance from the bed. The spectral gap delineates the spectrum of turbulence from the low-frequency range associated with very slowly evolving, albeit energetic, coherent structures induced by the migrating sand waves. Overall the numerical simulations reproduce the laboratory observations with good accuracy and elucidate the physical phenomena governing the interaction between the turbulent flow and the developing mobile bed.

Key words: computational methods, geophysical and geological flows, sediment transport

† Email address for correspondence: fotis@umn.edu

1. Introduction

In fluvial and coastal environments, sediment transport processes induced by energetic coherent structures in a turbulent boundary layer developing over a mobile sediment bed result in the formation of different types of sand waves or bedforms, which can grow and migrate. Such bed features, which also occur in aeolian sediment transport by the atmospheric boundary layer (Nishimori & Ouchi 1993), are dynamically rich and topologically complex and occur across a wide range of scales and flow regimes. Depending on their size, sand waves can be classified into three broad categories: (i) large-scale dunes and bars with amplitudes $\Delta \sim O(1\ \mathrm{m})$ and wavelength $\lambda \sim O(10\ \mathrm{m})$; (ii) intermediate-scale bedforms with $\Delta \sim O(0.1\ \mathrm{m})$ and $\lambda \sim O(1\ \mathrm{m})$; and (iii) small-scale ripples with $\Delta \sim O(0.01\ \mathrm{m})$ and $\lambda \sim O(0.1\ \mathrm{m})$. This classification is based on the analysis of bedforms observed in various environments, including: small-scale experimental flumes (e.g. Seminara, Colombini & Parker 1996; Hansen *et al.* 2001; Venditti & Bauer 2005; Venditti & Church 2005; Venditti, Church & Bennett 2005*a*,*b*, 2006; Raudkivi 2007; Chou & Fringer 2010; Dreano *et al.* 2010; Escauriaza & Sotiropoulos 2011*a*); mid-size streams (e.g. Lacy *et al.* 2007; Kang *et al.* 2011; Palmsten *et al.* 2011); and large rivers in nature (e.g. van Rijn 1993; Venditti & Bauer 2005; Nittrouer, Allison & Campanella 2008; Nittrouer, Mohrig & Allison 2011). The study of sand wave dynamics in fluvial environments has been the subject of intense research over many decades (Kennedy 1969; Fredsoe 1974; Jain & Kennedy 1974). Studies have sought to understand the fundamental mechanisms that lead to the initiation of sand wave formation (Besio, Blondeaux & Vittori 2006) and to elucidate the profound impact that migrating bedforms have on the turbulent flow and sediment transport processes that create them. The latter become especially apparent during flooding events, during which bedform migration provides the primary mechanism for transporting large amounts of sediment through riverine systems (Blondeaux 2001), impacting both the morphology and ecology of waterways (MacVicar, Parrott & Roy 2006). The continuous migration of bedforms gives rise to a turbulent open channel flow over a bed with dynamically evolving roughness. The evolving shape of the sediment–water interface gives rise to low-frequency, albeit very energetic, coherent structures (van Rijn 1993; Hansen *et al.* 2001; Venditti & Church 2005; Dreano *et al.* 2010), and leaves a distinct and persistent signature in the flow velocity spectra in the form of a spectral gap that delineates the spectrum of turbulence from that of slowly evolving energy-containing eddies associated with bedform migration (Singh, Porté-Agel & Foufoula-Georgiou 2010). In spite of significant recent progress, however, many of the complex flow, sediment transport and bed morphodynamic phenomena associated with the initiation, growth and migration of bedforms remain poorly understood. This paper seeks to advance fundamental understanding of these phenomena by reporting and analysing the results of a high-fidelity coupled hydro-morphodynamic large-eddy simulation (LES) of turbulent open channel flow over a mobile sand bed.

Because of the complexity of the problem, most of what we know today about the coupled interaction of a turbulent flow with a mobile bed has been derived from laboratory experiments and field studies (e.g. Raudkivi 1966; Allen 1968, 1971; Hino 1968; van Rijn 1984, 1993; Gyr & Schmid 1989; Khelifa & Ouellet 2000; Venditti & Bennett 2000; Hansen *et al.* 2001; Venditti & Church 2005; Venditti *et al.* 2005*a*, 2006; Raudkivi 2007; Mazumder *et al.* 2009; Dreano *et al.* 2010; Sarkar & Dey 2010). Theoretical approaches, relying on linear stability theory, have also contributed important insights into the mechanisms that destabilize an initially flat mobile bed and give rise to sand waves. Such linear models incorporate a

number of simplifying assumptions, which render their results applicable only to microscale sand waves with amplitudes smaller than 1.0 cm. For instance, in their pioneering stability theory-based models, Kennedy (1969), Hayashi (1970) and Jain & Kennedy (1974) assumed quasi-steady potential flow to simulate the bed evolution mechanism of microscale sand ripples. Others, including Fredsoe (1974), Richards (1980), Coleman & Fenton (2000), Colombini (2004), Coleman *et al.* (2006) and Colombini & Stocchino (2012), have also used a similar modelling framework to analyse microscale ripples. The assumptions inherent in linear stability models are valid only during the initial stages of sand wave formation during which the amplitude of sand waves is very small and rolling of sediment particles within the bedload layer is the major mechanism for transporting sediment and destabilizing the initially flat bed. This initial period, however, is very brief compared to the time scale of a typical bedform life cycle. Once the initiated sand waves grow sufficiently in wavelength and amplitude, increased shear stress due to flow acceleration over crestlines along the stoss side coupled with flow separation off the lee side of crestlines provide the primary mechanisms for continuous particle entrainment and deposition, leading to the evolution of the geometry of sand waves. Naturally, as soon as this state emerges, the validity of linear models breaks down (Chou & Fringer 2010). Based on the simulation results we will report in this work, and also in experimental and analytical findings (see e.g. Venditti & Church 2005; Andreotti *et al.* 2011; Niemann, Fredsøe & Jacobsen 2011; Charru, Andreotti & Claudin 2013; de Moraes Franklin 2013), the initial stage occurs during the first few minutes of the process, while the sand wave life cycle, depending on the availability of bed material, flow condition and waterway condition, can last up to hours and even days.

With increasing computing power and advances in computational fluid dynamics (CFD) algorithms, it has now become possible to computationally investigate turbulent flows over sand waves. Existing computational models can be broadly classified into two groups: (i) decoupled models that simulate the turbulent flow over synthetic stationary sand waves; and (ii) coupled, hydro-morphodynamic models that can simulate the co-evolution of turbulence, sediment transport and bedform growth and migration in open channels. Decoupled models, which employ direct numerical simulation (DNS), LES, or Reynolds-averaged Navier–Stokes (RANS) models, have been extensively applied to investigate the dynamics of turbulent flow over stationary sand wave geometries (Blondeaux & Vittori 1991; Angelis, Lombardi & Banerjee 1997; Henn & Sykes 1999; Scandura, Vittori & Blondeaux 2000; Zedler & Street 2001, 2006; Chang & Scotti 2003, 2004; Barr *et al.* 2004; Best 2005; Yue, Lin & Patel 2005; Zou, Liu & Lu 2006). Recently, Chau & Bhaganagar (2012) carried out a DNS to simulate the turbulent flow over mobile microscale sand waves that were randomly generated, whereas Nabi *et al.* (2012) carried out LES of turbulent flow over frozen two-dimensional (2D) and three-dimensional (3D) dunes (see also Giri & Shimizu 2006, 2007). In the most recent of such studies, Omidyeganeh & Piomelli (2013*a*,*b*) also performed a LES to investigate the formation and downstream transport of vortical structures over a series of frozen 3D dunes at laboratory scale. Although simulations of turbulent flow over stationary bedforms have yielded significant insights into the dynamics of coherent structures that emerge as the turbulent flow interacts with the complex bed shape, such studies are inherently incapable of simulating phenomena associated with the coupled interactions between the emerging, growing and migrating sand waves and the turbulent flow.

There are several numerical investigations attempting to simulate sand wave evolution using RANS models (e.g. Roulund *et al.* 2005; Tjerry & Fredsøe 2005;

Niemann *et al.* 2011). However, to our knowledge, only two studies have employed LES to undertake a fully coupled numerical simulation of the underlying hydro-morphodynamic processes that give rise to sand waves. Chou & Fringer (2010) employed an arbitrary Lagrangian–Eulerian (ALE) scheme to simulate small-scale ripples ($O(\leqslant 2$ cm)) arising in an open channel as a result of the action of a turbulent oscillatory flow induced by waves. They carried out LES, solving the spatially filtered Boussinesq equations to account for local stratification effects that arise in the sediment–water mixture. Their model incorporated both suspended sediment transport, with a pick-up function at the sediment–water interface for sediment entrainment, as well as transport in the bedload layer, by solving a mass-balance equation to simulate the instantaneous bed elevation field. Chou & Fringer (2010) demonstrated good agreement between the computed and measured sand wave characteristics and elucidated the impact of the migrating sand waves on the near-bed coherent structures in the turbulent boundary layer. They also showed that taking into account density stratification effects is a critical prerequisite for bedforms to emerge in their simulations. They argued that this is because neglecting stratification yields spuriously high levels of near-bed turbulence, which effectively acts to destroy the bedload layer within which ripples will first originate. In another study, Escauriaza & Sotiropoulos (2011*a*) also employed the ALE technique to simulate the initial stages of microscale sand wave ($O(\leqslant 1$ cm)) dynamics inside the scour hole that grows around a cylinder mounted on a mobile sand bed. They used detached eddy simulation (DES), a hybrid RANS–LES method, to resolve the dynamics of the turbulent horseshoe vortex at the junction of the cylinder with the bed, which initiates sediment transport for this case under clear-water conditions. Their model included only bedload sediment transport by solving the Exner equation coupled with the flow to simulate the evolution of the bed and naturally could not account for stratification effects. Escauriaza & Sotiropoulos (2011*b*), however, proposed and employed in their model a new transport equation for calculating the distribution of the instantaneous velocity field of computational sediment particles within the bedload layer derived from Lagrangian considerations and incorporating most of the relevant forces imparted on the sediment grains by the fluctuating turbulent flow in the vicinity of the bed. They showed that in their simulation small-scale ripples appear spontaneously at approximately the same time as observed in laboratory experiments (Dargahi 1990), grow and merge to form larger slowly travelling sand waves that migrate continuously with speeds also similar to the experimental observations (Dargahi 1989, 1990). Escauriaza & Sotiropoulos (2011*a*) analysed the statistical properties of the calculated sand waves and showed that they exhibit all the features of sand waves occurring in nature, including, among other things, the f^{-1} rate of decay in the spectra of bed elevation fluctuations. A limitation of the studies of both Chou & Fringer (2010) and Escauriaza & Sotiropoulos (2011*a*) is that they employ the ALE formulation, which requires that the grid conforms to the boundary shape at all times. This requirement restricts the application of such methods to simulations of small-amplitude bedforms for which the mesh deformation remains small at all times.

In a very recent work, Kidanemariam & Uhlmann (2014) carried out DNS of flow over a thick bed of mobile spherically shaped particles, resolving particle–particle and particle–flow interactions, and were able to simulate realistic small-scale sand waves (amplitudes of $O(\sim 2$ mm)) from first principles. This approach, however, is computationally very costly (Kidanemariam & Uhlmann 2014) and not feasible for simulating high-Reynolds-number flows and long-term evolution of large-amplitude bedforms.

In this paper, we report a new numerical method, which is able to carry out LES of bed morphodynamics in turbulent open channel flows and to simulate bedforms of arbitrarily large amplitude. We subsequently demonstrate that this method can yield results that are quantitatively and qualitatively similar to experimental observations, and we provide insights into the physics of bed evolution and associated impact on the turbulent flow that drives sand wave formation that go considerably beyond what can be documented experimentally.

We develop a fully coupled hydro-morphodynamic formulation, which is based on the curvilinear immersed boundary (CURVIB) framework of Khosronejad *et al.* (2011), Khosronejad, Kang & Sotiropoulos (2012) and Khosronejad *et al.* (2013), and is able to carry out LES of stratified turbulent flows in arbitrarily complex domains under live-bed sediment transport conditions incorporating both suspended load and bedload sediment transport processes. The dynamically evolving geometry of the sediment–water interface is simulated by solving the non-equilibrium sediment mass-balance equation (Khosronejad *et al.* 2011) coupled with the near-bed velocity fluctuations resolved by the LES. The hydrodynamic module of the proposed method has undergone extensive validation by applying it to carry out LES of turbulent flow through a rigid-bed natural meandering stream (Kang *et al.* 2011; Kang & Sotiropoulos 2011, 2012). The coupled hydro-morphodynamic model has been validated under clear-water sediment transport conditions by carrying out LES of turbulent flow through a mobile bed straight laboratory flume with various in-stream rock structures (Khosronejad *et al.* 2013). In this work, we apply our computational model to carry out LES of turbulent flow and sand wave dynamics in a straight laboratory flume with a mobile sand bed, which was studied experimentally by Venditti & Church (2005) and Venditti *et al.* (2005*b*). The specific test case is selected because it presents one of the most well-documented experiments of sand wave dynamics under the action of a turbulent open channel flow, including quantitative experimental measurements that allow for the comprehensive characterization of the spatio-temporal characteristics of the sand waves during various stages of their evolution. Namely, the experiments of Venditti and co-workers have documented and quantified the very early stages of sand wave formation, their subsequent growth and organization to form 2D ripples, and their transition into a 3D state, which is accompanied by the emergence of sand waves of complex, multi-connected topology. We carry out simulations on four successively finer grids, with total grid nodes ranging from 22 to 80 million, and show that our numerical simulations resolve most features of the experiments both qualitatively and quantitatively. We further analyse the simulated flow fields in tandem with the evolving sand waves to elucidate the complex physics of the problem, and gain new physical insights into the mechanisms that govern the coupled interaction of the turbulent flow with the initiating and subsequently migrating sand waves.

This paper is organized as follows. First, we introduce briefly the hydrodynamic and morphodynamic models, followed by the description of the coupling approach that we employ. Subsequently, we present the hydrodynamic and morphological results of the simulated sand waves and compare them with the laboratory experiments of Venditti & Church (2005) and Venditti *et al.* (2005*b*). Then we analyse the calculated instantaneous and time-averaged flow fields and discuss the physics of the flow as it emerges from our simulations. Next, we report a statistical analysis of flow and bed fluctuations and link our findings with the dynamics of the resolved sand waves and flow structures. Finally, we summarize the main contribution and conclusions from this work and discuss areas for future research.

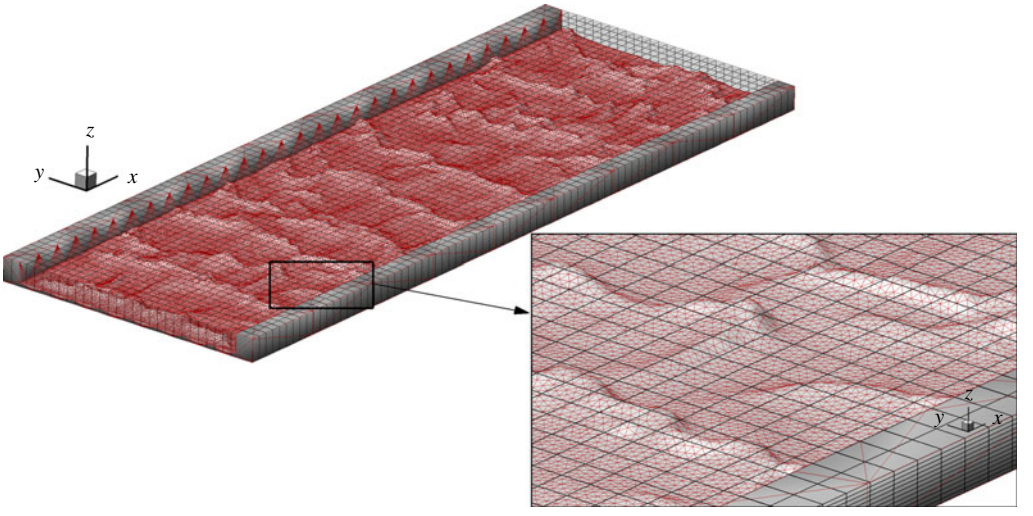

FIGURE 1. (Colour online) Schematic of the proposed CURVIB approach. The channel side walls and mobile bed are discretized with an unstructured triangular mesh and treated as a sharp-interface immersed body embedded in the background domain discretized with a structured curvilinear mesh. For the simulations reported in this paper, the background grid is non-uniform and Cartesian, but the ability of the method to handle curvilinear domains facilitates the simulation of bedforms in meandering channels. The nodes of the structured curvilinear mesh located in the sediment layer and side walls are blanked out of the simulation.

2. The coupled hydro-morphodynamic model

2.1. *The hydrodynamic model*

We consider incompressible stratified turbulent flow of dilute water–sediment mixture, which is governed by the spatially filtered (for LES) continuity and Navier–Stokes equations with the Boussinesq assumption to account for density variations due to the suspended sediment concentration in the water column. In the CURVIB method that we employ herein (see figure 1), the governing equations are first written in Cartesian coordinates $\{x_i\}$ and then transformed fully (both the velocity vector and spatial coordinates are expressed in curvilinear coordinates) in non-orthogonal generalized curvilinear coordinates $\{\xi^i\}$ (Ge & Sotiropoulos 2007). The transformed equations read in compact tensor notation (repeated indices imply summation) as follows $(i, j, k, l = 1, 2, 3)$:

$$J\frac{\partial U^j}{\partial \xi^j} = 0, \tag{2.1}$$

$$\frac{1}{J}\frac{\partial U^i}{\partial t} = \frac{\xi_l^i}{J}\left(-\frac{\partial}{\partial \xi^j}(U^j u_l) + \frac{1}{\rho_o}\frac{\partial}{\partial \xi^j}\left(\mu\frac{\boldsymbol{G}^{jk}}{J}\frac{\partial u_l}{\partial \xi^k}\right) - \frac{1}{\rho_o}\frac{\partial}{\partial \xi^j}\left(\frac{\xi_l^j p}{J}\right) - \frac{1}{\rho_o}\frac{\partial \boldsymbol{\tau}_{lj}}{\partial \xi^j} + \frac{\overline{\rho}-\rho_o}{\rho_o}g\left(\frac{\delta_{i3}}{J}\right)\right), \tag{2.2}$$

where $J = |\partial(\xi^1, \xi^2, \xi^3)/\partial(x_1, x_2, x_3)|$ is the Jacobian of the geometric transformation, x_3 is the vertical coordinate, $\xi_l^i = \partial \xi^i/\partial x_l$ are the transformation metrics, u_i is the

ith Cartesian velocity component, $U^i = (\xi^i_m/J)u_m$ is the contravariant volume flux, $\boldsymbol{G}^{jk} = \xi^j_l \xi^k_l$ are the components of the contravariant metric tensor, p is the pressure, μ is the dynamic viscosity, $\boldsymbol{\tau}_{ij}$ is the subgrid stress tensor for the LES model, ρ_o is the background density (the density of water in our case), $\overline{\rho}$ is the density of the sediment–water mixture, g is the gravitational acceleration and δ is the Kronecker delta. The density of the sediment–water mixture $\overline{\rho}$ is modelled as

$$\overline{\rho} = \rho_o(1-\psi) + \rho_s\psi, \tag{2.3}$$

where ψ is the volume fraction of suspended sediment concentration and ρ_s is the density of sediment particles. The volume fraction of suspended sediment ψ is calculated by solving an advection–diffusion equation for the suspended sediment, which is described in the subsequent section. The sediment particles in suspension are assumed to have negligible effect on the momentum of fluid flow, which is a common assumption in the Eulerian framework of simulating flow and low-concentration sediment particles (see Wu, Rodi & Wenka 2000; Chang & Scotti 2004; Zedler & Street 2006; Chou & Fringer 2010). However, the impact of the stratification and bulk of suspended sediment material on the resolved flow field is taken into account with the Boussinesq term in the momentum equation (the last term on the right-hand side of (2.2)). The subgrid-scale (SGS) stresses are modelled using the dynamic Smagorinsky model (Smagorinsky 1963; Germano *et al.* 1991),

$$\boldsymbol{\tau}_{ij} - \tfrac{1}{3}\boldsymbol{\tau}_{kk}\delta_{ij} = -2\mu_t\overline{\boldsymbol{S}_{ij}}, \tag{2.4}$$

$$\mu_t = C_s\Delta^2|\overline{\boldsymbol{S}}|, \tag{2.5}$$

where the overbar denotes the grid filtering operation, $\overline{\boldsymbol{S}_{ij}}$ is the filtered strain-rate tensor, μ_t is the eddy viscosity, C_s is the Smagorinsky constant, Δ is the filter size and $|\overline{\boldsymbol{S}}| = \sqrt{2\overline{\boldsymbol{S}_{ij}}\,\overline{\boldsymbol{S}_{ij}}}$. The box filter (Sagaut 1988) is employed in the present model, which is given as follows:

$$\Delta = J^{-1/3}. \tag{2.6}$$

In the above equation, J^{-1} represents the cell volume, and the filter size is taken as the cubic root of the cell volume. We employ the dynamic Smagorinsky model (Smagorinsky 1963) as a subgrid model in which the model constant C_s evolves in time and space as a function of the flow field. The optimal value of C_s is selected to minimize the mean square error between the resolved stress at the grid filter and the test filter as follows (Germano *et al.* 1991):

$$C_s = \frac{\langle L_{ij}M_{ij}\rangle}{\langle M_{kl}M_{kl}\rangle}, \tag{2.7}$$

where

$$L_{ij} = \widehat{\overline{u_i}\,\overline{u_j}} - \widehat{\overline{u}_i}\,\widehat{\overline{u}_j}, \tag{2.8}$$

$$M_{ij} = 2\Delta^2\widehat{\overline{\boldsymbol{S}_{ij}}|\overline{\boldsymbol{S}}|} - 2\widehat{\Delta}^2\overline{\boldsymbol{S}_{ij}}|\widehat{\overline{\boldsymbol{S}}}|. \tag{2.9}$$

In the above equations, $\widehat{\Delta}$ is the size of the test filter, which is twice as large as the grid filter for uniform grids, and the $\widehat{\ }$ denotes the test filtering, which in three dimensions involves the 27 grid nodes surrounding a given grid node. Here, $\langle\ \rangle$ indicates averaging in the homogeneous directions implying the direction where

the periodic boundary condition is employed. For problems with no homogeneous direction present (fully 3D cases), this averaging can be replaced by local averaging around a grid node. In the present numerical implementation of the above SGS model, the Smagorinsky constant and the eddy viscosity are computed at the centre of the cell using (2.7) and (2.5), respectively, at the beginning of each time step. Subsequently, the eddy viscosity is interpolated from the cell centre to the cell face and it is used to calculate the SGS terms in (2.4) (for more details see Kang & Sotiropoulos 2011).

In accordance with the CURVIB formulation (Kang *et al.* 2011; Khosronejad *et al.* 2011), we employ wall functions to reconstruct boundary conditions for the resolved velocity components at grid nodes located near rigid walls and the mobile sediment–water interface as follows:

$$\frac{u}{u_*} = \begin{cases} y^+ & y^+ \leqslant y_o^+, \\ \dfrac{1}{\kappa}\ln(Ey^+) & y^+ > y_o^+, \end{cases} \tag{2.10}$$

where u is the velocity magnitude at the nearest node to the wall boundary (located at distance y from the wall), y^+ $(= yu_*/\nu)$ is the non-dimensional distance from the wall in wall units, u_* is the shear velocity, κ is the von Kármán constant, $y_o^+ = 11.53$ and E is the roughness parameter, which is related to the roughness Reynolds number $k_s^+ = u_* k_s/\nu$ as (Khosronejad *et al.* 2011)

$$E = \exp[\kappa(B - \Delta B)], \tag{2.11}$$

where k_s is the effective roughness height of the wall boundary and $B = 5.2$. Here, ΔB is a function that depends on the bed roughness and is formulated in terms of the roughness Reynolds number as follows (Khosronejad *et al.* 2011):

$$\Delta B = \begin{cases} 0 & k_s^+ < 2.25, \\ \left[B - 8.5 + \dfrac{1}{\kappa}\ln(k_s^+)\right]\sin[0.4258(\ln k_s^+ - 0.811)] & 2.25 < k_s^+ < 90, \\ B - 8.5 + \dfrac{1}{\kappa}\ln(k_s^+) & k_s^+ \geqslant 90. \end{cases} \tag{2.12}$$

For hydraulically smooth wall boundaries, k_s^+ is less than 2.25, and based on (2.12) the roughness function ΔB is zero. For a stationary flat bed covered with sand material with median grain size d_{50}, k_s is assumed to be equal to d_{50} (Wu *et al.* 2000). In practice, however, for mobile beds, somewhat higher values are adopted (Wu *et al.* 2000). In the present simulations, we employ a value of $k_s = 3d_{50}$ for the mobile beds and treat the stationary rock structures and side walls as hydraulically smooth surfaces.

The details of the numerical method for solving numerically the hydrodynamic governing equations have already been documented extensively elsewhere (Ge & Sotiropoulos 2007; Borazjani, Ge & Sotiropoulos 2008; Kang *et al.* 2011; Kang & Sotiropoulos 2011) and only a brief summary of the key elements of the method will be given here.

The governing equations are discretized in space on a hybrid staggered/non-staggered grid arrangement using second-order accurate central differencing for the convective terms along with second-order accurate, three-point central differencing for the divergence, pressure gradient and viscous-like terms (Gilmanov & Sotiropoulos

2005; Ge & Sotiropoulos 2007). The time derivatives are discretized using second-order backward differencing (Kang *et al.* 2011).

The discrete equations are integrated in time using an efficient second-order accurate fractional step methodology coupled with a Jacobian-free Newton–Krylov solver for the momentum equations and a GMRES solver enhanced with multi-grid method as preconditioner for the Poisson equation. For additional details, the reader is referred to Ge & Sotiropoulos (2007), Borazjani *et al.* (2008), Kang *et al.* (2011) and Kang & Sotiropoulos (2011).

Geometrically complex computational domains are handled using the sharp-interface CURVIB method (Ge & Sotiropoulos 2007). For the present case, the computational domain is a straight open channel that outlines the actual channel under consideration and is sufficiently deep to contain the entire sediment–water interface at all times. The computational domain is discretized with a boundary-fitted Cartesian (or curvilinear for curved channels) mesh, while the sediment–water interface and channel side walls are discretized with an unstructured grid, which is immersed in the background domain and treated as sharp interfaces in accordance with the CURVIB formulation. The governing equations are solved at the background grid nodes in the fluid phase (fluid nodes) with boundary conditions specified at fluid nodes in the immediate vicinity of the sediment–water interfaces (denoted as immersed boundary (IB) nodes). All nodes inside the sediment layer are blanked out from the computations. Boundary conditions for the velocity components, turbulence quantities and sediment concentration are reconstructed at all IB nodes using the wall functions presented above implemented in a manner consistent with the CURVIB method (Kang *et al.* 2011; Khosronejad *et al.* 2011).

A critical issue for the successful application of the CURVIB method to problems with moving IBs is the efficient classification of the background grid nodes into fluid, IB and external nodes whenever the shape and/or location of the IB are modified as the evolving sand waves migrate. Herein we employ the efficient ray-tracing algorithm developed by Borazjani *et al.* (2008) to re-classify the grid nodes every time the bed shape and location are updated.

The flow solver is also fully parallelized using the message passing interface (MPI) communication standard to run on parallel high-performance clusters.

2.2. *Suspended sediment transport equation*

For dilute sediment–water mixture (the volumetric sediment concentration does not exceed $O(0.01)$), the suspended sediment is modelled as an active scalar whose transport is governed by the following advection–diffusion equation (e.g. Wu *et al.* 2000; Zedler & Street 2001, 2006; Chou & Fringer 2008, 2010; Kraft, Wang & Oberlack 2011):

$$\frac{1}{J}\frac{\partial(\rho\psi)}{\partial t}+\frac{\partial}{\partial\xi^j}(\rho\psi(U^j-W^j\delta_{i3}))=\frac{\partial}{\partial\xi^j}\left((\mu+\sigma^*\mu_t)\frac{G^{jk}}{J}\frac{\partial\psi}{\partial\xi^k}\right), \tag{2.13}$$

where $W^j=(\xi_3^j/J)w_s$ is the contravariant volume flux of suspended sediment, σ^* is the Schmidt number ($=0.75$) (Khosronejad 2006; Khosronejad, Salehi & Rennie 2008) and w_s is the settling velocity of non-spherical sediment particles, which is computed

by van Rijn's formula (van Rijn 1993):

$$w_s = \begin{cases} \dfrac{(\rho_s - \rho_o) g d_{50}}{18\mu} & 1 < d_{50} < 100\ \mu\text{m}, \\ \dfrac{10\nu}{d_{50}} \left\langle \left(1 + \dfrac{0.01\left(\dfrac{\rho_s}{\rho_o} - 1\right) g d_{50}^3}{\nu^2} \right)^{1/2} - 1 \right\rangle & 100 < d_{50} < 1000\ \mu\text{m}, \\ 1.1 \left\langle \left(\dfrac{\rho_s}{\rho_o} - 1 \right) g d_{50} \right\rangle^{1/2} & d_{50} \geqslant 1000\ \mu\text{m}, \end{cases} \tag{2.14}$$

where d_{50} is the median sediment particle size and ν is the kinematic viscosity of water.

At the mobile sediment–water interface, we employ the approach proposed by Chou & Fringer (2008) to specify boundary conditions for ψ using van Rijn's pick-up function (van Rijn 1993). At rigid walls and the outlet of the flow domain, we employ a Newman zero-gradient boundary condition, while for the free surface boundary we assume no-mass flux condition as follows (van Rijn 1993):

$$w_s \psi + (\mu + \sigma^* \mu_t) \frac{\partial \psi}{\partial x_3} = 0. \tag{2.15}$$

Third-order weighted essentially non-oscillatory (WENO) (Jiang & Shu 1996) and second-order central differencing schemes are employed for the spatial discretization of advection and diffusion terms in the sediment concentration transport equation (2.13), respectively. Additionally, the second-order backward differencing scheme is used for the time integration. The sediment concentration equation is solved using the fully implicit Jacobian-free Newton's method at every time step after the velocity fields are obtained by the fractional step method (for more details see Kang *et al.* 2011).

2.3. *Bed morphodynamics model*

In this section we outline the mathematical equations that govern the temporal variation of the mobile sediment–water interface and describe the numerical method that we have developed for solving them. Our numerical methodology under equilibrium conditions has been described in detail in Khosronejad *et al.* (2011), and thus only a brief description of the numerical formulation under non-equilibrium conditions and for live-bed sediment transport is given herein.

Under live-bed conditions sediment transport occurs as both suspended load and bedload. Bedload transport occurs within the bedload layer (i.e. a layer of thickness $\|\boldsymbol{\delta}_{BL}\|$ set to $2d_{50}$ immediately above the bed), while the suspended load is advected by the flow and interacts with the bedload layer. This interaction occurs in the form of sediment particle entrainment and deposition from and into the bed surface, respectively, across the sediment–water interface (see face '*S*' in figure 2). The temporal variation of the bed elevation is governed by the following non-equilibrium sediment continuity equation, the so-called Exner–Polya equation (Paola & Voller 2005):

$$(1 - \gamma) \frac{\partial z_b}{\partial t} + \boldsymbol{\nabla} \cdot \boldsymbol{q}_{BL} = D_b - E_b, \tag{2.16}$$

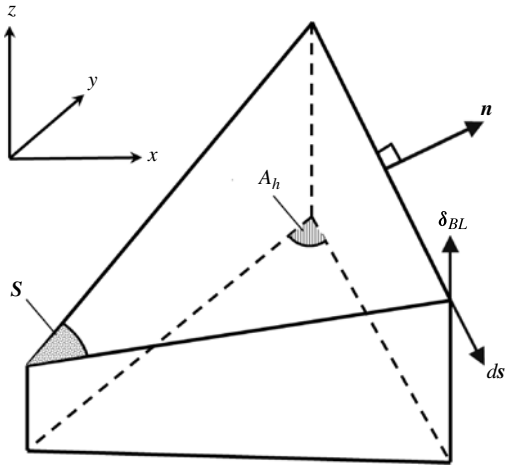

FIGURE 2. Schematic of a triangular element in the bedload layer and definition of the cell area (A_h), top face (S) and unit normal vector ($\boldsymbol{n}$).

where γ is the sediment material porosity, z_b is the bed elevation, ∇ denotes the divergence operator, $\boldsymbol{q}_{BL}$ is the bedload flux vector, D_b is the net deposition onto the bed and E_b is the net entrainment from the bed cell.

In the CURVIB method, the sediment–water interface is discretized with an unstructured triangular grid and (2.16) is discretized and solved using a finite volume method suitable for unstructured grids. Using the divergence theorem, the left-hand side of (2.16) can be discretized at a given triangular element on the bed as follows (Khosronejad *et al.* 2011):

$$(1-\gamma)\frac{\Delta z_b}{\Delta t}+\frac{1}{A_h}\sum_{i_e=1,2,3}[\boldsymbol{q}_{BL}\cdot(d\boldsymbol{s}\times\boldsymbol{\delta}_{BL})]_{i_e}=(1-\gamma)\frac{\Delta z_b}{\Delta t}+\frac{1}{A_h}\sum_{i_e=1,2,3}[\boldsymbol{q}_{BL}\cdot\boldsymbol{n}]_{i_e}, \quad (2.17)$$

where Δz_b is the bed elevation change over time step Δt and A_h is the projection of the triangular bed cell area onto the horizontal plane or horizontal projected area of the cell face. The summation is carried out over the three edges of the triangular element ($i_e = 1, 2, 3$), $d\boldsymbol{s}$ is the vector along a cell edge with length equal to the edge length, $\boldsymbol{\delta}_{BL}$ is the vertical vector along the z-axis with length equal to the bedload layer thickness $\|\boldsymbol{\delta}_{BL}\|$ and $\boldsymbol{n}$ ($= d\boldsymbol{s}\times\boldsymbol{\delta}_{BL}$) is the unit normal vector to the cell face edge (see figure 2 for a schematic description). The bedload flux vector, $\boldsymbol{q}_{BL}$, is calculated as follows (Khosronejad *et al.* 2011):

$$\boldsymbol{q}_{BL}=\psi_b\|d\boldsymbol{s}\|\|\boldsymbol{\delta}_{BL}\|\boldsymbol{u}_{BL}, \quad (2.18)$$

where ψ_b is the local sediment concentration on the bed, $\|d\boldsymbol{s}\|$ is the length of edge i_e and $\boldsymbol{u}_{BL}$ is the flow velocity vector parallel to the bed surface at the edge of the bedload layer. The instantaneous resolved velocity vector and bed shear stress calculated from the hydrodynamic model are projected onto the cell centroid at the edge of the bedload layer by applying the law of the wall (equation (2.10)). The sediment concentration within the bedload layer ψ_b is computed at each cell centre on the bed using the deterministic equation of van Rijn (1993) as follows:

$$\psi_b=0.015\frac{d_{50}}{\delta_b}\frac{T^{3/2}}{D_*^{3/10}}, \quad (2.19)$$

where

$$D_* = d_{50}\left[\frac{(\rho_s-\rho)g}{\rho\nu^2}\right]^{1/3}, \tag{2.20}$$

$$T = \frac{\tau_* - \tau_{*cr}}{\tau_{*cr}}, \tag{2.21}$$

where T is the non-dimensional excess bed shear stress (van Rijn 1993), τ_* is the bed shear stress, which is calculated using the wall model (2.10), and τ_{*cr} is the critical bed shear stress. The critical bed shear stress is computed using Shield's criterion (using the parametrized relation of Shield's curve (van Rijn 1993)) for the flat bed critical bed shear stress (τ_{*c0}) and then corrected for a bed with transverse and longitudinal bed slopes (Khosronejad *et al.* 2007; Chou & Fringer 2010) as follows:

$$\tau_{*cr} = \tau_{*c0}\left[\frac{\sin(\phi+\alpha)}{\sin(\phi)}\right], \tag{2.22}$$

where ϕ is the sediment material's angle of repose and α is defined as the local bed slope at the bed cell centroid. The local bed slope for a fully 3D bed geometry is then calculated along the direction of the bed shear stress vector as follows (Khosronejad *et al.* 2007, 2011):

$$\alpha = \sin^{-1}\left[\frac{u_{1,BL}\sin\alpha_1 + u_{2,BL}\sin\alpha_2}{\sqrt{u_{1,BL}^2 + u_{2,BL}^2}}\right], \tag{2.23}$$

where $u_{i,BL}$ is the velocity component at the top of bedload layer and α_i is the local bed slope along corresponding coordinates ($i = 1, 2$).

Once all the required variables have been computed at the cell centroid, the bedload flux $\boldsymbol{q}_{BL}$ at the cell face is calculated using an appropriate convective scheme. In this study we employed the second-order GAMMA differencing scheme (for more details see Khosronejad *et al.* 2011).

Now we focus our attention on the right-hand side of (2.16), which represents the net flux of sediment across the interface between the flow and the bedload layer. The deposition rate at this interface is modelled as follows (Celik & Rodi 1988):

$$D_b = w_s\overline{\psi}_b, \tag{2.24}$$

where $\overline{\psi}_b$ is the instantaneous sediment concentration immediately above the bedload layer. Since the deposition rate involves sediment materials that are vertically transported from the flow domain onto the bed surface, we use a quadratic interpolation procedure to compute $\overline{\psi}_b$ from the calculated ψ in the flow domain (i.e. IB and fluid nodes immediately above the bedload layer); for more details on the interpolation method see Gilmanov & Sotiropoulos (2005). The entrainment rate is also modelled by assuming equilibrium conditions under which the E_b would be equal to D_b and therefore it reads as follows (Celik & Rodi 1988; van Rijn 1993):

$$E_b = w_s\psi_b. \tag{2.25}$$

Note that the modelled entrainment rate (E_b) in this equation is calculated using the instantaneous bedload concentration (ψ_b) obtained by applying (2.19) at the edge of

the bedload layer. Thus, both the entrainment and deposition rates in the mass-balance equation (2.17) are calculated at the top face of the bed cell (see figure 2) where $z = 2d_{50}$.

Therefore the non-equilibrium sediment continuity equation (2.16) can now be rewritten as

$$(1-\gamma)\frac{\Delta z_b}{\Delta t} + \frac{1}{A_h}\sum_{i_e=1,2,3}[\boldsymbol{q}_{BL}\cdot\boldsymbol{n}]_{i_e} = w_s[\overline{\psi}_b - \psi_b]. \tag{2.26}$$

In order to prevent the bed slope from exceeding the sediment material angle of repose, a mass-conservative sand-slide algorithm has been developed and incorporated (for more details see Khosronejad *et al.* 2011; Khosronejad, Kozarek & Sotiropoulos 2014). After solving the Exner–Polya equation and computing the new bed elevations, the entire bed is swept to identify bed cells at which the maximum bed slope (at the centroid of triangular bed cells) is larger than the angle of repose. The local slope correction procedure of the sand-slide model (see Khosronejad *et al.* 2011 for more details) is then applied only to the identified bed cells. Because a single application of this algorithm may not be sufficient to identify and correct all cells with excess slope, the algorithm is applied iteratively until all slopes are smaller than the material angle of repose. The iterative process is declared converged when the bed cell steepest surface angle is less than or equal to 0.99 of the angle of repose of the bed material. To eliminate bias in the final solution, the iterative algorithm is implemented through successive sweeps of alternating direction, from upstream to downstream and reverse. For most time steps only two to four iterations are required for the sand-slide algorithm to converge. Also it is important to mention that the sudden avalanche of material in regions of steep slopes (e.g. along the steep downslope of sand waves immediately downstream of the sand wave crest), which can dislodge and set in motion a large mass of sediment (Khosronejad *et al.* 2012), is not an instantaneous phenomenon. To be consistent with this physical condition, and as soon as the present sand-slide model activates, within only one time step the whole sediment mass is redistributed over other neighbouring cells until all slopes are smaller than the material angle of repose.

2.4. *Hydro-morphodynamic coupling approach*

To simulate the coupling between the flow and morphodynamics, we employ a partitioned fluid–structure interaction (FSI) approach (Borazjani *et al.* 2008). That is, we partition the problem into the fluid and sediment domains and solve the governing equations for the stratified flow and the bed morphodynamics separately in each domain, accounting for the interaction of the two domains by applying boundary conditions at the sediment–water interface. More specifically, to solve the equations governing the flow, boundary conditions are specified on the bed in terms of the bed surface location, rate of bed elevation change and sediment concentration on the bed. On the other hand, to solve the bed evolution equation (2.16), the velocity components, bed shear stress and sediment concentration from the stratified flow domain are required to calculate: (i) the sediment fluxes on the left-hand side of (2.16), and (ii) the net sediment flux at the interface of stratified flow and bedload layer on the right-hand side of (2.16). For the details of how we prescribe the boundary conditions in the two domains, see Khosronejad *et al.* (2011). In this work, we found that the loose-coupling FSI approach in which the boundary conditions at the sediment–water interface are obtained from the domain solutions from the

previous time level (explicit in time) is robust enough for the problems considered and thus we employ it in all subsequent simulations.

An important aspect of the coupled formulation arises from the need to conserve global mass for the flow at each time step as the bed elevation and consequently the domain geometry change. In order to impose global mass conservation, we calculate the rate of volume change ($\partial\forall/\partial t$) associated with the bed deformation (at each time step). Subsequently we calculate the outlet boundary flux (Q_{out}) such that global mass conservation is satisfied (for more details see Khosronejad *et al.* 2011):

$$Q_{out} = Q_{in} + \partial\forall/\partial t. \tag{2.27}$$

The velocity field at the outlet plane, which is obtained by Newman boundary conditions, is then explicitly corrected to ensure that it yields an outflow flux equal to Q_{out}. Furthermore, the velocity boundary conditions that are reconstructed at the IB nodes adjacent to the evolving mobile bed do not necessarily satisfy global mass conservation, because the discrete continuity equation is not enforced at these nodes. To address this issue at every time step, we also correct the reconstructed velocity boundary conditions at the IB nodes such that the rate of volume change through the entire lower boundary is equal to that imposed by the bed motion $\partial\forall/\partial t$.

The overall loose-coupling stratified flow–bed interaction method that we employed in this study is summarized as follows. Assuming that the bed surface location, rate of bed change, flow and sediment concentration field are known at time level n, the steps are as follows.

(*a*) Compute the flow field at time level $n+1$ by solving the hydrodynamic equations with the known bed position, rate of bed change and ψ from time level n.

(*b*) Compute ψ at time level $n+1$ by solving the sediment concentration equation with the known bed position and flow field from time levels n and $n+1$, respectively.

(*c*) Calculate the boundary conditions, i.e. bedload flux vector and net sediment flux at the sediment–water interface, for the Exner–Polya equation (2.16) from the solution of the flow and sediment concentration field at time level $n+1$ as follows:

  (i) find the bed shear stress, flow velocity components and sediment concentration $\overline{\psi}_b$ at the top of the bedload layer (at a distance of δ_b above the bed). All the interpolated variables are stored at triangle cell centres of the unstructured bed mesh.

  (ii) For the given sediment material, bed shape (at time level n) and flow velocity components (at time level $n+1$), compute the critical bed shear stress using (2.22) and (2.23).

  (iii) Compute the sediment concentration ψ_b at the centre of each triangular cell on the bed using the van Rijn (1993) formula (2.19).

  (iv) Calculate the normal component of the bedload flux at each cell face edge using a conservative formulation.

(*d*) Find the new bed elevation at each cell centre at time level $n+1$ by advancing (2.17) in time using the following first-order forward-in-time discretization scheme:

$$z_b^{n+1} = z_b^n - \frac{\Delta t}{(1-\gamma)A_h} \sum_{i_e=1,2,3} [\boldsymbol{q}_{BL} \cdot \boldsymbol{n}]_{i_e} + \frac{\Delta t w_s}{(1-\gamma)} [\overline{\psi}_b - \psi_b]. \tag{2.28}$$

Once the bed level at the cell centres has been updated, the related bed change for the vertices of a cell are computed by weighted interpolation among neighbouring cells.

(*e*) Apply the sand-slide model to ensure that the local bed slopes nowhere exceed the material angle of repose; for more details on the sand-slide model see Khosronejad *et al.* (2011).

(*f*) Modify the shape of the sediment–water interface and calculate the rate of bed change at the vertices of the cells to provide boundary conditions for the flow field computation at the next time step.

3. Description of the experimental test case

We simulate flow and sediment transport in a straight laboratory flume studied experimentally in a series of papers by Venditti & Church (2005) and Venditti *et al.* (2005*a*,*b*, 2006). These experiments include detailed and systematic observations of sand wave initiation, growth and transition from 2D to 3D geometry, as well as quantitative measurements of the temporal variation of bedform characteristics, such as amplitude, wavelength, celerity and arclength. In this section we present a brief overview of the experimental set-up and flow conditions. The reader is referred to Venditti & Church (2005) and Venditti *et al.* (2005*a*,*b*) for more details.

Venditti & Church (2005) employed a tilting flume with recirculating flow of water and sediment. The flume dimensions were 15.2 m long, 1.0 m wide and 0.3 m deep. A uniformly graded non-cohesive sand material with a median grain size of $d_{50} = 0.5$ mm and grain density of $\rho_s = 2650$ kg m^{-3} was used. Venditti and co-workers carried out five experimental runs under various subcritical turbulent flows ranging from a mean flow velocity of 0.36 to 0.5 m s^{-1} and a flow depth of approximately 0.15 m. In their experiment, Venditti & Church (2005) first flattened the bed and then carefully filled up the flume to 0.152 m of water depth and eventually ramped up the flow rate from 0.0 to a discharge of 0.0759 m^3 s^{-1}. The required time to reach the desired discharge is 60 s (for more details see Venditti *et al.* 2005*b*). Instantaneous images of the evolving bedforms were captured at 10 s time intervals using a high-resolution video camera mounted above the flume and focusing on an observation window that covers an area of 1.0 m (streamwise) $\times$ 0.92 m (spanwise) and centred at $\sim$10.3 m downstream of the channel's inlet. Two acoustic echo sounders were also used to measure the celerity of sand waves. Once the bedforms reach equilibrium (after approximately 1.5 h), the average sand wave amplitude is between 19.7 and 47.7 mm and the average sand wavelength ranges between 0.3 and 1.2 m (Venditti & Church 2005).

It is important to note that the flow discharge in the experimental flume is ramped up from zero to the desirable discharge of 0.0759 m^3 s^{-1} within a time period of 60 s, during which the bed undergoes deformations from flat to a chevron-shaped geometry. In our simulations, we start with flat bed geometry but the initial flow condition corresponds to fully developed turbulent open channel flow pre-computed from a separate LES (see below). This difference in the initial flow conditions between the simulations and the experimental set-up should be kept in mind in the subsequently presented comparisons of the numerical simulations with the experimental observations, as it is responsible for some discrepancies observed during the initial stages of the bed evolution. Finally, it is important to mention that the non-dimensional critical Shield's parameter (van Rijn 1993) for flat bed condition (at the beginning of experiment and simulations) is $\sim$0.031, while the Shield's parameter during the coupled simulation varies between 0.03 and 0.15.

4. Computational details

We simulate the flow condition denoted as Case *A* by Venditti & Church (2005), for which the mean flow depth is 0.152 m and the mean flow velocity is 0.501 m s^{-1}. The corresponding values of the Reynolds number and Froude number, based on the mean flow depth H and the bulk velocity U, are $Re = 75\,936$ and $Fr = 0.411$, respectively (see Venditti & Church 2005 for more details). We carry out coupled hydro-morphodynamic LES of this case using the numerical method described in § 2.3 above. The computational domain is a 3.5 m long rectangular channel with vertical and spanwise dimensions identical to those of the laboratory flume and containing a 10 cm thick sediment layer at its bottom (see figure 1). The bed is treated as rigid for the first 0.5 m from the inlet to enable the implementation of inflow conditions as described below.

At the inlet of the computational domain we prescribe fully turbulent open channel flow, which is obtained by carrying out a separate LES for a rigid-bed channel with identical cross-section and flow conditions as in the experiment and using periodic conditions in the streamwise direction. Once this LES reaches its statistically stationary turbulent condition, we store a sufficiently long sample of the instantaneous velocity fields in order to use them as instantaneous inflow conditions for the coupled hydro-morphodynamic LES. This pre-simulated turbulent inflow is developed over a flat bed and therefore needs to be fed at the inlet, which should be flat. Hence, we assume that the channel inlet for a very short distance is rigid ($\sim$10 cm). This assumption is reasonable, as there are many laboratory experiments in which the initial flume section has been kept flat and rigid (Khosronejad *et al.* 2008, 2012, 2013). The rigid part is usually the transitional distance between the water supply to the flume and the mobile bed part of the flume (downstream of the stilling basin in the channel).

At the downstream end of the domain, the Newman outlet boundary condition is employed for all three velocity components, and suspended sediment concentration. The free surface boundary is treated as a rigid lid, while at the solid side walls and mobile bed the wall functions approach is employed as described in § 2.1. For the mobile bed the effective roughness height is set to $k_s = 3d_{50}$, while for the channel side walls we use $k_s = d_{50}$ (Wu *et al.* 2000). For the bed morphodynamic model, the inflow bedload flux at the inlet is set equal to the outflow bedload flux to emulate the recirculation of sediment material used in the laboratory experiment (Venditti & Church 2005). Boundary conditions for the pressure are not explicitly required in the hybrid staggered/non-staggered grid CURVIB formulation. Newman boundary conditions are employed for the pressure correction variable, however, at all boundaries of the computational domain; for more details, see Ge & Sotiropoulos (2007), Borazjani *et al.* (2008) and Kang *et al.* (2011). We also note that in all our simulations the discrete continuity equation is satisfied to machine zero at every time step. To ensure such level of convergence, we need to have a well-posed discrete Poisson problem, which is ensured by correcting the velocity boundary conditions to satisfy global mass using the procedure we described in § 2.4 above for a domain with a dynamically deforming boundary.

The sediment–water interface is discretized with an unstructured triangular mesh and treated as a dynamically evolving IB using the CURVIB method (Khosronejad *et al.* 2011). The channel, within which the sediment–water interface is immersed, is discretized with a Cartesian grid. To investigate the sensitivity of the computed solutions to grid density, we carry out simulations on four, successively finer, background grid systems, which are denoted as grids A (22.6 million nodes),

	$N_x \times N_y \times N_z$			
	Grid A $1101 \times 281 \times 73$	Grid B $1201 \times 301 \times 85$	Grid C $1353 \times 325 \times 97$	Grid D $1649 \times 429 \times 113$
N_b	7.27×10^4	1.04×10^5	1.51×10^5	2.31×10^5
Δx (m)	2.76×10^{-3}	2.53×10^{-3}	2.25×10^{-3}	1.82×10^{-3}
Δy (m)	3.55×10^{-3}	3.32×10^{-3}	3.08×10^{-3}	2.33×10^{-3}
Δz_{bed} (m)	1.42×10^{-3}	1.08×10^{-3}	8.12×10^{-4}	7.48×10^{-4}
Δz_{fs} (m)	3.05×10^{-3}	2.88×10^{-3}	2.64×10^{-3}	2.52×10^{-3}
Δz^+	40	30	23	20
Δt^*	10^{-2}	8×10^{-3}	5×10^{-3}	2×10^{-3}

TABLE 1. The computational grids and the time steps used for each grid system. Here, N_i and Δi indicate the number of grid nodes and the grid spacing in the i direction, respectively; N_b is the number of nodes used to discretize the unstructured triangular mesh at the sediment–water interface; and t^* is the non-dimensional time defined as $t^* = t(U/H)$. Grid systems are uniform in streamwise (x) and spanwise (y) directions, while they are stretched in the vertical (z) direction. Here, Δz_{bed} is the grid spacing in the vertical direction and in a zone 3.5 cm below and 3.5 cm above the initial flat bed. The vertical grid spacing in the near-bed zone is uniform, while above this zone (which is 11.7 cm thick) it is stretched in the vertical direction with a tanh function. Here, Δz_{fs} is the grid spacing in the vertical direction at the water surface. Thus, the vertical grid spacing varies from a minimum of Δz_{bed} to a maximum of Δz_{fs} at the water free surface. Finally, Δz^+ is the minimum grid spacing in the vertical direction scaled in inner wall units.

B (30.7 million nodes), C (42.7 million nodes) and D (79.9 million nodes); their details are summarized in table 1.

For each background grid (table 1), the grid nodes are spaced uniformly along the streamwise and spanwise directions in order to ensure that the emergence and evolution of sand waves in the simulation are not affected by spatially heterogeneous resolution on the horizontal plane due to aspect ratio effects. In the vertical direction the grid spacing is kept constant within a 7.0 cm deep vertical layer that is centred around the initially flat bed. Above this layer, however, the grid in the remaining 11.7 cm deep outer region is stretched in the vertical direction using the hyperbolic stretching function (see table 1). As required by the CURVIB method (Khosronejad *et al.* 2011), for each grid system the resolution of the unstructured mesh, i.e. the triangular grid that covers the sediment–water interface, is adjusted so that it is consistent with the resolution of the structured background mesh. Also, for each grid system, an appropriate non-dimensional time step ($\Delta t^* = \Delta t(U/H)$) is selected such that the maximum Courant–Friedrichs–Lewy number (CFL) is less than 1.0. Note that such a requirement is dictated by the need for temporal accuracy rather than stability of the numerical approach. The convective and viscous terms in our flow solver are treated implicitly and therefore the algorithm will be stable for $CFL > 1.0$. Large time steps, however, will degrade the accuracy of the resolved flow structures in the LES, and for that we restrict the CFL number on each grid to be less than unity. The parameters of the various grids along with the time step used for each grid are summarized in table 1.

Note that the number of grid nodes along each of the three spatial directions has been increased by $\sim$1.5 from grid A to grid D, which is a reasonable grid refinement for such a complex coupled problem. It is important to mention that

such coupled simulations on very fine grids are extremely expensive, and to the best of our knowledge the coupled simulation on grid D is by far the finest coupled hydro-morphodynamic simulation that has been reported to date. As an indication of the computational requirements, we note that the coupled simulation on grid D required 55 days of execution time on 320 CPUs for simulating 200 s of physical time. For that we have continued the simulations on grid D for only the first 200 s of bed evolution for grid sensitivity analysis.

5. Results and discussion

In this section we discuss the computed results and analyse the physics of the coupled turbulent flow and bed evolution as they emerge from our simulations. We begin by validating our hydrodynamics computations against the flow field measurements of Venditti & Church (2005) over a rigid bed in the same flume they used later for their live-bed measurements. Next we continue by presenting and discussing in detail the evolution of the computed sand waves through the various stages of development as observed by Venditti & Church (2005), from the early instability patterns of the bed to fully grown 2D and 3D migrating sand waves. We also compare various calculated quantitative characteristics of the sand waves, including celerity, wavelength and amplitude, and measures of their degree of topological complexity, with the experimental measurements to show that the simulations reproduce with good accuracy the experimental observations both qualitatively and quantitatively. Subsequently we analyse the calculated instantaneous flow fields in tandem with the bed evolution and discuss a number of novel physical insights that arise from the rich dataset we obtain from the simulation results.

5.1. *Flow field validation for the rigid bed case*

In this section we seek to demonstrate the ability of our method to accurately simulate the mean flow and turbulence characteristics of the fully developed turbulent flow in the rigid open channel in which we subsequently study sand wave dynamics. As mentioned above, such simulations need to be carried out anyway for each of the computational grids that we employ in order to obtain inflow conditions for the coupled LES. Venditti & Church (2005) reported mean flow and turbulence statistics measurements for their rigid bed flume to quantify the state of the flow prior to the start of the bed deformation.

In figure 3 we compare the measured and computed, on all four grids, mean streamwise velocity, primary Reynolds stress and streamwise turbulence intensity profiles at the centre of the channel. It is evident that the two finest grids capture the experimental profiles with good accuracy. The convergence is almost monotonic for all quantities as the grid is refined. As one would anticipate, the turbulence statistics are somewhat more sensitive to grid refinement than the mean flow, but even so the results obtained on the two finest meshes for the turbulence quantities are in good agreement with each other and the measurements.

5.2. *Bed surface morphology*

It is well known that sand wave development takes place in three stages: initiation, growth and migration (Chou & Fringer 2010; Escauriaza & Sotiropoulos 2011*a*). During the initiation stage, sand waves are relatively small features of the bed and are mostly composed of linear striations with an amplitude of approximately $2d_{50}$

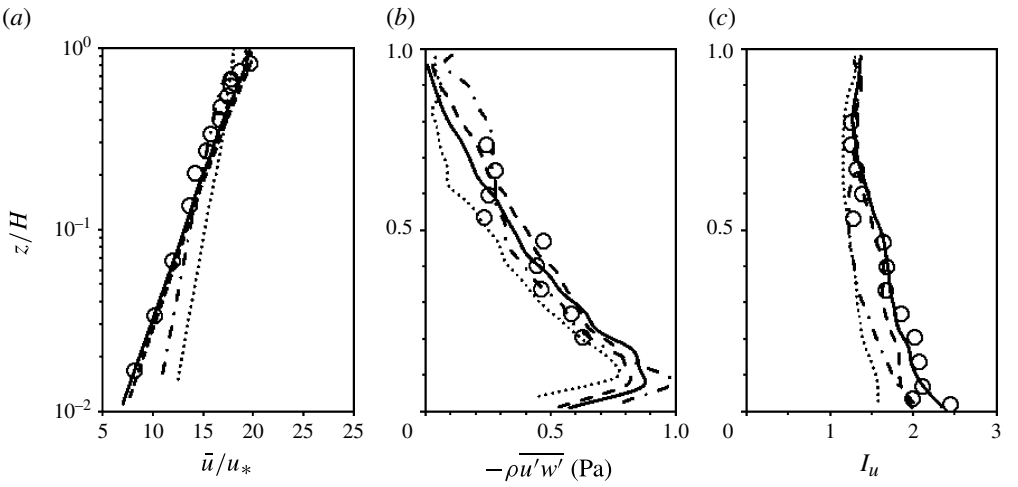

FIGURE 3. Fully developed turbulent flow in the rigid-bed open channel of Venditti & Church (2005) at $Re = 75\,936$ corresponding to the flow prior to the start of the bed deformation. Profiles of (*a*) mean streamwise velocity (non-dimensionalized by the shear velocity u_*), (*b*) Reynolds shear stress $\boldsymbol{\tau}_{uw}$ (Pa) and (*c*) streamwise turbulence intensity I_u at the channel centre. The experimental data of Venditti & Church (2005) (open circles) are compared with LES on grids A (dotted line), B (dot-dashed line), C (dashed line) and D (solid line).

(Venditti & Church 2005). The growth stage is mostly associated with a transition from 2D spanwise features to less regular and larger size 3D bedforms, as discussed by Venditti & Church (2005) and Venditti *et al.* (2006). Once the sand waves reach their 3D stage, they mainly migrate with the main flow, only slightly increasing in size. At their 3D stage, however, the bedforms are sufficiently large to interact with the flow field and substantially modify the dynamics of the turbulent flow field that triggered their onset. In this section we report the results of the coupled hydro-morphodynamic simulations, and the various stages of sand wave evolution are presented, discussed and compared with the experimentally observed results.

5.2.1. *Initiation of sand wave development*

Starting from the flat bed condition and during the first 160 s of the experimental run, Venditti & Church (2005) (see also Venditti *et al.* 2006) reported the emergence of various, progressively larger and more complex features on the bed. In the sequence they appeared in the experiment, these include: (i) spontaneously occurring cross-hatch patterns over the entire bed surface; (ii) chevron-shaped features at the nodes of the cross-hatch; (iii) incipient sand wave crestlines arising as the result of chevron migration; (iv) quasi-2D sand waves forming as crestlines become more organized in the spanwise direction; (v) growth of sand waves in length and amplitude; and (vi) transition to fully grown 2D bed features. As we will show in this section, most of these features were also captured by our simulations.

As reported by Venditti & Church (2005), the cross-hatch pattern appeared spontaneously covering the entire bed surface and consisted of oblique linear striations with an amplitude of $\sim 2d_{50}$ and wavelength of ~4–7 cm. They also reported that the angles observed between the oblique striations and the centreline of the flume varies between 10° and 70°, with an average value of 35°–45°. The emergence of cross-hatch

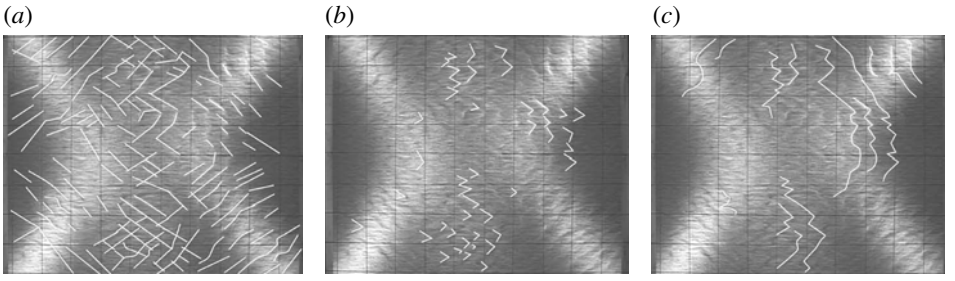

FIGURE 4. Experimental observations of (*a*) cross-hatch patterns, (*b*) chevron-shaped features and (*c*) incipient crestlines in the centre of the channel. The distance between the grid lines in these figures is 0.115 m along both directions, and the flow is from left to right. The clarity of the observed patterns has been enhanced by white lines. (Courtesy of Venditti & Church (2005).)

patterns in the experiment (see figure 4*a*) was followed by downstream migration and subsequent formation of chevron-shaped defects at the nodes of the cross-hatch features (see figure 4*b*). Early bed features very similar to those reported by Venditti & Church (2005) have also been observed by Gyr & Schmid (1989). Describing their observations of bedform initiation, Venditti & Church (2005) mention that, soon after the chevron-shaped features form, they start to migrate and grow rapidly in the spanwise direction to form incipient crestlines, which are span-long bed features roughly perpendicular to the centreline of the flume (see figure 4*c*). The incipient crestlines grow in length and amplitude, ultimately giving rise to well-defined 2D ripples, with quasi-equilibrium wavelength and amplitude of nearly 20 cm and 2 cm, respectively. As reported by Venditti *et al.* (2006), the entire process starting from the flat bed state to the growth of organized 2D bedforms occurs within 160 s (i.e. 100 s after full flow discharge of 0.0759 $m^3\ s^{-1}$ is established), with the initial cross-hatch and chevron features appearing early on during the ramping-up period of flow discharge.

In figure 5 we plot instantaneous snapshots of the simulated initial sand waves in the form of contour plots of the sediment–water interface elevation along the full length of the channel during several instants in time, $t = 5$, 30, 50 and 100 s.

In spite of the previously discussed differences in the initial flow conditions between simulations and experiment – recall that in the latter the flow starts from zero discharge and required ∼60 s to establish the statistically stationary turbulent flow at $Re = 75\,936$ – the simulated bedforms during the initial stages of bed evolution exhibit essentially all the features observed in the experiment. For the first 15 s of the simulation (figure 5*a*), the experimentally observed cross-hatch patterns emerge and cover the entire bed surface. The simulated oblique striations are $\sim 2d_{50}$ high and ∼1–4 cm long, and their angles with the centreline of the channel are in the range of 40°–60°. These values are well within the range of the experimental observations. After approximately 10 s, the cross-hatch patterns have grown in length and amplitude sufficiently to start forming more organized linear striations with small nodes of cross-hatch (figure 5*b*). The nodes grow in size as the striations migrate downstream (figure 5*c*), ultimately forming well-defined chevron-shaped features on the bed. Once the chevrons appear, they grow quickly and form span-long bedforms ∼1.5 cm high and ∼3–10 cm long (figure 5*d*). It is important to note that the growth rate of these initial striations for $t > 10$ s was found to be at least one order

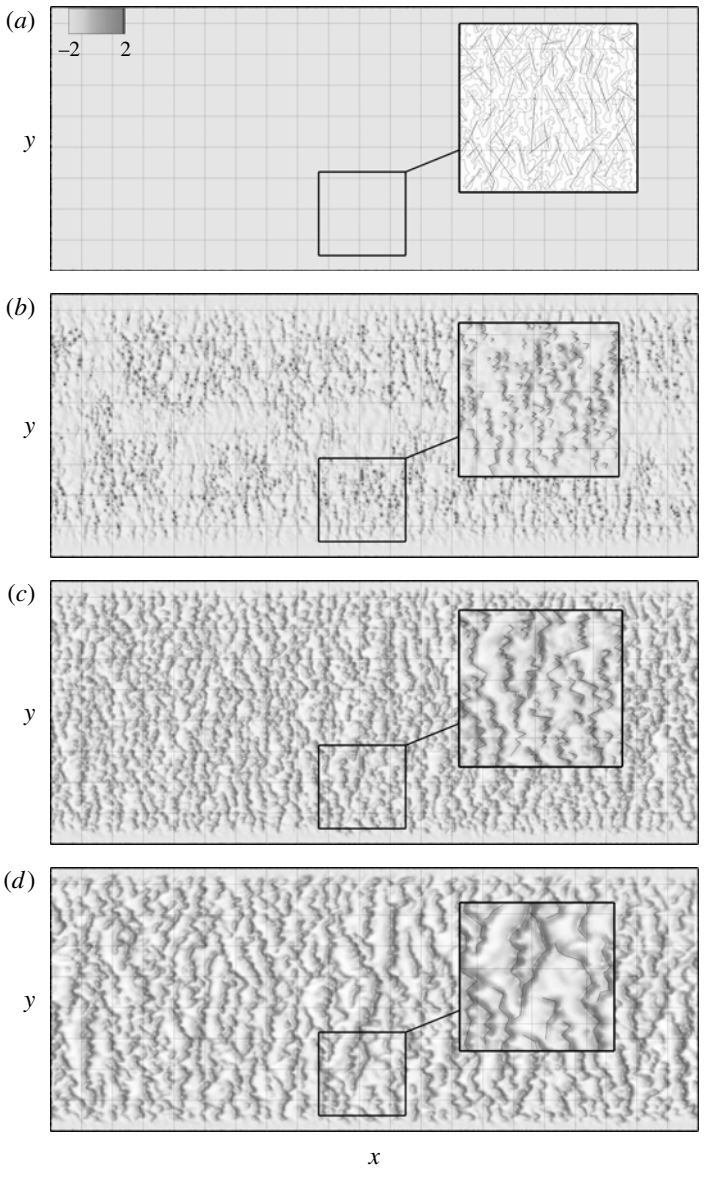

FIGURE 5. Simulated sand wave initiation in 3D contours of bed elevation (cm) corresponding to (*a*) $t = 5$ s, (*b*) 30 s, (*c*) 50 s and (*d*) 100 s, and on grid C. The distance between the grid lines in these figures is 0.115 m along both directions, and the flow is from left to right. The window covers the entire width of the channel (1.0 m in spanwise direction) for the last 2.415 m of the channel. Blown up regions of the bed are inset in each panel to better clarify sand wave patterns.

of magnitude faster than the growth rate observed within $t < 10$ s. We will return to the temporal variation of sand wave growth rate in the next section, where we discuss in more detail the dynamics of the simulated sand waves.

The evolution of the bed elevation during the initiation of bedforms over the entire bed surface shown in figure 5 illustrates that the calculated bed evolution is

quite similar to that described by Venditti & Church (2005) regarding both the time sequence in which various bed features appear and their sizes. A discrepancy between experiments and simulations, however, is observed in the calculated time scale of the initial stage of bed evolution, which appears to be somewhat faster than in the experiment. More specifically, in the simulations the initial stage of bed evolution is completed within 120 s while the same stage requires nearly 160 s in the experiment. Recall, however, that in our simulation the initial flow condition was prescribed as the statistically stationary turbulent flow corresponding to the final discharge of 0.0759 m^3 s^{-1}. In the experiment, on the other hand, the discharge was gradually increased from zero to the full discharge of 0.0759 m^3 s^{-1} within the first 60 s of the experimental run (Venditti *et al.* 2006). Therefore, the statistical state of the turbulent flow above the bed is quite different between the experiments and the simulations during their initial phases, which could account for the observed discrepancy in the time scale of the initial stage of bed evolution. Another possible explanation for this discrepancy between experiments and simulations could be the empirical formula used to calculate the bed concentration ψ_b, which has been derived and calibrated with mean flow quantities. These quantitative discrepancies notwithstanding, however, our simulations capture the process of bedform initiation throughout the bed surface in good overall agreement with Venditti & Church (2005).

To assess the effect of grid refinement on the simulated bed evolution, in figure 6 we compare instantaneous bed geometry computed on the four grids at three instants in time. While the broad trends of the bed evolution are similar on all four grids, it is evident that the coarsest grid (grid A) is not able to capture the fine-scale bed features, and especially the early cross-hatch patterns, and the rate at which the sand waves grow in size with the clarity and accuracy of the two finer mesh simulations. It is evident from figure 6, for instance, that, while on grids B, C and D well-developed chevron-shaped patterns and incipient crestlines are already established by $t = 50$ s, such features become visible on grid A in figure 6 only for $t > 100$ s. It should be noted that the bed in the grid A simulation has already been destabilized by $t = 50$ s via a similar sequence of events as on the two finer meshes, but the amplitude of cross-hatch and chevron patterns simulated on grid A is too small to be visible in the bed elevation contour scale we use in figure 6. In general, comparing the simulated results for the bed morphology on grid D with those on grid A during the initial stages of the simulation, the growth rate of bed features on grid A exhibited a consistent time lag of approximately 100 s. On the other hand, the simulations on grid B yielded a sand wave growth rate more similar to those obtained on grid D. Eventually, the simulation results on grid C are quite similar to those on grid D in terms of both sand wave characteristics and overall sand wave shape. In summary, the comparisons between the four grids we have employed herein show that grid A cannot resolve the early stages of bed evolution with regard both to the time scales and to the sharpness and clarity of bed features observed in the experiments. Grid B is also not fine enough to capture the details of the sand wave initiation. However, simulations on grids C and D yielded quite similar results for the initial stage of sand wave development. The sensitivity of the computed bed patterns to grid refinement will be further examined in a quantitative manner in subsequent sections. Unless otherwise indicated, the results we present in the remainder of this paper have been obtained on grid C, since, and as already discussed above, the simulations on the finest grid D were continued only for the first 200 s of bed evolution.

An important question that continues to be a subject of debate in the literature is with regard to the mechanism that triggers the initial bed instability and

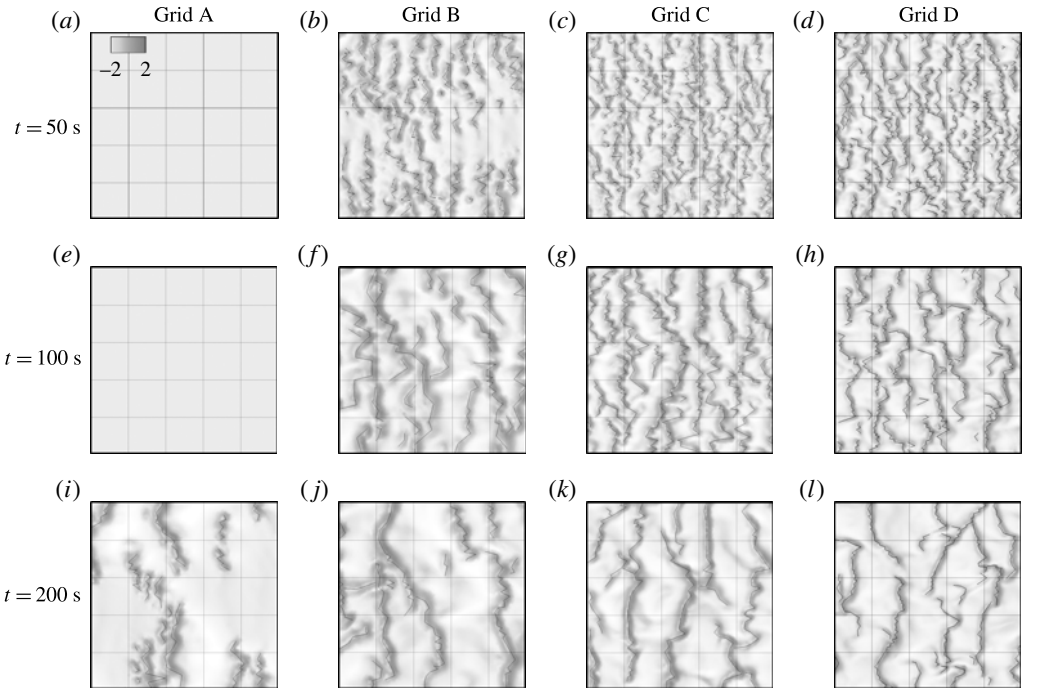

FIGURE 6. Computed bed morphology at various instants in time on grids A, B, C and D. Three-dimensional contours of bed elevation are in centimetres. The selected windows are located at the centre of the channel. The distance between the grid lines in these figures is 0.115 m along both directions, and the flow is from left to right.

gives rise to the early cross-hatch and chevron-shaped sand waves. Early theories (Bucher 1919; von Kármán 1947; Liu 1957) attributed the onset of the initial bed instability to interfacial Kelvin–Helmholtz (KH) type waves in the stratified near-bed sediment–water layer induced by sediment suspended in the flow (Liu 1957; de Jong 1989). Another point of view is that the bed destabilization mechanism is linked to near-bed coherent structures over the initially flat bed, which gives rise to variations in velocity and shear stress. Venditti & Church (2005) provided evidence in support of this idea by using velocity time-series measurements to estimate the average or dominant size of the eddies near the bed before the bed was destabilized, and showing that it is approximately equal to 7 cm, which is similar to the length scale of the linear cross-hatch bed patterns (see figure 5*a*). Numerical simulations have also yielded conflicting results regarding this issue. As we already discussed previously, Chou & Fringer (2010), who simulated oscillatory flow over a mobile sand bed, presented evidence pointing to the conclusion that density stratification effects near the bed play a key role in triggering the initiation of bedforms. More specifically, they carried out simulations on an identical grid using different models for the bed elevation equation and the flow–sediment mixture and showed that, when density stratification effects are neglected in the momentum equation, no ripples arise in the numerical simulation. These results, therefore, provided support to theories linking the initial destabilization of the bed to the instability of the near-bed stratified layer. Escauriaza & Sotiropoulos (2011*a*), on the other hand, who considered the initial stages of bed evolution inside the scour hole around a cylindrical pier, were able to

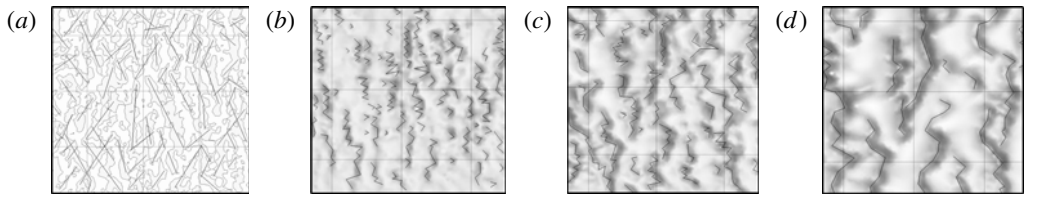

FIGURE 7. Simulated sand wave evolution in 3D contours of bed elevation (cm) corresponding to (*a*) $t = 5$ s, (*b*) 30 s, (*c*) 50 s and (*d*) 100 s, on grid C and with Boussinesq term in (2.2) set to zero. Flow is from left to right. The grid lines are 0.115 m apart along both directions. The window size, location and bed elevation scale are similar to the selected window in figure 5.

simulate ripple formation starting from an initially flat bed, considering only bedload transport and without incorporating stratification effects in their model. These results, therefore, appear to support the findings of Venditti & Church (2005) regarding the role of near-bed flow patterns over an initially flat bed.

All simulations we have reported thus far in this paper have been carried out using the stratified flow model described in § 2 and thus stratified flow effects have been taken into account. To elucidate whether stratification effects play a role in destabilizing the bed for the case we consider herein, we also carried out simulations on all four grids for the initial stage of the process by neglecting the Boussinesq term on the right-hand side of (2.2) but retaining all other aspects of the coupled hydro-morphodynamic model described in § 2. On the coarsest grid, grid A, and to some extent on grid B, this numerical experiment failed to destabilize the bed, which remained stable and flat throughout the simulation interval. On the two fine grids (C and D), however, the bed was destabilized in a manner similar to that we obtained using the full stratified flow model. In order to compare the simulated sand waves with and without the stratification term, we plot in figure 7 the same snapshots of the sand wave geometry for the simulation with no stratification on grid C as those reported in figure 5. As seen in figures 5 and 7, the overall patterns of the bedforms are similar for the two cases. However, the amplitudes of the simulated sand waves start to diverge slightly apart between the stratified and unstratified models as time increases. Even though not shown here, similar trends are also observed on grid D.

To quantify the effects of stratified flow on the destabilization of the bed at various stages of the process, we plot in figure 8 contours of the difference between the bed elevation simulated with the full stratified model (z_{str}) and that simulated with the Boussinesq terms in (2.2) set equal to zero (z_{nstr}) at various instants in time (n). Both stratified and unstratified model results shown in this figure were obtained on grid C, and the differential bed elevation (Δz_{rms}) at each instant in time has been scaled with the maximum amplitude of sand waves ($|\Delta|$) that is calculated by the stratified flow model at that instant in time:

$$\Delta z^n_{rms} = \frac{z^n_{str} - z^n_{nstr}}{|\Delta^n|} \times 100. \tag{5.1}$$

It is seen from figure 8(*a*) that the computed results from the two simulations are identical at $t = 5$ s when the calculated bed elevation difference is actually equal to machine zero (see figures 5*a* and 7*a*). The bed elevation difference begins to grow monotonically with time as the amplitude of the sand waves increases, but it is evident

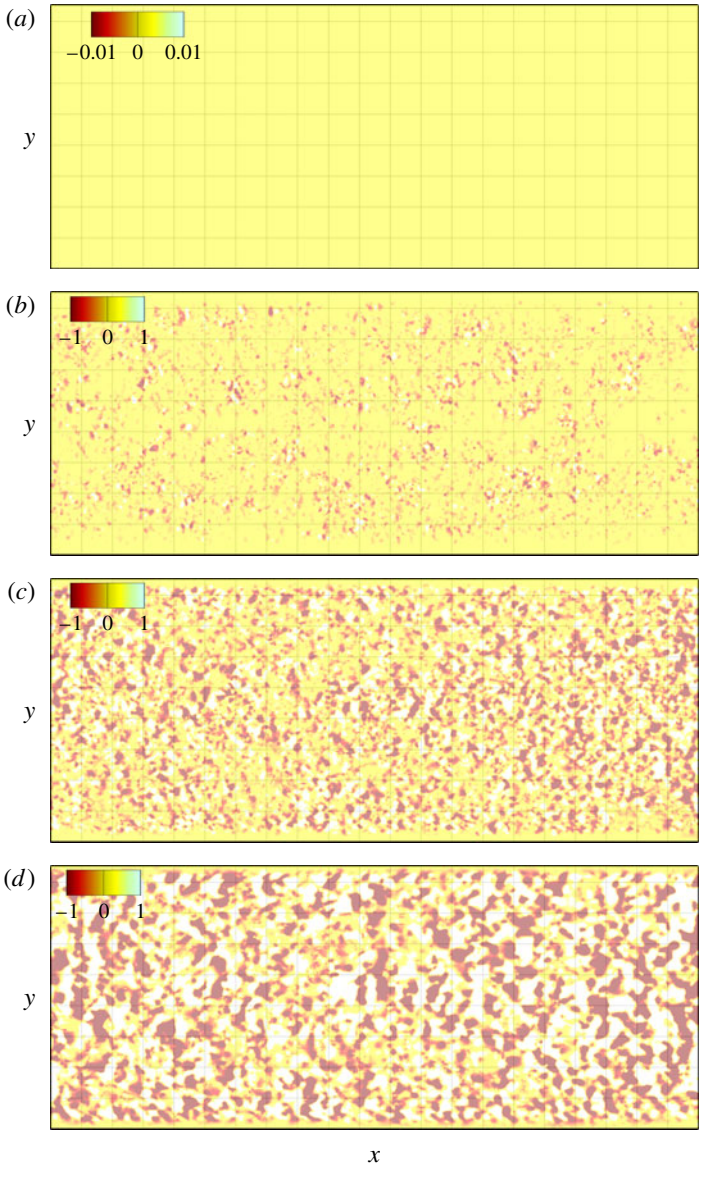

FIGURE 8. (Colour online) Contours of calculated (grid C) bed elevation difference between the bed morphology obtained with stratified and unstratified flow simulations, Δz_{rms} (see (5.1)), at (*a*) $t = 5$ s ($|\Delta z_{rms}|_{max} \sim 10^{-6}$), (*b*) 30 s ($|\Delta z_{rms}|_{max} = 1.8$), (*c*) 50 s ($|\Delta z_{rms}|_{max} = 6.2$) and (*d*) 100 s ($|\Delta z_{rms}|_{max} = 9.8$). Flow is from left to right and the grid lines are 0.115 m apart along both directions.

from the results of figure 8 that at least up until $t = 30$ s the effect of stratification on the evolution of the bed is minimal (see also figures 5*b* and 7*b*). At later times, however, the results from the two simulations start growing apart, with maximum errors ($|\Delta z_{rms}|_{max}$) approaching 10 at $t = 100$ s (see also figures 5*d* and 7*d*). These results support the findings of Venditti & Church (2005) and suggest that near-wall flow structures over the initially flat bed play a key role in destabilizing the bed.

Presumably grid A is not sufficiently fine near the bed to adequately resolve the flow at the scale of eddies that give rise to the linear cross-hatch patterns and for that neglecting stratification effects for this case fails to destabilize the bed. It is interesting to note, however, that for this case (grid A), even though the details of the flow and early cross-hatch bed patterns cannot be resolved, stratification effects act to ultimately trigger the bed instability, suggesting that instabilities in the near-bed stratified layer also play a role in destabilizing the bed. Recall, however, that as we have already discussed above the bed instability simulated on grid A exhibits a consistent time lag of approximately 100 s compared to the grid D, C and B simulations. As shown in figure 8, this is exactly the time when the stratified and unstratified simulations on grid C begin to exhibit major differences, which further suggests that stratification effects do become important but at later times after the bed has been destabilized and a stratified layer has formed above the bed. This is also consistent with our finding regarding the ratio of suspended load to bedload during the early and late stages of sand wave evolution (see § 5.2.4).

Venditti & Church (2005) alluded to the possibility of different mechanisms becoming important at different stages of the process by commenting that 'there is no reason that an instability that gives rise to well-organized variations in sediment transport must continue to dominate the flow once a bed wave is established'. Our results support this assertion and for that reason all subsequently presented results have been obtained using the stratified formulation. The specific linkage between near-bed flow structures over the initially flat bed and the early cross-hatch-shaped sand waves will be further examined in § 5.3 below.

5.2.2. *Transition from chevrons to two-dimensional bedforms*

Two-dimensional sand waves are defined to have roughly uniform spacing, height and length, while their crestlines tend to be straight or slightly sinuous and are oriented perpendicular to the direction of the mean flow (see Ashley 1990; Venditti *et al.* 2005*b*). Venditti & Church (2005) reported that, at the end of the sand wave initiation process in their experiment, the chevrons migrate and begin to organize transversely, forming ridges perpendicular to the flow with a preferred streamwise spacing. This process eventually leads to the emergence in the experiment of the first set of 2D bedforms at approximately $t \sim 160$ s. These sand waves are regularly spaced with experimentally observed wavelength and amplitude in the range of approximately 4 to 14 cm and 2 cm, respectively (see figure 9). In the experiment of Venditti & Church (2005) this 2D state lasted for nearly 500 s, until $t \sim 600$ s, when the sand waves started undergoing a distinct transition to their 3D state. It is important to note, though, that, in spite of using the term 'two-dimensional sand waves', it is evident from a visual inspection of figure 9 that the experimentally observed sand waves are never perfectly 2D (i.e. straight, parallel crestlines perpendicular to the flow direction). A number of complex topological connections among neighbouring bedforms as well as distorted crestlines are evident in figure 9, which suggest that a perfectly 2D state was not realized in the experiment. Venditti & Church (2005) have proposed a more quantitative approach to delineate the 2D state of bed evolution and identify the instant when three-dimensionality emerges, which we will discuss in detail in a subsequent section.

In figure 10 we show snapshots of calculated bed elevation contours at two instants in time, $t = 150$ and 300 s, which are within the interval when Venditti & Church (2005) reported the onset of the 2D state in their experiment. In our simulations, this state, which starts at $t \sim 120$ s, can be at best characterized as quasi-2D, since, as

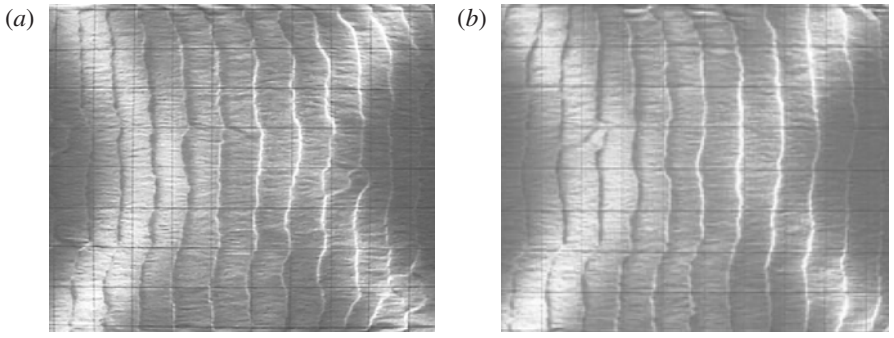

FIGURE 9. Experimental observations of sand waves during their 2D state at (*a*) $t = 240$ s and (*b*) $t = 300$ s in the centre of the channel. Flow is from left to right and the grid lines are 0.115 m apart along both directions. (Courtesy of Venditti & Church (2005).)

evidenced by the results shown in figure 10, the simulated bedforms do not appear as 2D in their spanwise structure as in the experiment (compare figures 9 and 10).

We argue that the inability of the simulations to reproduce crestlines closer to a 2D state as seen in the experiment should be attributed to the length of the computational domain and the approach we employ to specify inlet conditions for the flow and sediment concentration in the simulation. Recall that the flume of Venditti & Church (2005) is 10.5 m long and the observation window within which the evolution of sand waves was monitored starts at approximately 7.5 m from the inlet. Owing to the significant computational cost of a coupled LES, the computational domain is only 3.5 m long. As we discussed above, at the inlet of this domain we continuously feed instantaneous velocity fields from a pre-computed LES of fully developed open channel flow over a rigid bed and recirculate numerically the suspended sediment exiting the domain by setting the sediment flux at the inlet equal to the outlet flux at every instant in time. The latter boundary condition, however, which is intended to emulate the sediment recirculation in the experiment of Venditti & Church (2005), introduces disturbances to the near-bed flow near the inlet. Such disturbances are also introduced in the experiment at the inlet, but the 7.5 m of flume upstream of the observation window provides an opportunity for the bed to develop and the effects of the disturbances to be reduced by the time the flow reaches the observation window. In the simulations, however, the distance from the inlet to the observation window is only 1 m. We thus argue that disturbances induced by the numerical recirculation of sediment could be impacting the bed within the observation window, preventing a more 2D state from emerging and triggering sooner the onset of the 3D state. A quantitative assessment of the degree of two-dimensionality of the simulated bedforms during this stage will be discussed in the next section using the metric proposed by Venditti & Church (2005).

5.2.3. *Transition to three-dimensional bedforms*

Venditti *et al.* (2005*b*) reported that in their experiment the 2D phase of bed evolution ends at approximately $t = 600$ s. The onset of the 3D state in the experiment was characterized via sporadic mass transport events during which small masses of sand material detach from sand waves to form idle crest defects, which are transported and merge with neighbouring sand waves. As a result of such processes, the patterns

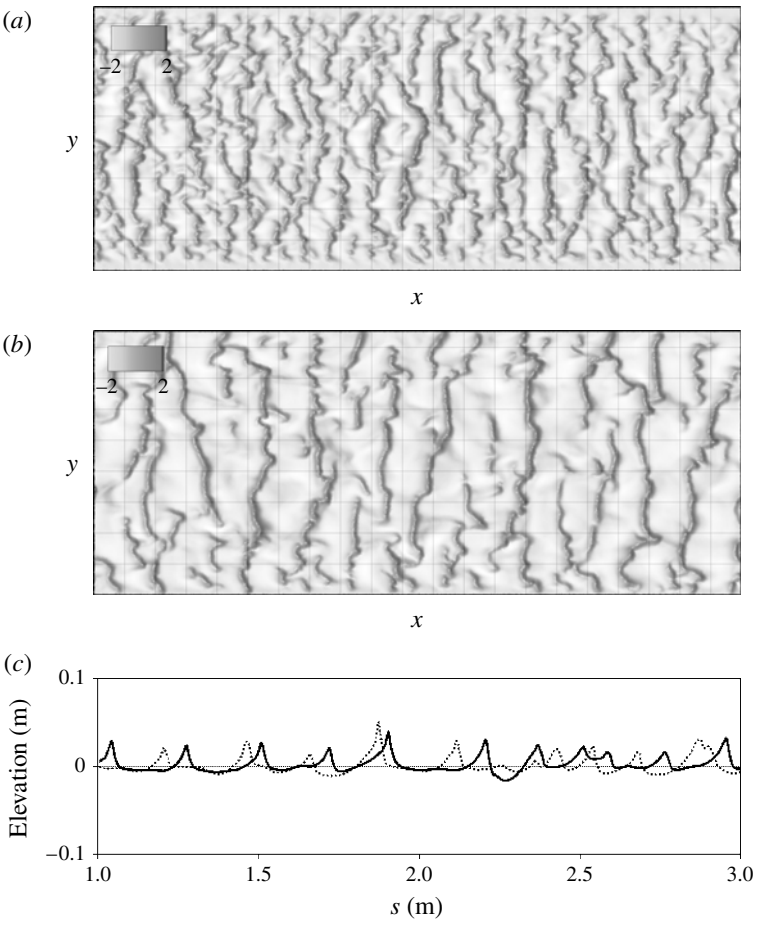

FIGURE 10. Instantaneous images of the bed morphology (3D contours of bed elevation are in centimetres) showing the sand waves at transition from chevron shape to 2D states corresponding to (*a*) $t = 150$ s and (*b*) 300 s. Flow is from left to right and the grid lines are 0.115 m apart along both directions. The windows in cover the entire width (1.0 m in spanwise direction) for the last 2.415 m of the channel. (*c*) The bed elevation profiles along 2 m of the channel centreline in the centre of window (*a*) with dotted line and (*b*) with solid line.

of the bedforms become irregular and more sinuous in the spanwise direction and develop complex multi-connected topologies as shown in figure 11, which depicts two snapshots of the 3D state. The bedforms at this stage grow larger than in the 2D stage, with wavelengths and amplitudes in the range of ∼10–50 cm and ∼4–6 cm, respectively (Venditti *et al.* 2005*b*).

Figure 12 shows two representative snapshots of the calculated bed morphology at two instants in time within the 3D state of bedforms. Comparing this figure with the experimental images shown in figure 11, it is readily apparent that the simulations capture a number of the complex topologies observed in the laboratory flume. Among other things, we observe: many of the computed sand waves to be highly distorted and sinuous in the spanwise direction; complex bifurcations of crestlines; and the formation of distinct distorted O-shaped features connecting adjacent crestlines. The

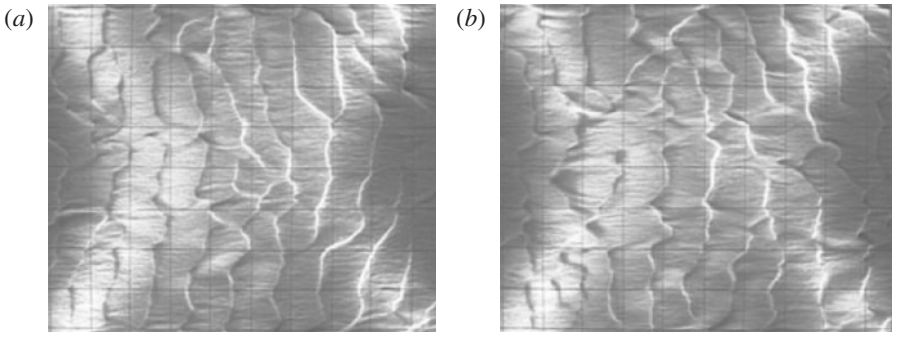

FIGURE 11. Experimental observations of sand waves during their 3D state at (*a*) $t =$ 900 s and (*b*) $t = 1020$ s. Flow is from left to right and the grid lines are 0.115 m apart along both directions. (Courtesy of Venditti & Church (2005).)

latter feature is further highlighted in figure 13, which shows instants in time when such complex patterns are realized in the simulation and the experiment. The similarity between the two patterns is striking, which further underscores the ability of our simulations to capture sand wave topologies realized experimentally. It should be noted that, even though such patterns appear even during the 2D state (see figures 9 and 10), they become very pronounced and prevalent when the 3D state emerges.

The previously discussed fundamental mass-transport mechanism among sand waves that causes topologically complex crestlines to emerge is clearly illustrated in figure 14, which shows three snapshots from the simulations highlighting the overall process. A small crest defect that forms at $t = 700$ s is seen in figure 14 to migrate and ultimately merge at $t = 900$ s with a downstream sand wave causing a bifurcating crestline to form. Our simulations support the experimental findings of Venditti *et al.* (2005*b*) that such mass transport events play a key role in maintaining the 3D patterns of the bedforms, by providing the key mechanism for crestline bifurcation and formation of complex topologies (see figure 14).

de Moraes Franklin (2013) employed a line recirculation vortex model with an external flow and stability analysis to find a relationship to predict the longitudinal and transverse wavelength of 3D ripples. Using their model, de Moraes Franklin (2013) predict that the maximum wavelength of 3D ripples is $\lambda_{max} = 281 d_{50}$. Employing Franklin's relation, this scale for our specific case with a d_{50} of 0.5 mm would be $\lambda_{max} = 14$ cm. The measured wavelength for 2D and early 3D stages by Venditti & Church (2005) are 15 cm and 65 cm, respectively. The computed maximum wavelength for 2D and 3D stages are 17 cm and 68 cm, respectively. Hence, it seems that Franklin's relation is more valid for the initial stages of bedform evolution and during the early 2D stage of sand wave development for the test case simulated and measured in this work. Andreotti, Claudin & Douady (2002) also proposed a model for the transverse wavelength of 3D ripples. Using experimental and field data, Andreotti *et al.* (2002) showed that the transverse wavelength λ_{trans} and longitudinal wavelength λ_{long} of bedforms are related as $\lambda_{trans} \approx 1.3\lambda_{long}$. Based on Franklin's model, on the other hand, the transverse wavelength of sand waves at their 3D stage is $\lambda_{trans} \approx 0.8\lambda_{long}$. The $\lambda_{trans}/\lambda_{long}$ ratio for the simulated sand waves during the 3D stage in our work, however, varies between 0.85 and 1.25. This ratio for the sand waves measured by Venditti & Church (2005) is also approximately within the same range (0.8–1.3). This means that, for both the measured and simulated sand waves

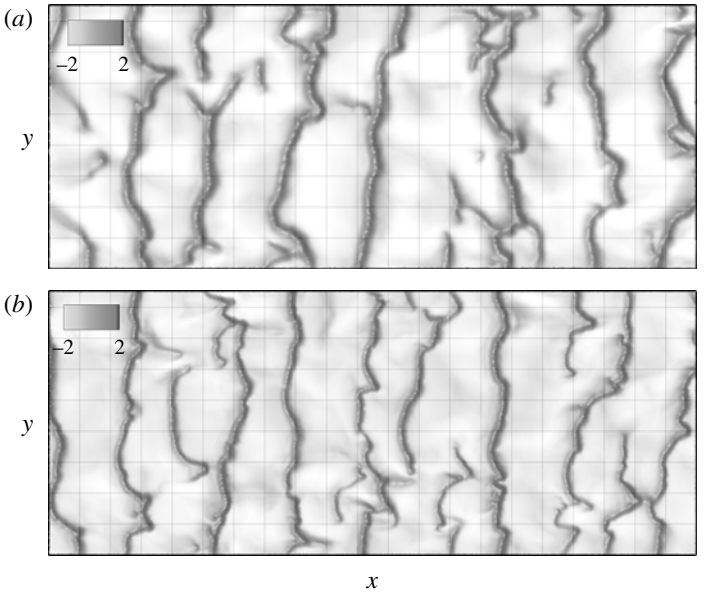

FIGURE 12. Computed instantaneous images of the bed elevation contours (cm) showing the sand waves at 3D state corresponding to (*a*) $t = 700$ s and (*b*) 1200 s on grid C. Flow is from left to right and the grid lines are 0.115 m apart along both directions. The windows cover the entire width of the channel (1.0 m in spanwise direction) for the last 2.415 m of the channel.

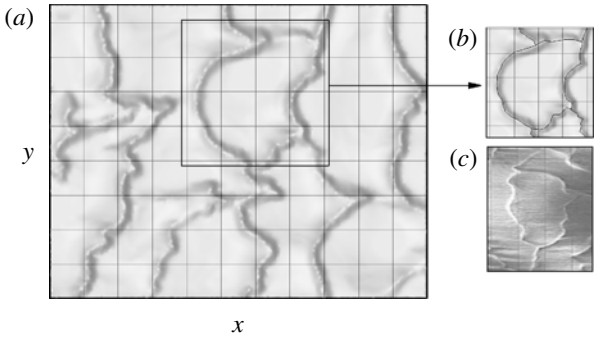

FIGURE 13. (*a*,*b*) Computed and (*c*) experimentally observed 3D bed features at the 3D stage of sand wave evolution. Images are shown for $t = 660$ s and 890 s for computed and measured, respectively. The window in (*a*) covers the entire width of the channel and for approximately 1.2 m of the central part of the channel. Flow is from left to right and the grid lines are 0.115 m apart along both directions.

that we consider herein, during the early 3D stages of the process λ_{long} is shorter than λ_{trans} and the ratio is more than unity. At later stages, the longitudinal wavelength increases above λ_{trans} and so the ratio is reduced to approximately 0.85. Thus, the range of $\lambda_{trans}/\lambda_{long}$ ratio for the simulated sand waves in this work is reasonably consistent with the model presented by Andreotti *et al.* (2002).

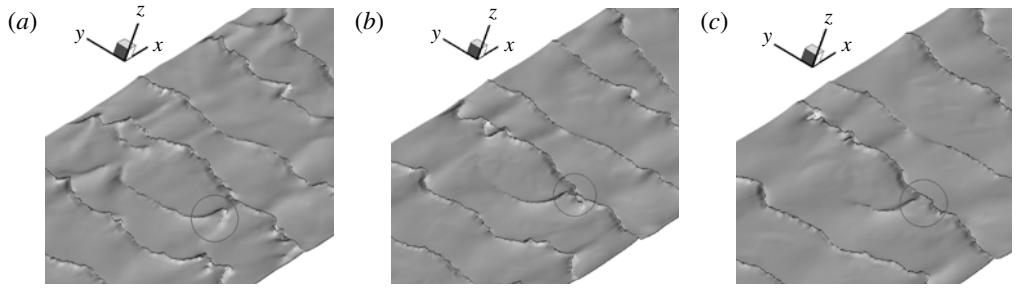

FIGURE 14. Computed instantaneous images of the bed morphology showing a crest defect (circled) catching up with and merging into a downstream sand wave. The selected windows are located at the centre of the flume. The idle crest defect was earlier cleaved from an upstream sand wave. Images correspond to time instants of (*a*) $t = 700$ s, (*b*) 800 s and (*c*) 900 s. The windows cover the entire width of the channel and for approximately 1.0 m of the central part of the channel. Flow is from bottom left to top right.

5.2.4. *Quantitative characteristics of sand waves*

Venditti *et al.* (2005*b*) systematically analysed the characteristics of the sand waves in their experiment and reported quantitative information about the temporal variation of sand wavelength, amplitude and celerity. The characteristics of the sand waves were measured using two in-line acoustic sensors, which are 13.3 cm and 0.45 m apart in the streamwise and spanwise directions, respectively, focusing on the observation window of the flume (see § 3). We post-process our simulated sand waves by manually identifying the number of sand waves present in the observation window at a given instant in time, measuring their amplitude and wavelength, and tracking them to calculate their celerity. Since during most instants in time sand waves are quite distorted, for each sand wave we average the various properties along the spanwise direction.

In figure 15 we plot the simulated temporal variation of sand wave characteristics (amplitude, length and celerity) on grid C along with the measurements of Venditti *et al.* (2005*b*) over a time interval long enough to include all previously discussed stages of bed evolution (spanning approximately 4.2 h in the simulations and 5.5 h in the experiment). Since Venditti *et al.* (2005*b*) used two echo sounders (at two different locations) to measure the sand wave characteristics (wavelength, amplitude and celerity), the experimental data in figure 15 (open circles) represent the instantaneous values measured with both echo sounders. However, the simulated data in figure 15 (filled circles) are the domain-averaged values throughout the bed surface at every instant in time. Therefore, the variation in simulated results is less than in the measured quantities. It is evident from this figure that the amplitude, length and celerity of the computed sand waves are well within the range of the measured values at most instants in time. The most significant discrepancies are observed during the early stages of the process when the simulated sand waves appear to grow in amplitude somewhat faster than the measurements, reaching the quasi-equilibrium state approximately 30 min sooner than in the measurements. The aforementioned differences between experiments and simulations concerning the gradual ramping up of the flow in the laboratory flume, the length of the laboratory flume and computational domain, and the potential disturbances introduced in the simulation due to the manner in which sediment was recirculated numerically, may account for

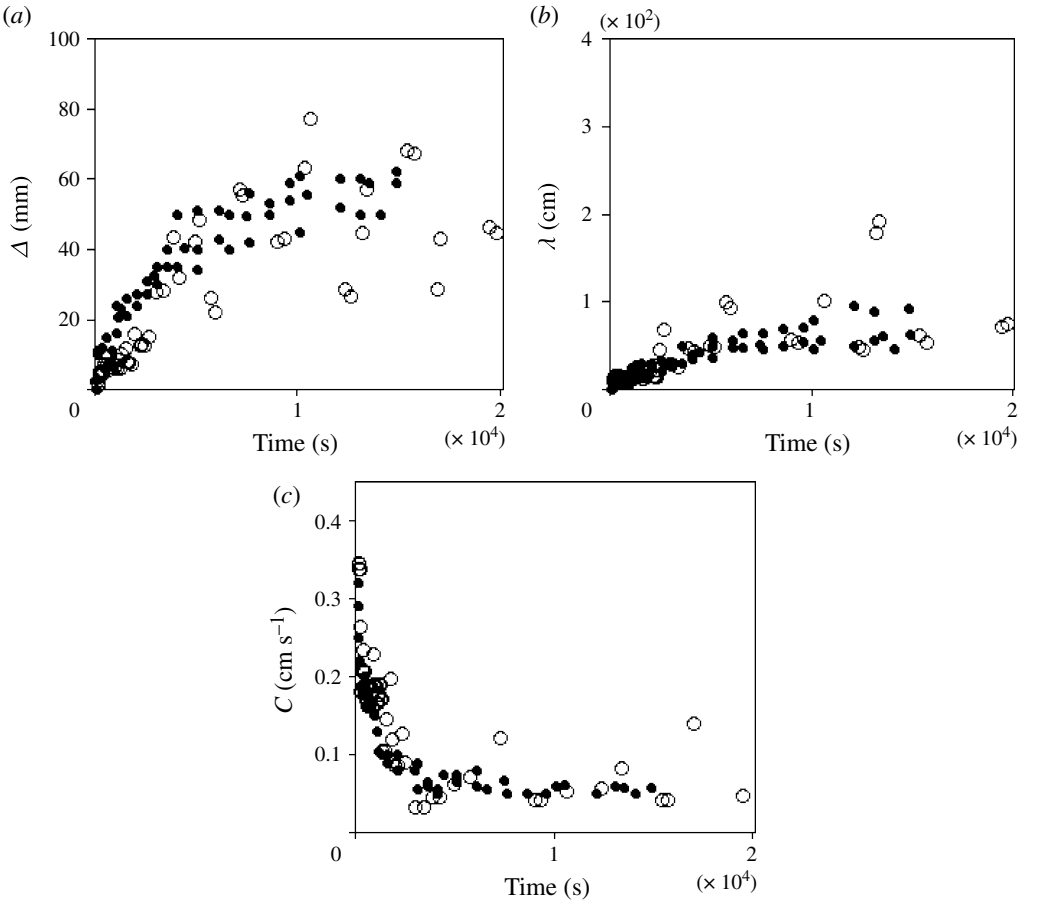

FIGURE 15. Measured (Venditti *et al.* 2005*b*) and computed sand wave (*a*) height, (*b*) length and (*c*) celerity. The experimental data (open circles) represent individual sand waves that are instantaneously measured, while the computed values (filled circles) are averaged on the bed surface at each instant in time.

these discrepancies. These differences notwithstanding, however, and considering the complex and inherently intermittent nature of the underlying processes, figure 15 clearly shows that the simulations capture sand waves whose characteristics are comparable to what was measured in the laboratory.

To quantify the effect of grid resolution in the accuracy of the predicted sand wave characteristics, we plot in figure 16 the temporal variation of domain-averaged values of sand wave amplitude, length and celerity calculated on grids A, B, C and D. With the only exception being the temporal variation of the amplitude, where grid B slightly overshoots the grid C prediction, figure 16 demonstrates the monotonic convergence of sand wave characteristics as the grid is refined, and makes a strong case that, at least as far as the sand wave characteristics are concerned, the grid C simulations can be characterized as grid-insensitive. Note that the simulations on grid D were carried out for only the first 200 s, but during this interval the computed results of grids D and C are very similar (see figure 16). Grids B and C also yield results close to each other for all three quantities, but the sand waves predicted on the coarsest grid, grid A,

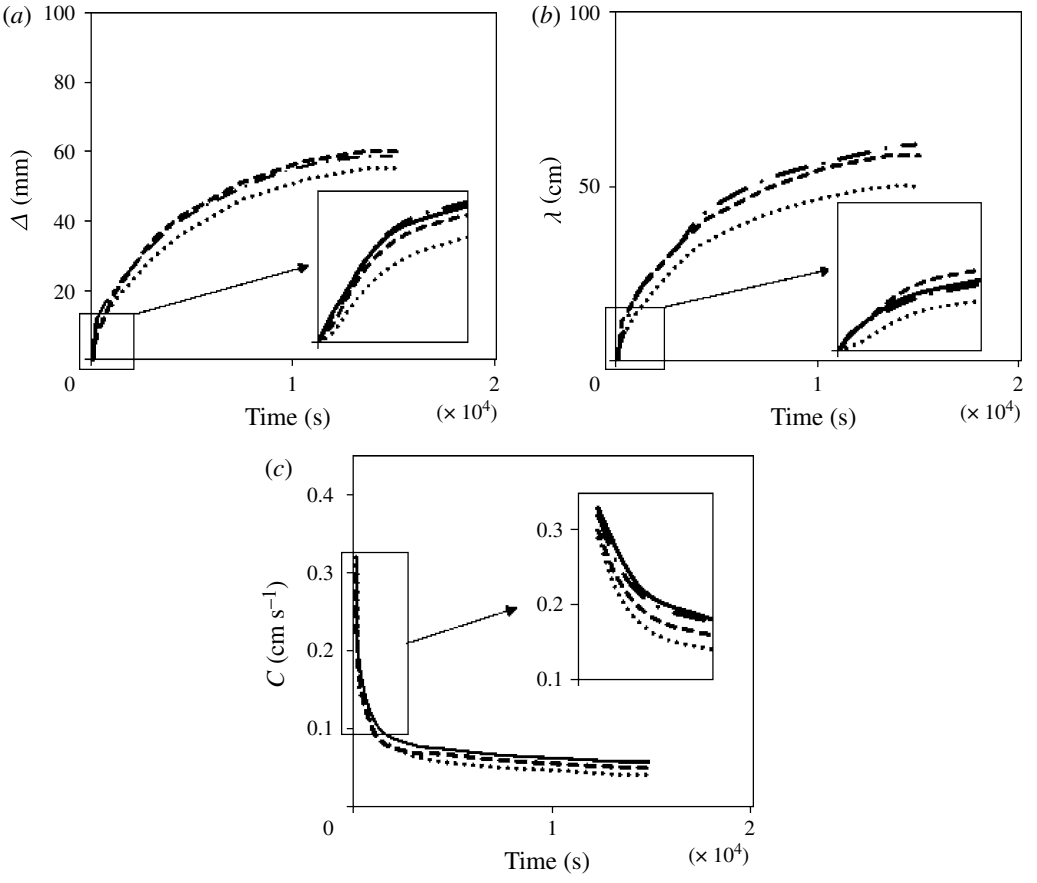

FIGURE 16. Computed sand wave (*a*) height, (*b*) length and (*c*) celerity using grid system A (dotted), B (dashed), C (dotted-dashed) and D (solid). Simulations on grid D are continued for only the first 200 s.

grow significantly slower in amplitude and length, with the discrepancy being more pronounced in the predicted sand wavelength. Most importantly, the quasi-equilibrium sand waves on grid A have smaller amplitude and length and travel at a slightly lower speed than on grids B and C. These results are consistent with the previously discussed quantitative comparisons between the four grids (see figure 16).

To quantify the topological complexity of bedforms and to characterize the 2D and 3D states, Venditti *et al.* (2005*b*) proposed a metric denoted as the non-dimensional span factor (*NDS*) as

$$NDS = \frac{\Lambda_c}{\Lambda_y}, \tag{5.2}$$

where Λ_c is the arclength of the bedform along its crestline and Λ_y is the linear distance between the end points of the crestline at the channel side walls (see figure 17). For sand waves with crestlines that do not extend all the way to the channel side walls, the above definition can also be employed using the two end points of the crestline. Similar to the stream sinuosity factor, the *NDS* is simply a measure of sand wave crest sinuosity. By definition, $NDS = 1$ for a line connecting two

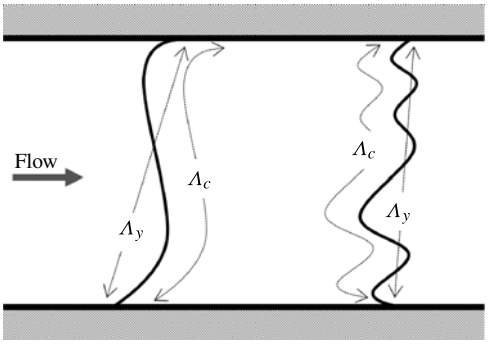

FIGURE 17. Schematic view of sand wave sinuosity parameters.

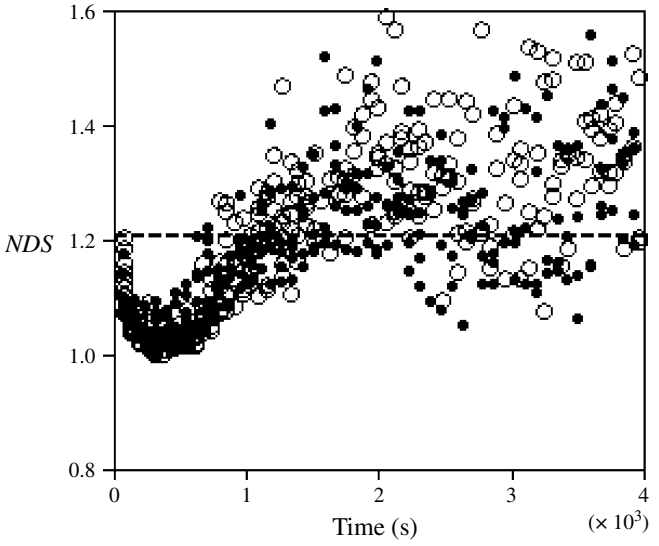

FIGURE 18. Computed (filled circles) and measured (open circles) (Venditti *et al.* 2005*b*) non-dimensional span *NDS* for the whole range of observed crestlines.

points and approaches infinity in the limit of a space-filling curve spanning the same two points. Following Venditti *et al.* (2005*b*), therefore, the value $NDS = 1$ marks a bed composed of perfectly straight-crested 2D dunes, while a value sufficiently greater than one can be used to identify the transition from the 2D to the 3D state. The minimum value found in the experiments of Venditti *et al.* (2005*b*) is $NDS = 1.02$ while the threshold marking the onset of the 3D state was set equal to $NDS = 1.21$ by examining the state of the bed and empirically deciding the *NDS* value for which the bed is composed primarily by a mixture of highly sinuous and linguoid bedforms (Venditti *et al.* 2005*b*).

In figure 18 we plot the measured and computed values of *NDS* as a function of time for the first hour of bed evolution for all bedforms present within the observation window at each instant in time. The first phase of bed evolution is marked in this figure by the line $NDS = 1.21$, which delineates the transition from the 2D to the 3D states. It is evident from this figure that the calculated values of the *NDS* are in reasonable agreement with the measurements of Venditti *et al.* (2005*b*). The

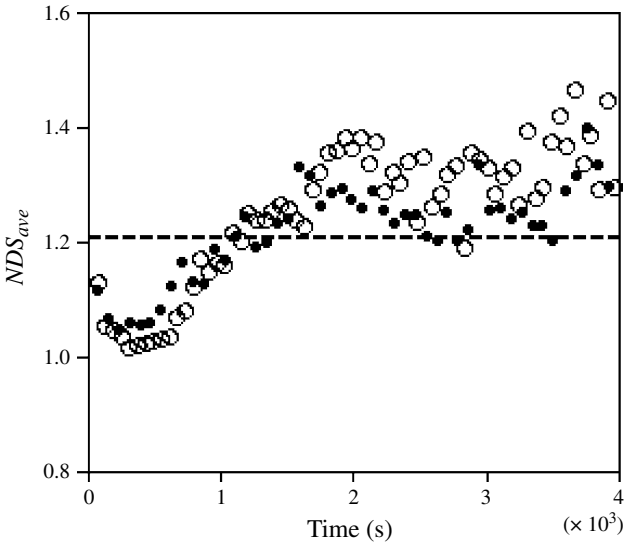

FIGURE 19. Computed (filled circles) and measured (open circles) (Venditti *et al.* 2005*b*) averaged non-dimensional span NDS_{ave}.

calculated values, however, do not get as close to unity as do the measurements and are overall somewhat higher than the measurements throughout the first phase of bed evolution. Moreover, the simulated bed crosses the $NDS = 1.21$ threshold at ∼700 s, which is sooner than in the experiment. Overall, these trends are consistent with the previously discussed finding that the simulations do not produce a state of the bed evolution as 2D as observed in the experiment. As the *NDS* threshold for the onset of three-dimensionality is crossed, both simulated and measured *NDS* values begin to exhibit significant scatter and a great deal of intermittency, with values fluctuating wildly between clearly 3D and 2D bed states. As discussed by Venditti *et al.* (2005*b*), this trend is attributed to the complex and highly fragmented crestline topologies that emerge during the 3D state during the crestline reorientation process. Such crestlines are not persistent in time and give rise to the large scatter observed in figure 18. The numerical simulations reproduce this important feature of the 3D state of the bed with reasonable accuracy.

To further quantify the level of agreement between the measured and computed temporal variation of the *NDS*, we plot in figure 19 the temporal variation of NDS_{ave}, which is obtained by averaging at each instant in time the values of *NDS* for crestlines with $\Lambda_y \geqslant 0.8$ m. This figure clarifies the trends we discussed in the previous figure and further allows us to gauge the level of agreement between the experiments and simulations during the 3D state when the *NDS* values exhibit large scatter. It is evident, for instance, that once the $NDS = 1.21$ threshold is crossed, both the measured and simulated NDS_{ave} values fluctuate around an equilibrium value, which is equal to approximately 1.3 in the experiments and 1.25 in the simulations.

Numerous field and experimental studies have been devoted to investigate the ratio of bedload to suspended load in waterways under various flow field condition (see e.g. Fredsoe 1974; van Rijn 1993; Best 2005; Andreotti *et al.* 2011; Charru *et al.* 2013). For a fixed flow condition, however, the variation of this ratio at different stages of sand wave evolution has not been investigated. Using the simulation results in this

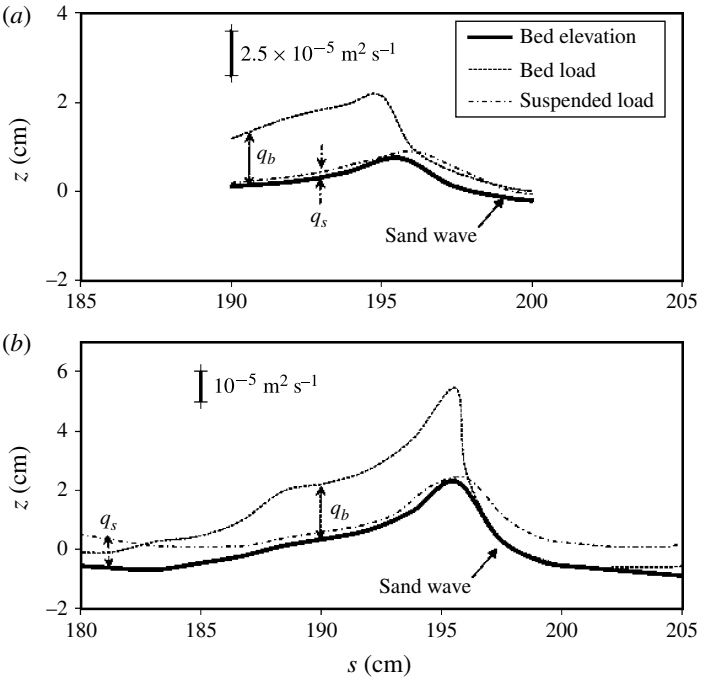

FIGURE 20. Calculated instantaneous profiles of bedload (q_b) and suspended load (q_s) distribution over a sand wave along the streamwise direction ($\boldsymbol{s}$ vector) during (*a*) the 2D stage and (*b*) the 3D stage of sand wave development. The 2D and 3D stages correspond to $t = 200$ s and 400 s, respectively. Flow is from right to left and the vertical axis is elevation above bed.

work, we attempted to identify the relationship between bedload and suspended load during the 2D and 3D stages of sand wave development. In figure 20, we plot the variation of suspended load and bedload along the streamwise direction over a single sand wave in the middle of the channel and at two different instants in time: one during the 2D stage; and one during the 3D stage of sand wave development. The suspended load is calculated as the depth integral of the product of the streamwise velocity component with the suspended sediment concentration above the bedload layer. The bedload, on the other hand, is calculated directly from (2.18). The results in figure 20 show that, for a single sand wave in the 3D stage (in this case after 400 s), the bedload and suspended load contributions to the total sediment load are 83 % and 17 %, respectively. During the 2D stage (after 200 s in this case), the bedload and suspended load contributions comprise 94 % and 6 % of total sediment load, respectively. These results agree with the study of Andreotti *et al.* (2011) in which, for grains with $w_s/U \ll 1$, they proposed that most of the sediment load is concentrated near the bed and that the bedload is the main contribution of the total load. In our study, we observe that, during the 2D stage when the suspended sediments are not completely entrained, the sediment concentration is more concentrated near the bed and therefore our results show only a small contribution of suspended load (6 %). As the turbulent flow near the bed is able to entrain more sediment into suspension, however, the contribution of the suspended load increases significantly to 17 % as sand waves develop into their 3D stage. Thus the total sediment load that

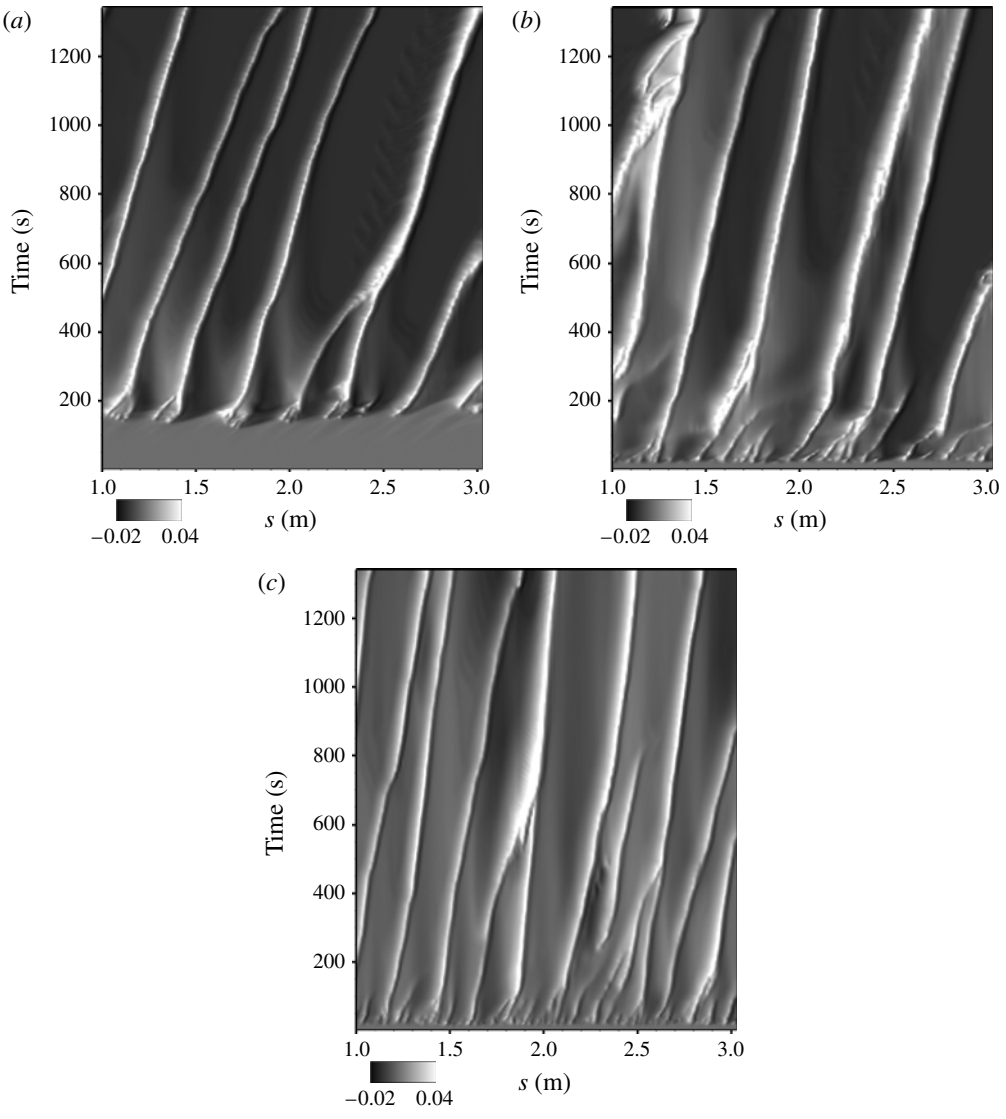

FIGURE 21. Calculated temporal evolution of contours of bed elevation along the arclength coordinate s showing the propagation of sand waves along the centreline of the channel computed on grid systems (*a*) A, (*b*) B and (*c*) C.

gives rise to the development of the sand wave pattern comprises both suspended load and bedload, and neglecting either of these contributions can lead to considerable errors. This finding is consistent with the previously discussed effects of stratification, which become increasingly more significant at later stages (see figure 8) when the concentration of suspended load in the water column increases.

To summarize many of the characteristics of the simulated sand waves in a single plot and present yet another comparison between the solutions obtained on the three grid systems, A, B and C, we plot in figure 21 contours of bed elevation during the first 25 min of the simulation in s–t form. The horizontal axis s in this figure is the arclength along the channel centreline within the sand wave observation window,

the vertical axis t measures time since the start of the coupled simulation, and the contours shown are those of the instantaneous bed elevation $z = z(s, t)$. Such plots are used extensively to characterize the spatial and temporal evolution of bedforms, because they provide an effective way to illustrate a number of important physical phenomena (MacVicar *et al.* 2006; Coco *et al.* 2007; Escauriaza & Sotiropoulos 2011*a*). For example, the slope of the characteristic lines that emerge in such a plot is inversely related to the sand wave celerity, while the horizontal spacing of the topography contours along $t = \text{const.}$ lines provides the wavelength of sand waves. It is evident from figure 21 that on all three grid systems bed features of various sizes and celerities appear and evolve with time. A well-known feature of sand waves, which has been observed in many experiments (see e.g. Coleman & Melville 1994; Venditti & Church 2005), is that the celerity of bedforms decreases with time (also see figure 15*c*). This feature is clearly evident in figure 21 by the continuously steepening upward slope of the characteristic lines. Fast-travelling small-scale sand waves are seen to initially appear and merge to form larger-scale slower-travelling sand waves. In particular, the three different stages of sand wave development that we already mentioned in previous sections of this paper can be readily identified in figure 21, especially on the two finest meshes. The first stage ($t <\sim 120$ s), when the sequence of cross-hatch patterns, chevrons and incipient crestlines appear on the bed, is clearly evident by the fine structure of the contours observed during this interval in figure 21(*b*,*c*). The quasi-2D stage of the process is also evident in figure 21, by the steepening of the characteristic lines in the interval $\sim 120 < t < \sim 600$ s, as is the onset of the 3D quasi-equilibrium stage occurring for $t > 600$ s and marked in figure 21 by yet another steepening of the slope of the characteristic lines. Finally, this figure can also serve as an effective measure for quantifying the grid sensitivity of the computed sand waves. It is evident from figure 21(*a*), for instance, that, as we have already discussed above, grid A is far too coarse to accurately capture the first stage of bed evolution dominated by small-scale cross-hatch and chevron features. While it takes longer until the bedforms initiate in this grid, however, it is apparent in figure 21(*a*) that, as soon as they appear, they grow very fast, yielding patterns that are broadly similar to those observed on the two finer grids. Finally, while both grids B and C can capture the fine-scale early-time bed features, figure 21 clearly shows that on grid C the simulated sand waves evolve faster than in the other two grids, which is in better overall agreement with the measurements.

5.3. *Coupled bed–flow interactions*

Having established in the previous section that the simulations are able to capture most features of the measured bed instability and subsequent growth of sand waves with reasonable accuracy, we now turn our attention to elucidate the physics of the coupling between the turbulent open channel flow and the mobile sand bed. The main objective of this section is to provide novel insights into the hydrodynamic processes that drive the complex morphological features we discussed in the previous section. Specifically, we seek to probe questions that have been at the centre of extensive debate in the literature, including, among other things: the linkage between coherent structures in the turbulent boundary layer and the initial bed instability (Colombini 2004; Venditti & Church 2005; Venditti *et al.* 2006; Chou & Fringer 2010; Omidyeganeh & Piomelli 2013*a*,*b*), the role of flow separation off sand wave crestlines as a means for sand wave migration (Kostaschuk 2000; Schindler & Robert 2004; Best 2005; Colombini & Stocchino 2012) and the origin of low-frequency coherent structures rising to the

water surface, also known as surface 'boils' (Jackson 1976; Yalin 1992; Venditti & Bennett 2000; Best 2005).

With the previously discussed grid-sensitivity studies and numerical experiment in which stratification effects were neglected (see § 5.2.1), we presented evidence in support of the hypothesis that near-bed coherent structures in the turbulent flow over the initially flat, mobile sand bed are responsible for initiating the bed instability (Grass 1970; Venditti *et al.* 2006). If this is indeed the case, however, it is reasonable to further hypothesize that the distinct linear cross-hatch patterns that appear on the bed at the onset of the instability (see figures 5*a* and 4*a*) are the imprints on the sand bed of near-bed coherent structures. Turbulent sweep events, characterized by fourth-quadrant (Q4) velocity fluctuations with $u' > 0$ and $w' < 0$ and associated with the interaction of hairpin vortices in the turbulent boundary layer with the wall, have long been hypothesized as the main mechanism for destabilizing the bed (Grass 1970, 1971; Coleman & Melville 1994; Best & Kostaschuk 2002). Venditti & Church (2005) presented some quantitative evidence in support of this hypothesis by showing that the average or dominant size of eddies in the initial (flat bed) flow at 5 mm above the bed (located at wall unit of $z^+ \sim 150$) are essentially identical to the average size of the lines of the cross-hatch pattern. It has yet to be demonstrated, however, that instantaneous sweep events form patterns that correlate with the distinct cross-hatch or chevron striations observed during the early stage of the bed instability (Venditti & Church 2005). To explore this possibility we first use our simulation results on grid C and consider the fluctuating velocity field at the first horizontal plane off the bed (located at $z^+ \sim 23$) at time $t \sim 4$ s. At this instant in time the bed is still flat and shows no signs of instability. To identify the areas on the bed experiencing instantaneous sweeps, we define the sweep detection function (SDF) F_s defined as follows:

$$F_s = \begin{cases} 1 & \text{if } u' > 0 \text{ and } w' < 0, \\ 0 & \text{elsewhere.} \end{cases} \tag{5.3}$$

In figure 22 we plot a snapshot of the SDF constructed by time averaging the instantaneous velocity field over a time interval of 4 s (from $t = 0$ until $t = 4$ s) and subtracting the mean velocity field from the instantaneous velocity field to calculate the fluctuating velocity components. We also plot in this figure the fluctuating shear velocity (which is non-dimensionalized with the mean flow velocity) and show for the sake of reference the cross-hatch patterns that emerge on the bed a few seconds later within the same observation window. The dimensionless fluctuating shear velocity (u'_*/U) in figure 22(*b*) is also computed by time averaging the instantaneous shear velocity over a time interval of 4 s and subtracting the mean velocity field from the instantaneous velocity. It is clearly evident from figure 22 that both the SDF and the fluctuating shear velocity exhibit cross-hatch patterns very similar to those appearing on the bed during the early stage of instability. The length of most of the linear features comprising the cross-hatch in the shear stress and SDF fields are of the order of 5–7 cm, which compares well with the length of lines that appear on the bed. The angles the lines in the SDF and fluctuating shear velocity contours form with the channel axis in figure 22 range from 35° to 45°, which is close to the average angle of the cross-hatch patterns (35°–40°). To the best of our knowledge, these results represent the first evidence that near-bed synchronized sweeps are correlated in terms of both length and shape with the early cross-hatch patterns on the sand bed. We thus argue that, when considered in tandem with the evidence presented by Venditti & Church (2005), our results make a conclusive case that near-bed coherent structures

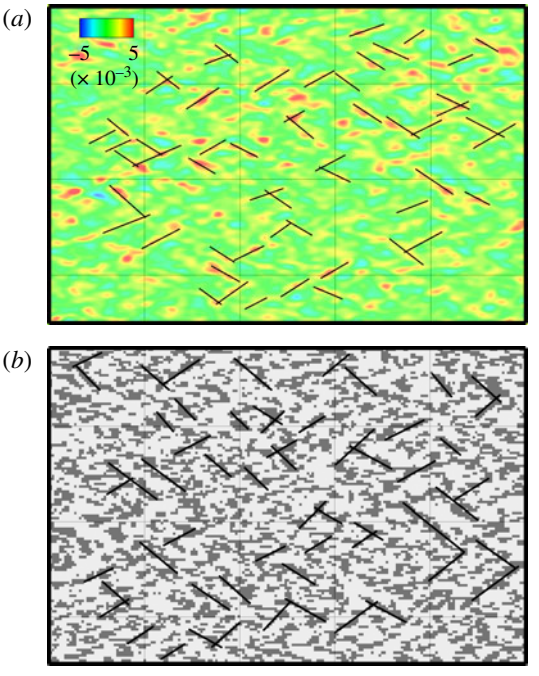

FIGURE 22. Computed contours of (*a*) the dimensionless fluctuating shear velocity and (*b*) sweep detection function F_s (5.3) over a window in the centre of the channel and near the bed surface where $z = \|\boldsymbol{\delta}_{BL}\|$. The bed features associated with this instant in time ($t \sim 4$ s) are the cross-hatch patterns with an amplitude of $\sim 2d_{50}$ and wavelength of ~4–7 cm, which are consistent with the scale of the structures shown in this figure (see the oblique lines). Flow is from left to right and the grid lines are 0.115 m apart along both directions. The black solid lines are provided to better identify some of the regions of linear cross-hatch features in the contour plots.

are responsible for destabilizing the bed and for giving rise to the cross-hatch and chevron shapes observed in both the simulations and the experiments during the very early stage of bed evolution.

In order to further support our hypothesis regarding the linkage between near-bed coherent structures and bedform initiation, we use our simulation results on the finest grid system, grid D, and track simultaneously the evolution of the turbulent sweep events on a 2D plane above the bed and the bed deformation for the first 22 s of the simulation. We note once again that the fluctuating quantities and SDF at any time instant $t = t_f$ are obtained by time averaging the instantaneous values over a time interval of $0 < t < t_f$ and subtracting the mean value (over the time interval) from the instantaneous quantity. In figure 23 we further mark in the contour plots of the instantaneous SDF (5.3) the location where the deforming bed rises to intersect and protrude through the horizontal plane, which is located at the leading edge of the bedload layer ($z = \delta_b$). In other words, the white patches in figure 23 mark the intersection of the sediment defects (areas of localized deposition of sediment) with the horizontal plane and can be used to readily track the growth and propagation of these defects in relation to the instantaneous sweep events. To help interpret these results, we note that the dark-coloured patches in the F_s contours mark areas where $F_s = 1$, which by definition denotes Q4 events, whereas light-coloured patches

are areas where $F_s = 0$ (regions where no sweeps are present). In other words, the dark patches in these plots are regions where the vertical velocity component of the fluctuating velocity vector is directed towards the bed. One could thus argue that regions where $F_s = 1$ are areas where local micro-scour events could first originate on the bed because: (i) the direction of the fluctuating velocity vector in these regions is towards the bed and is favourable for inducing scour; and (ii) Q4 events carry high-momentum fluid towards the bed and tend to locally increase the bed shear stress, which could create conditions suitable for initiation of motion (see subsequent discussion about the role of shear stress fluctuations). For sediment continuity to be satisfied, and assuming that during the initial stages of the process only a negligible amount of sediment is suspended (see the discussion of figure 20), the sediment displaced outside of these small scour holes will tend to accumulate in their vicinity, giving rise to the formation of small sediment defects. We also note that, as soon as some of these defects and surrounding scour holes form on the bed, they modify the local bed geometry and can help intensify the local structure of near-bed fluctuations in a manner that promotes further scour and deposition events, causing the defects to grow and propagate (see subsequent discussion on this in relation to figure 24). Based on this heuristic analysis we can thus hypothesize that sediment defects will first appear on the bed in regions where $F_s = 0$ and adjacent to patches where $F_s = 1$. As seen in figure 23 our computed results confirm this hypothesis. During the first 5–6 s of the simulation, any defects on the bed are too small to protrude through the horizontal plane of figure 23. During that time the contours of F_s exhibit the characteristic cross-hatch pattern that is also seen in the bed elevation contours at early times previously shown in figure 5(*a*) and also discussed by Venditti & Church (2005). The cross-hatch patterns in F_s (figure 23*a*,*b*) are seen to form angles between 40° and 60° with the horizontal, which are similar to the angles observed in the cross-patterns of the bed elevation during the first few seconds of the bed instability (Venditti & Church 2005). At approximately 6 s (see figure 23*c*), the first sediment defects appear on the horizontal plane, where F_s is plotted in the form of small circular nodes of sediment. It is evident from this figure that essentially all sediment defects are fully contained within areas where $F_s = 0$ and are almost always outlined, at least in part, by the boundary of areas where $F_s = 1$. This trend is seen to clearly persist for several seconds of the simulation, until the sediment defects and associated areas of scour on the bed become large enough to start drastically changing the structure of near-bed velocity fluctuations. This appears to happen after approximately 15 s when the F_s contours begin to lose the characteristic cross-hatch pattern they exhibited at early times when the bed was essentially flat.

Another important finding that is evident from figure 23 is that, as soon as the sediment defects appear at the horizontal plane, they begin to grow in size as they are advected downstream and ultimately begin to merge with surrounding defects to form the chevron features observed in the bed elevation at later times (see figure 5*b*). This process is highlighted in figure 23 by marking a few such defects (which are circled) so that their fate can be clearly tracked with time. A closer look at this figure further shows that essentially all defects that initially appear on the horizontal plane have the same fate; they are advected downstream by the near-bed flow, grow in size and ultimately merge to start the process of bedform initiation.

To underscore the importance of fluctuating shear stress magnitude in the formation and subsequent propagation of sediment defects, we plot in figure 24 the contours of instantaneous shear stress at the same plane, location and instants in time as used in figure 23 for the F_s contours. As in figure 23, we also superimpose in

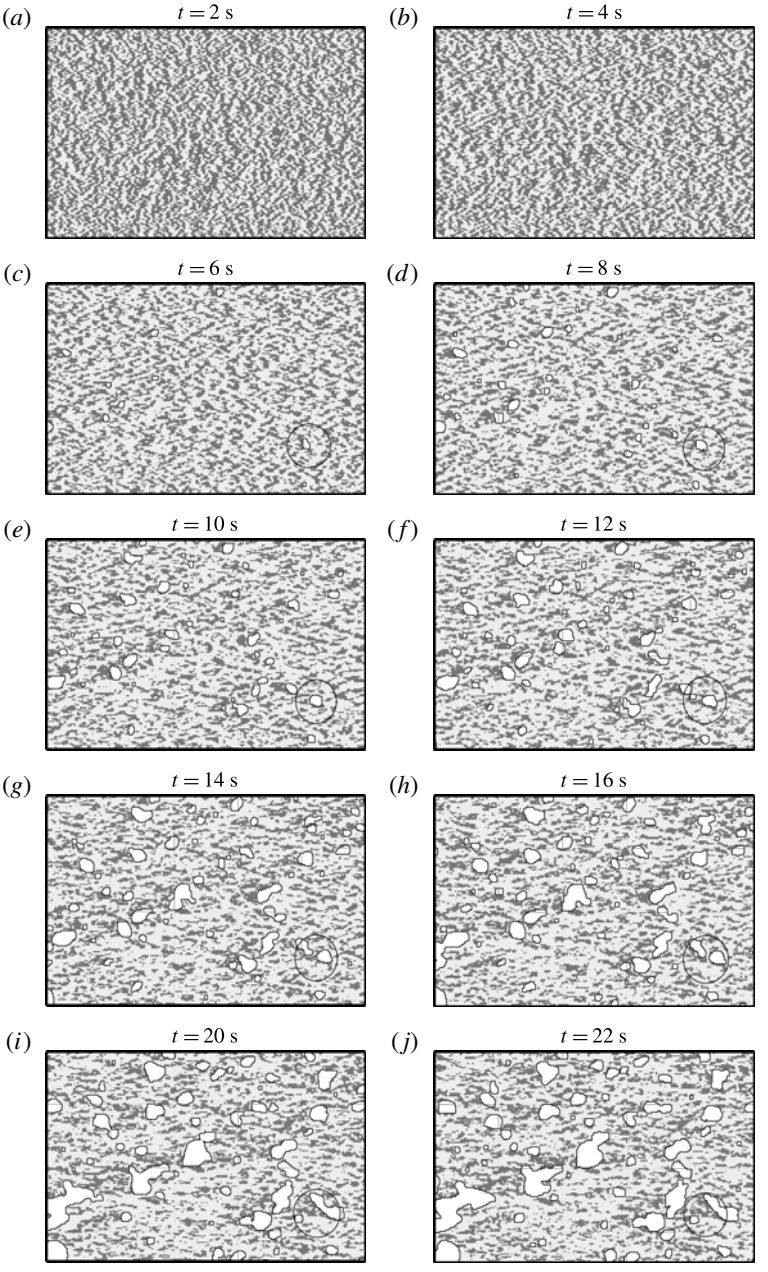

FIGURE 23. Computed (on grid D) contours of the instantaneous sweep detection function F_s (5.3) on a horizontal plane located at $z = \|\boldsymbol{\delta}_{BL}\|$ superimposed with the intersection of the bed surface with that plane (white spots). The circles in some of these figures are used to track in time a few selected areas of local deposition, which grow, merge and start forming the incipient sand waves. Flow is from left to right and the grid lines are 0.115 m apart along both directions.

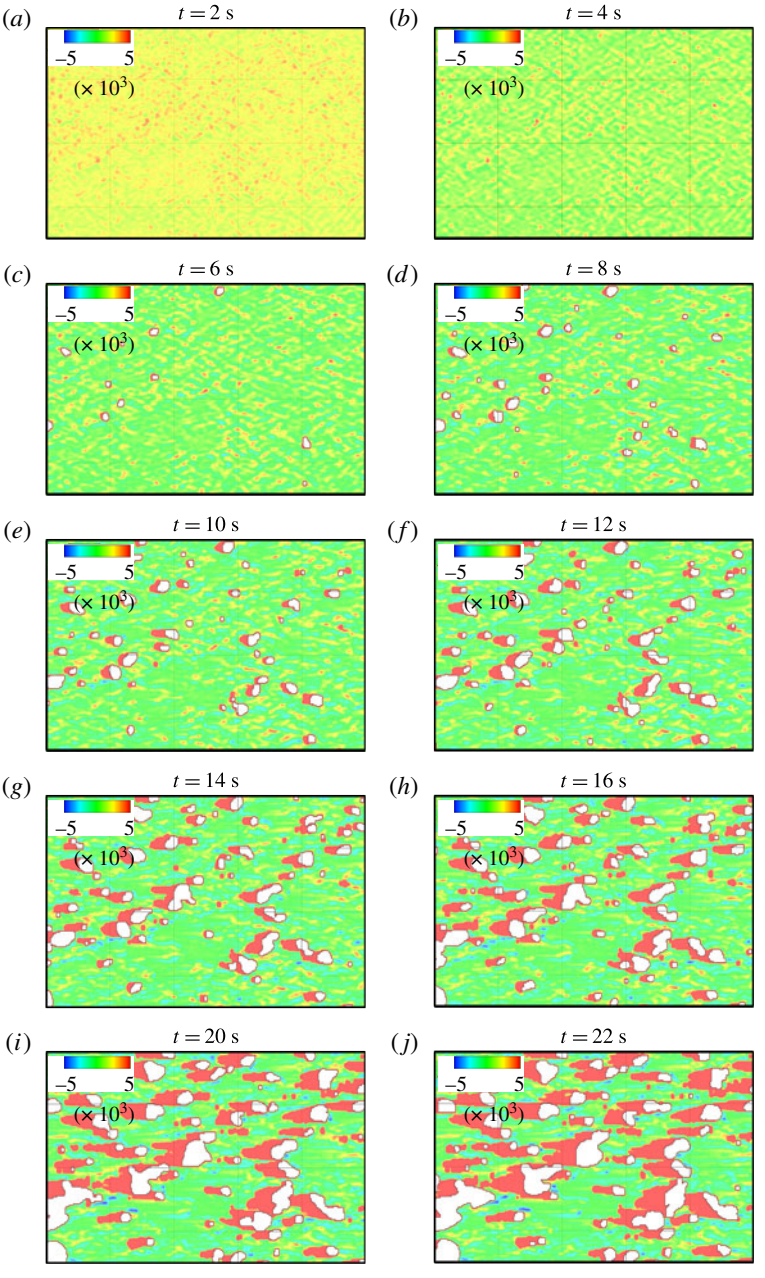

FIGURE 24. Computed (on grid D) contours of the dimensionless fluctuating shear velocity on a horizontal plane located at $z = \|\boldsymbol{\delta}_{BL}\|$ superimposed with the intersection of the bed surface with that plane (white spots). Flow is from left to right and the grid lines are 0.115 m apart along both directions.

figure 24 the intersection of the bed with the plane at various instants in time. It is readily apparent from figure 24(*a*,*b*) that the regions of the near-bed flow where the fluctuating shear stress is high are organized in the same cross-hatch pattern as the F_s function in figure 24. As previously discussed, this should not be surprising, since

fluctuating sweep events transport high-momentum fluid towards the bed and increase the local fluctuating shear stress. It is also evident from figure 24 (see snapshots at 6–10 s) that sediment defects occupy regions of low fluctuating shear stress but along their stoss side are bounded by regions of high fluctuating shear stress. This finding is entirely consistent with our previous discussion regarding the role of sweeps to promote local scour events on the bed and lead to the formation of adjacent sediment defects. Figure 24 also illustrates clearly the mechanism via which sediment defects grow and propagate. Note, for instance, that, as soon as the defects appear on the plane, they start propagating downstream ahead of a trail of high fluctuating shear stress that follows their motion. These distinct regions of high fluctuating shear stress in the stoss side of the defects, which also coincide with sweep events as shown in figure 23, mark regions of local scour events that supply the sediment that helps grow, advect and sustain the defects. As we observed for the F_s contours, the fluctuating shear stress magnitude contours begin to lose their cross-hatch pattern, starting at 10 s, when the defects have grown enough to be able to affect the local flow. Even at these later instants in time, however, the pockets of high fluctuating shear stress always trail sediment nodes. This finding underscores and further clarifies the previously discussed process of local scour at the stoss side (marked by high fluctuating shear stress) of the sediment nodes followed by deposition at their lee side that causes the bed features to grow and propagate. In subsequent sections of this paper we will discuss how essentially the same mechanism of scour at the stoss side and deposition at the lee side is responsible for the growth and migration of large-scale sand waves when they appear. The results we have presented in this section, however, are quite striking, as they also show that such mechanism appears to be at work during the early stages of bed instability. What changes are the structure, scale and dynamics of coherent structures near the bed that drives such phenomena. During early stages the process of bed deformation is dominated by the near-bed sweeps that occur in the initially flat bed open channel flow. The bed responds quickly to the flow, and sediment nodes appear as the result of sweep events in the fluctuating velocity field that increase the fluctuating shear stress locally, giving rise to localized scour events and associated regions of deposition for sediment continuity to be satisfied. As the bedforms grow and self-organize to form dunes, they migrate much slower than the time scale of the flow and, as we will subsequently show, induce large-scale coherent structures that act to augment scour at the stoss side and promote deposition at the lee side.

We now consider the coupled evolution between the bed and the flow at subsequent instants in times by showing in figures 25–27 various instantaneous perspectives of the simulated velocity magnitude, spanwise vorticity and suspended sediment concentration fields. Figure 25 shows the flow and bed at $t = 20$ s during the transition from chevrons to incipient crestlines. It is evident from the instantaneous velocity contours shown in figure 25 that the emerging sand waves act as roughness elements causing the boundary layer to thicken and giving rise to localized pockets of low streamwise momentum. At this stage of the evolution of the flow, the amplitude of sand waves is of the order of 0.5 cm (i.e. approximately smaller that 3 % of the flow depth) and crestlines have just begun to emerge. Consequently, the sand waves are not yet large and coherent enough to cause a major reorganization of the flow, which at this stage resembles flow over a rough flat wall. The coupled interaction between the turbulent flow and the mobile sand bed, however, is seen in figure 25 to have a profound impact on the suspended sediment concentration. Sediment is transported from the bed upwards by the coherent structures, providing the sediment

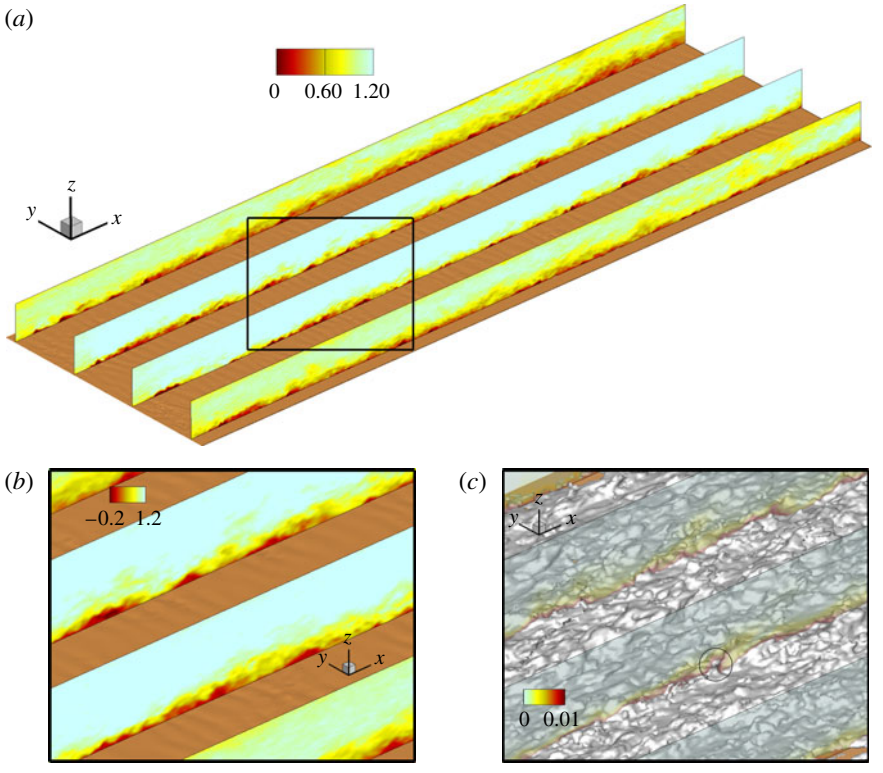

FIGURE 25. (Colour online) Computed colour maps of instantaneous (*a*) velocity magnitude (non-dimensionalized by mean flow velocity), (*b*) streamwise velocity component (non-dimensionalized by mean flow velocity) and (*c*) suspended sediment concentration (volume fraction) superimposed with the concentration isosurface (=0.01). The rectangular box in (*a*) shows the location of the windows in (*b*) and (*c*). Velocity and concentration fields are shown along five and four longitudinal sections, respectively, that are superimposed over the bed geometry at $t = 20$ s. Flow is from bottom left to top right.

supply mechanism for mobilizing the bed and driving the subsequent evolution of sand waves. While most suspended sediment at this stage remains confined close to the bed, the resulting concentration field is highly 3D and is dominated by intermittent and localized events during which masses of sediment are locally ejected from the bed into the outer flow (see the circle area in figure 25*c*). The overall shape of the concentration isosurface, which is characterized by streaks and loops inclined forwards and rising upwards, suggests a close correlation between sediment transport and coherent structures in the near-bed turbulent boundary layer. It is also clear from figure 25 that by $t = 20$ s a spatially heterogeneous layer of suspended sediment has formed above the bed, with pockets of heavier sediment-laden fluid lifted off the bed and into areas of lighter, clear fluid, thus setting up an active stratified layer. Based on the results shown in figure 8, it is approximately after 20 s of bed evolution when measurable discrepancies emerge between the bed elevation computed with the unstratified and the stratified formulations. The results shown in figure 25 explain why this is so. While, at the very early stages of bed evolution (when cross-hatch and chevrons appear), near-bed coherent structures serve as the only mechanism to

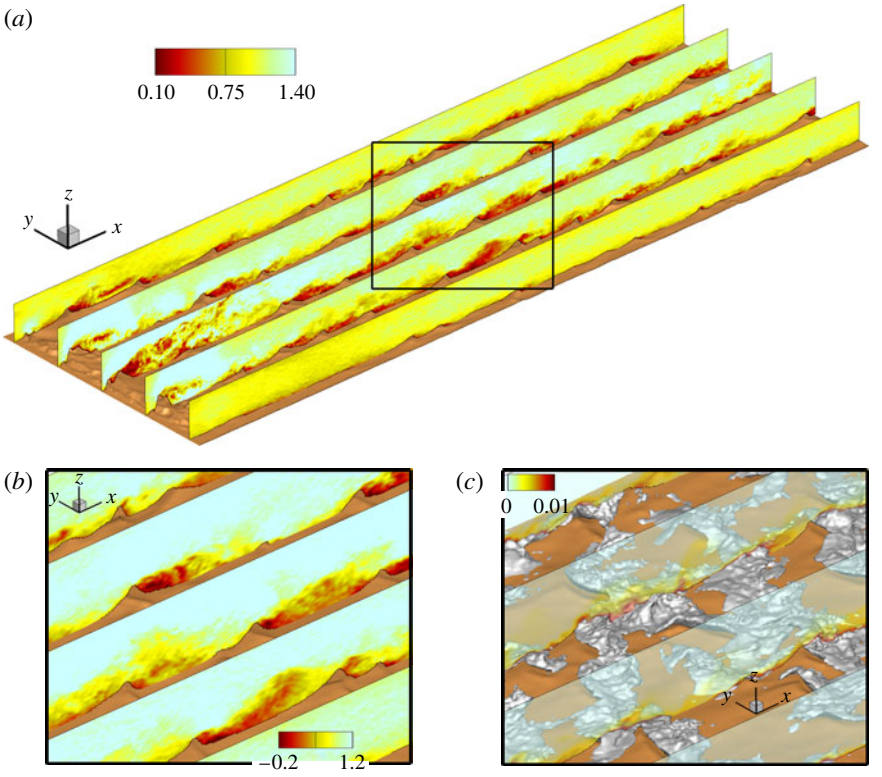

FIGURE 26. (Colour online) Computed colour maps of instantaneous (*a*) velocity magnitude (non-dimensionalized by mean flow velocity), (*b*) streamwise velocity component (non-dimensionalized by mean flow velocity) and (*c*) suspended sediment concentration (volume fraction) superimposed with the concentration isosurface (=0.01). The rectangular box in (*a*) shows the location of the windows in (*b*) and (*c*). Velocity and concentration fields are shown along five and four longitudinal sections, respectively, that are superimposed over the bed geometry at $t = 200$ s. Flow is from bottom left to top right.

destabilize the bed and initiate the entrainment of suspended sediment into the flow, as soon as sediment comes into suspension, the energetic near-bed coherent structures cause the formation of a spatially heterogeneous and locally unstable stratified layer as heavier sediment-laden fluid is locally lifted off the bed and ejected into the outer flow. Stratified layer instabilities, therefore, begin to become important at this point, explaining why the discrepancies between the stratified and unstratified simulations become evident at approximately this time. Therefore, our results make a strong case that both coherent structures in the flow and stratified layer instabilities are responsible for the destabilization and evolution of the bed (see also Venditti & Church 2005). The former dominate during the early stages of the process and serve to create the unstable and spatially heterogeneous stratified layer above the bed, which is required for activating the latter.

The flow patterns shown in figure 26 are at $t = 200$ s when quasi-2D sand waves have emerged with amplitude of ∼2 cm and wavelength of ∼4 to 14 cm. Comparing this figure with figure 25, it is clear that the sand waves at this latter instant in

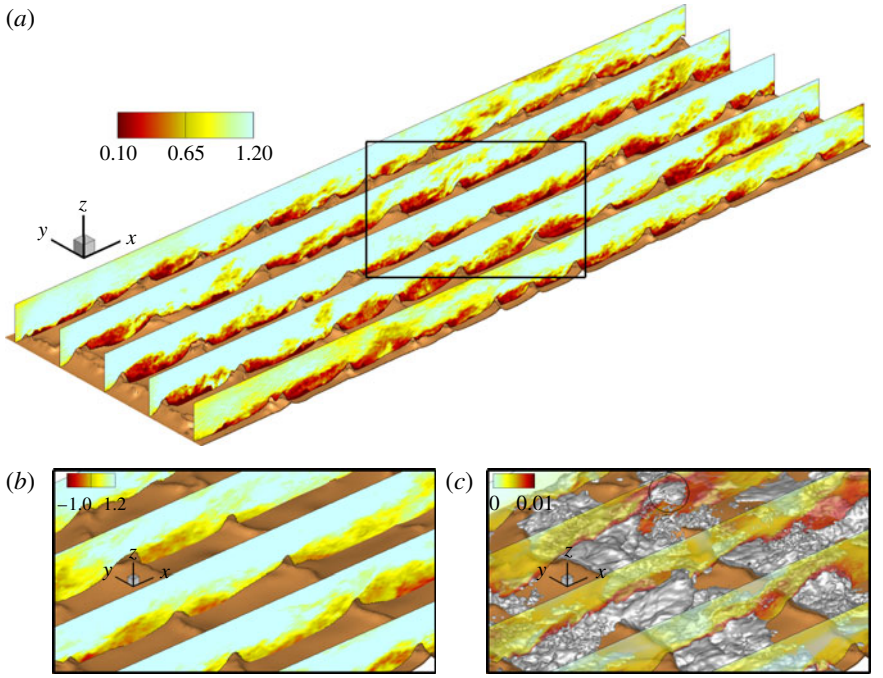

FIGURE 27. (Colour online) Computed colour maps of instantaneous (*a*) velocity magnitude (non-dimensionalized by mean flow velocity), (*b*) streamwise velocity component (non-dimensionalized by mean flow velocity) and (*c*) suspended sediment concentration (volume fraction) superimposed with the concentration isosurfaces (=0.01). The rectangular box in (*a*) shows the location of the windows in (*b*) and (*c*). Velocity and concentration fields are shown along five and four longitudinal sections, respectively, that are superimposed over the bed geometry at $t = 800$ s. Flow is from bottom left to top right.

time have grown large and organized enough to drastically alter the flow patterns near the bed. The instantaneous velocity and vorticity contours suggest that the flow is dominated by intense shear layers and vortex roller structures induced by KH instability of the shear layers emanating from sand wave crestlines. The effect of sand waves at this stage is also very pronounced in the suspended sediment field. The contours and isosurface of concentration suggest that suspended sediment, which is eroded by the accelerating flow over the crestlines, is trapped by the recirculating flow and deposited in the lee side of the sand waves. This process is essentially consistent with what has been hypothesized in the literature as the mechanism for dune migration (Yalin 1992; van Rijn 1993; Coleman & Melville 1994; Best 2005). Such processes are evident in figure 26 and become even more pronounced in figure 27, which shows the flow at $t = 800$ s. Dunes that are fully grown and well organized in the spanwise direction have now emerged on the bed, which protrude higher into the flow, intensify shear-layer instabilities from crestlines and give rise to intermittent, massive separation events that drive the transport of large amounts of sediment from the bed towards the free surface. One such suspended sediment transport event is clearly shown in figure 27, which shows a mass of sediment having detached from a large pocket of suspended sediment trapped in the lee side of a dune and getting advected towards the free surface (see the circled area in

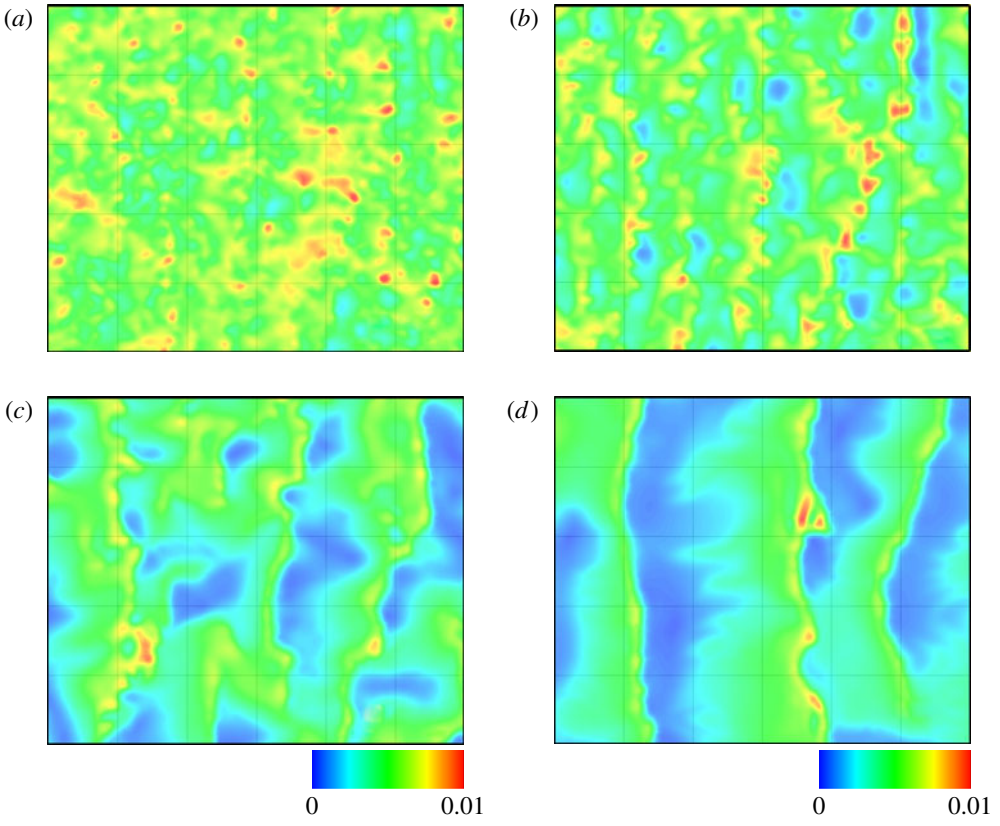

FIGURE 28. Computed colour map of instantaneous dimensionless shear velocity (u_*/U) near the bed surface where $z = \|\boldsymbol{\delta}_{BL}\|$ at (*a*) $t = 50$ s, (*b*) 100 s, (*c*) 300 s and (*d*) 1000 s over a window at the centre of the channel. High shear velocity near the nodes of the chevrons at $t = 50$ and 100 s are clearly shown in (*a*) and (*b*). Rearrangement of bed shear stress from initial stage to 2D and 3D stages of sand development can be clearly seen in these figures. Flow is from left to right and the grid lines are 0.115 m apart along both directions.

figure 27*c*). Such major suspended transport events are expected to dramatically attenuate the importance of stratified flow effects at this stage of the process, since they set up large regions of locally unstable stratification, which would modify the structure of turbulence and impact sediment transport and sand wave migration. This finding has been further reinforced by examining the relative contributions of bedload versus suspended sediment load in the flow, with the latter shown to be very small during the early stages of bed evolution, while the former increases during the 3D stage of the sand wave evolution (see figure 20 and the related discussion in § 5.2.4).

To further illustrate the role of flow separation from crestlines as the key mechanism for sand wave migration, we plot in figure 28 snapshots of the instantaneous shear velocity contours on the bed (non-dimensionalized with mean flow velocity). It is evident from this figure that, throughout the various stages of the process, regions of high shear stress occur at the stoss side of the crestlines while low shear stress occurs at the lee side. These results are consistent with the previously discussed features of suspended sediment motion. The high shear stress on the stoss side causes sediment

erosion and injection into the flow, whereas the separated flow region in the lee side promotes sediment trapping and deposition, causing the sand wave to migrate in the streamwise direction and rearrange.

A major characteristic of turbulent open channel flow over dunes is the aperiodic and highly intermittent appearance of free surface 'boils' (Muller & Gyr 1986; Best 2005; Omidyeganeh & Piomelli 2013*a*,*b*). These are upwelling events during which coherent structures in the flow advect near-bed fluid and sediment away from the bed, making distinct marks, or 'boils', on the free surface. The recent LES of Omidyeganeh & Piomelli (2013*a*,*b*), who simulated flow over fixed dunes, showed that, in agreement with previously proposed conceptual models of coherent structures (Best 2005), boils are the result of horseshoe-shaped vortical structures that rise away from the bed and impinge at the surface. As shown in figure 29, which depicts snapshots of an instantaneous isosurface of the Q criterion (=30) coloured with the distance from the bed, our simulations also capture the emergence of large-scale horseshoe vortices. This figure as well as video animations (not included herein) that we have created, depicting the simultaneous evolution of coherent structures in the flow and the sand waves, show that such horseshoe structures appear in the flow as soon as chevrons and incipient crestlines emerge on the bed. The appearance of such bed features causes local separation in the lee side of sand waves and the emergence of distorted KH rollers in the spanwise direction (due to the complex sand wave morphology), which quickly evolve into the horseshoe (or hairpin) structures observed in figure 29. The heads of the horseshoes grow upwards while their legs are stretched in the streamwise direction by velocity gradients in the local flow and intensify. As the amplitude of sand waves grows, so do the strength and size of horseshoes, which ultimately become strong enough not to be dissipated in the water column and are able to rise all the way to the free surface, causing the distinct 'boil' events. Such events are intermittent and, as we will subsequently show, become more frequent and pronounced when the 3D stage of bed evolution has been reached. To further elucidate the effects of upwelling events on the free surface flow, we plot in figure 30 instantaneous velocity magnitude, vorticity magnitude and suspended sediment concentration contours on a horizontal plane located immediately below the free surface. This figure clearly shows that surface boils are characterized by low flow velocity, regions of large suspended sediment concentration and patches of intense vorticity magnitude arising as sediment-carrying coherent structures reach and interact with the free surface. It is however important to mention that bursting of flow quantities (e.g. velocity and vorticity in figure 30*a*,*b*) and sediment concentration (figure 30*c*) do not show up at the free surface at the same time because there is a time lag between the two. The eruption of sediment concentration at the free surface follows the eruption of coherent structures in the flow with a time lag. This is indeed an interesting topic for future research, as it relates to fundamental differences between Lagrangian and Eulerian coherent structures in the flow, with the former arising as a result of the advection of suspended sediment to the free surface.

To quantify the frequency of occurrence and intensity of upwelling events at the free surface, in figure 31 we plot an s–t diagram for the instantaneous vorticity magnitude along the channel centreline and at 5 mm below the free surface. This figure summarizes in a succinct manner many of the underlying flow processes and also contains important quantitative information about their associated spatial and temporal scales. First note that, since vorticity is advected by the flow, the slope of the characteristic streaky patterns that emerge in this diagram is inversely related to the local mean flow velocity. As seen in this figure, the slope of the

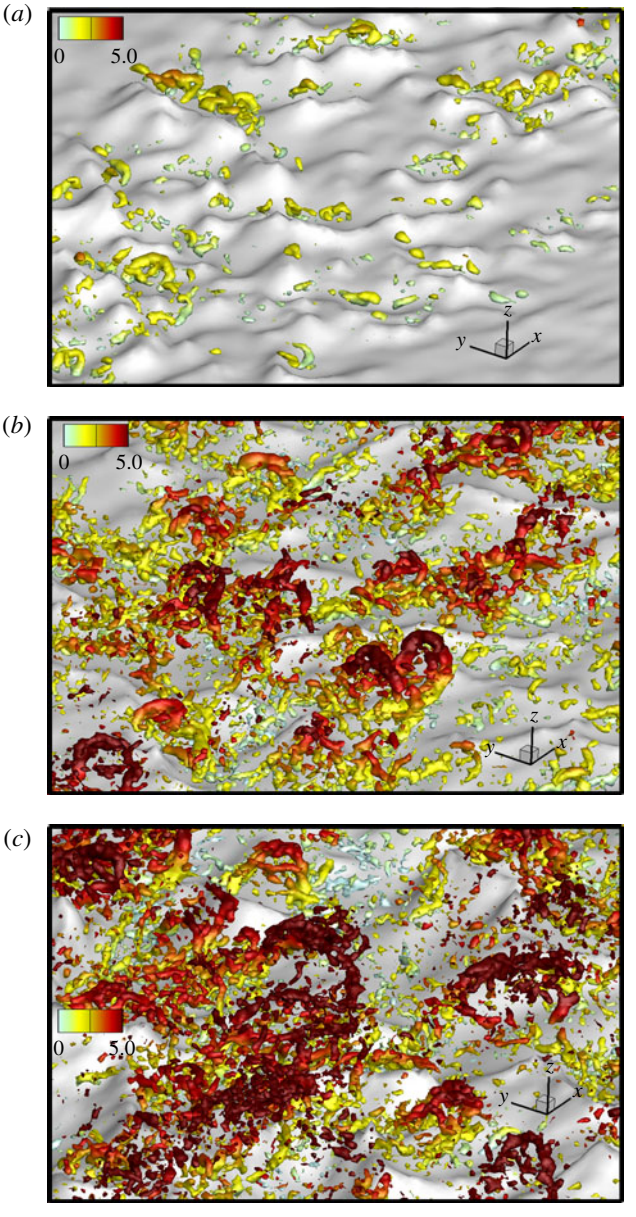

FIGURE 29. (Colour online) Computed instantaneous isosurfaces of Q criterion (=30) at (*a*) $t = 100$ s, (*b*) 400 s and (*c*) 700 s superimposed over the bed geometry at the pertaining time instants. The window is the same as the rectangular box in figure 26(*a*). The isosurfaces are coloured by contours of flow depth (in cm). Flow is from bottom left to top right.

characteristics decreases with time, which is consistent with the acceleration of the mean flow near the free surface occurring as sand waves emerge and reduce the effective cross-sectional area of the channel and the flow velocity near the bed. More specifically, the changing slope of the characteristics in figure 31 suggests that at equilibrium the mean velocity at the free surface is approximately 35 %

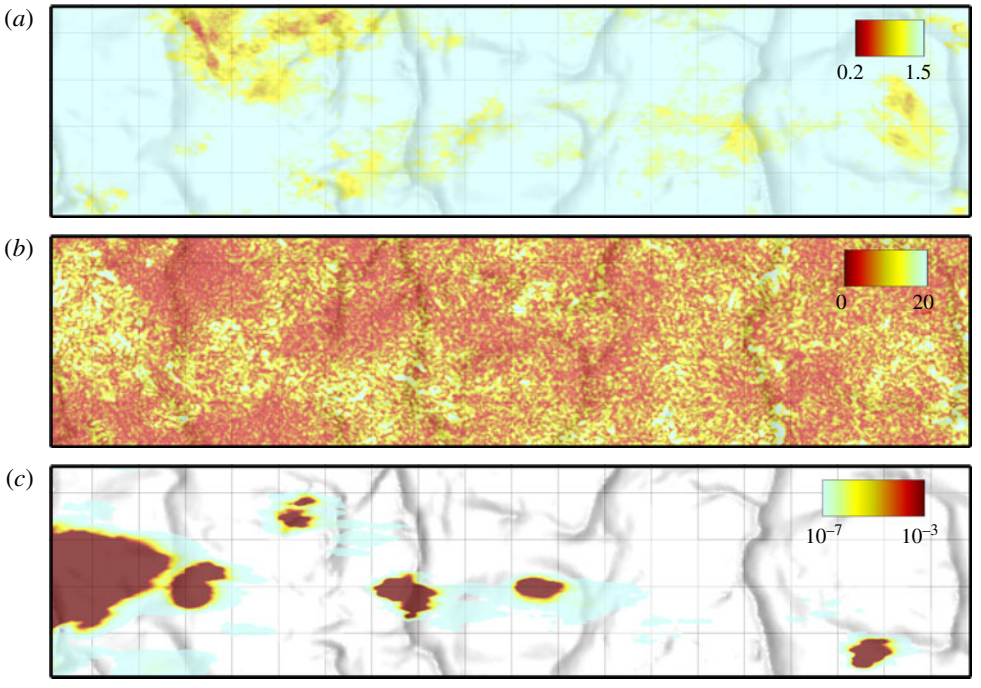

FIGURE 30. (Colour online) Computed contours of instantaneous (*a*) non-dimensionalized velocity magnitude, (*b*) non-dimensionalized vorticity magnitude and (*c*) suspended sediment concentration (volume fraction) at a horizontal plane 5 mm below the free surface and after $t = 500$ s. The bed surface geometry associated with the same instant in time is also shown below the water free surface. The selected window is focused on the centre of the flume. The sediment concentrations below 10^{-7} are cut off. Flow is from left to right and the grid lines are 0.115 m apart along both directions.

greater than when the bed is flat. This is broadly consistent with the development of approximately 6 cm high equilibrium sand waves (see figure 15), which can locally reduce the effective cross-sectional area of the channel by as much as 40 %. Another important finding evident from figure 31 is that, based on the overall levels of vorticity magnitude at the free surface, the following three distinct stages of evolution of the vorticity field can be clearly defined: (i) $0 < t < 100$ s, when the vorticity magnitude at the surface is essentially close to zero; (ii) $100 < t < 300$ s, when intermediate values of vorticity develop along with highly intermittent small-size streaks of high vorticity; and (iii) $t > 300$ s, when streaks of high vorticity magnitude grow in size and persist. Based on our previous discussion of bed evolution, it is apparent that the time scales of these three stages correlate well with the various stages of development of sand waves. During the first stage, when only small-amplitude cross-hatch patterns, chevrons and incipient crestlines appear on the bed, the flow near the free surface is not affected by near-bed phenomena and resembles that of the flow in a channel with a flat bed, exhibiting weak vortical structures. As sand waves grow in their 2D and 3D stages, however, horseshoe vortical structures generated at crestlines are able to rise and interact with the free surface (see figure 29), drastically increasing the levels of vorticity magnitude in figure 31. This effect is clearly evidenced by the sharp increase in the level of vorticity magnitude of the streaks occurring at approximately

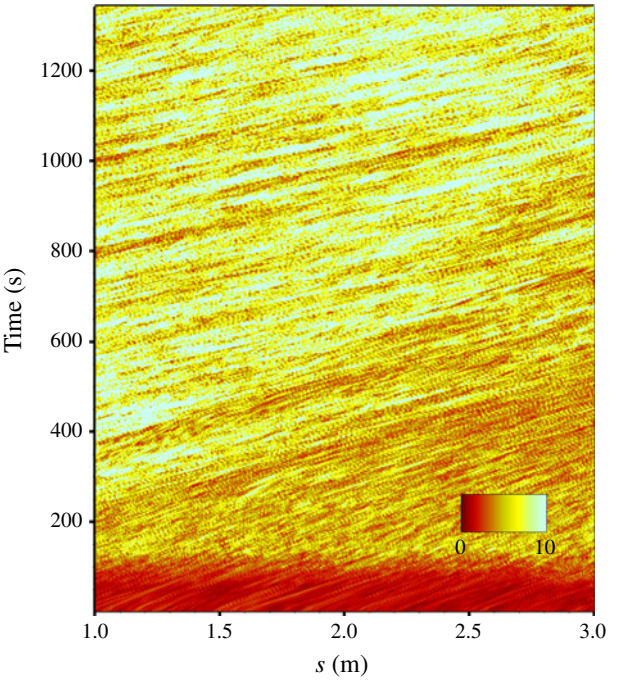

FIGURE 31. (Colour online) Computed contours of non-dimensionalized vorticity magnitude in time along the channel centreline s at an elevation 5 mm below the free surface.

$t = 300$ s, which is roughly when quasi-2D sand waves appear on the bed. Another striking feature that follows from figure 31 is with regard to the average length of the high-vorticity streaks, which is seen to increase continuously in time. In fact the observed length scale agrees reasonably well with the wavelength of bedforms (see figure 15*b*), reaching values as high as 50 cm or greater at later times. Such scaling can be explained by the fact that the size of horseshoes, which dictates the length of their free surface imprints, should correlate with the distance between adjacent crestlines. The larger this distance, the more space horseshoes have to grow and intensify through vortex stretching before they interact with horseshoes generated by downstream crestlines – we present some evidence in support of this assertion in the discussion of figure 32 below. Therefore, the results shown in figure 31 not only help to quantify the interactions between vorticity structures generated by sand waves and the free surface but also show that time series of flow quantities near the free surface have embedded in them information regarding the characteristics of these sand waves. Although not shown herein, similar conclusions can be drawn by considering s–t diagrams of instantaneous velocity magnitude and sediment concentration.

To further elucidate the structure of the flow at instants in time when fully developed dunes have emerged, we plot in figure 32 finite-time-averaged contours and isosurfaces of streamwise velocity, turbulence kinetic energy, spanwise vorticity and sediment concentration. The instantaneous results have been averaged over a time interval of 5 s, which is small enough to assume quasi-stationary dunes. Many of the previously discussed features of the flow become more clear in this figure, including the regions of flow separation from crestlines, the pockets of high turbulence kinetic energy at the unstable shear layers that originate as a result of the

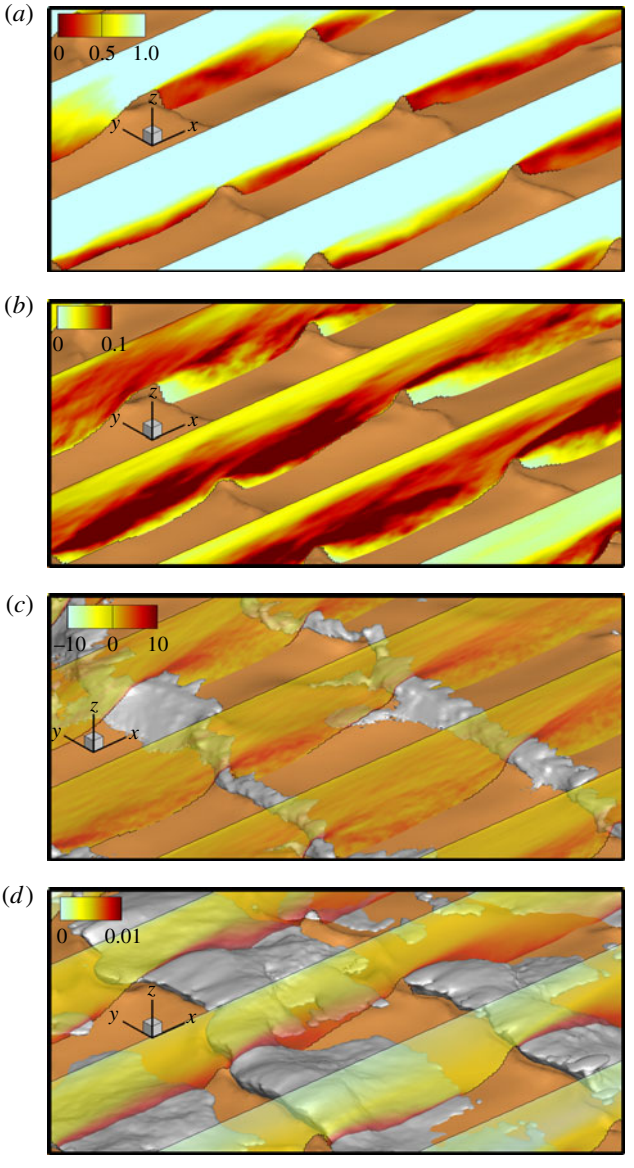

FIGURE 32. (Colour online) Computed contours of finite-time-averaged (*a*) velocity magnitude, (*b*) turbulent kinetic energy, (*c*) spanwise vorticity (plus isosurfaces of spanwise vorticity =15) and (*d*) suspended sediment concentration (plus concentration isosurfaces of 0.01) along five representative longitudinal sections. Time-averaging has been carried out over the time window of $t = 800$ to 805 s. The location of the windows is shown in figure 27(*a*). The quantities are non-dimensionalized with bulk velocity and flow depth. Sections are separated with identical distances, and geometrical scales are tilted. Flow is from bottom left to top right.

recirculating lee flow, the strong organization of vorticity in spanwise rollers along the crestlines, and the systematic and persistent organization of regions of large suspended sediment concentration in the lee side of the dunes. These results further reinforce

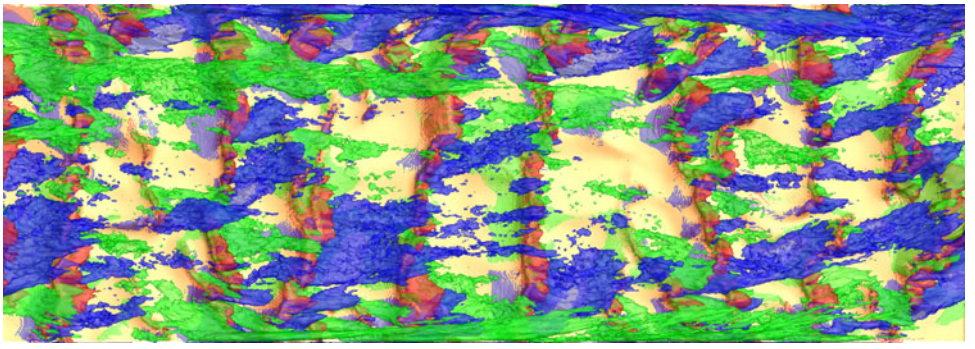

FIGURE 33. Plan view of computed isosurfaces of finite-time-averaged (over the time window of $t = 800$ to 805 s) spanwise vorticity (=8 in red) and streamwise vorticity ($= \pm 1.5$ in blue and green, respectively). Isosurfaces are superimposed over the bed geometry (in gold) at $t = 800$ s. The window covers the entire mobile bed and the flow is from left to right.

our previous discussion regarding the role of flow separation from the dune crestlines, and sediment trapping and deposition in the lee side, as the main mechanism for migration and continuous reorganization of crestlines. It should be noted, however, that the mean vorticity field is rather more complex than that suggested by figure 32, which only shows the spanwise vorticity. This is demonstrated in figure 33, where we superimpose in the same plot an isosurface of spanwise vorticity along with two isosurfaces of streamwise vorticity of equal but opposite sign. While it is clear from the values of the selected isosurfaces that most of the mean vorticity in the flow is concentrated along spanwise rollers aligned with dune crestlines, it is also evident that the space between successive rollers is occupied by weaker, albeit clearly defined, streamwise counter-rotating streaks of vorticity. The streamwise streaks that are close to the channel walls are more coherent and persistent since they are the result of well-known corner eddies in open channels (Yalin 1992; Nezu & Nakagawa 1993). In the centre of the channel, however, the streamwise streaks are shorter and span the distance between successive rollers. We argue that such streaks are associated with the streamwise vorticity concentrated in the legs of horseshoe vortices that are stretched in the space between adjacent crestlines as also revealed by the instantaneous Q isosurfaces shown in figure 29.

5.3.1. *Sand wave dynamics*

In this section, we focus our attention on quantifying the statistical properties of the simulated sand waves as well as examining the spectral characteristics of the simulated flow velocity fields over an active mobile sand bed. Previous work has shown that sand waves in numerical simulations, in laboratory experiments and in nature obey universal scaling laws. For instance, spectral analysis of the topography in experimental data has revealed power-law relations of the frequency spectra, with exponents of f^{-2} and f^{-3} for high and low frequencies, respectively (Hino 1968; Jain & Kennedy 1974). The root-mean-square (RMS) of bed elevation fluctuations sampled over a range of length scales has also been shown to exhibit a power scaling law (Jerolmack & Mohrig 2005*c*,*a*,*b*; Escauriaza & Sotiropoulos 2011*a*), which can be related to the roughness of the evolving bed (Barabási & Stanley 1995). Finally, recent laboratory measurements of turbulent flow over mobile beds showed that the

spectra of velocity fluctuations above the bed exhibit a distinct 'spectral gap', which delineates energetic low-frequency structures in the flow linked to migrating bedforms from turbulence in the flow (Van Der Hoven 1957; Singh *et al.* 2010). In this section we show that our simulated sand waves and flow fields exhibit all these important characteristics.

Following Jerolmack & Mohrig (2005*c*) and Escauriaza & Sotiropoulos (2011*a*), we evaluate the *rms* of the computed bed elevation as a function of the length scale Δs along the centreline s of the channel. The details of this so-called fluctuation approach can be found in Escauriaza & Sotiropoulos (2011*a*) (see also Chrisohoides & Sotiropoulos 2003) and for that reason only a brief summary is presented here. For a given instant in time t, we sample the bed elevation series along the channel centreline $z = z(s)$ using a filter width Δs and compute the RMS of the bed elevation as a function of Δs as follows:

$$z'_{\Delta s} = \left[\frac{1}{N} \sum_{i=1}^{N} (z_i - \bar{z}_b)^2 \right]^{1/2}, \tag{5.4}$$

where z_i is the bed elevation at the ith point along the channel centreline, $\bar{z}_b$ is the averaged bed elevation along the centreline, and N is the total number of data points along the centreline at intervals of Δs.

The scale invariance of the spatial fluctuations produced by the bedform geometry determines an increase in magnitude with the length scale of $z'_{\Delta s}$. This relation is also similar to the definition of the roughness exponent on the RMS diagram of Barabási & Stanley (1995). We thus define the statistic $\mathfrak{I}_{\Delta s}$ to quantify the scaling of the variation of the bed RMS with Δs (Escauriaza & Sotiropoulos 2011*a*):

$$\mathfrak{I}_{\Delta s} = z'_{\Delta s} \sqrt{\Delta s} \sim (\Delta s)^{\vartheta}. \tag{5.5}$$

The scale at which $\mathfrak{I}_{\Delta s}$ deviates from the above power-law relation represents the approximate maximum spatial window size at which the spatial correlation of the bedforms is maintained (Escauriaza & Sotiropoulos 2011*a*). As seen in figure 34, for our case and at time $t = 150$ s, when we apply the above fluctuation analysis, the bed elevation fluctuations remain correlated up until $\Delta s \approx 0.05$ m. This coherence length scale of sand waves coincides with the average length of measured (Venditti & Church 2005) and computed sand waves in the time period of $0 < t < 200$ s. Sand waves of smaller length scale remain correlated and self-similar, with a roughness exponent $\vartheta = 0.5$. This exponent is identical to that determined by Escauriaza & Sotiropoulos (2011*a*) for ripples developing inside the scour hole in the junction of a circular cylinder with a mobile sand bed.

In figure 35 we plot the temporal variation of the spatial standard deviation of the bed elevation $z = z(s, t)$ along s obtained on all four grid systems that we employed in this work. Since bedforms cannot grow indefinitely, we anticipate reaching an equilibrium steady state consistent with the continuous generation of bedforms at a statistically converged wavelength and amplitude. As seen in figure 35, and regardless of the grid system used, the resulting variation of $\sigma(t)$ exhibits three distinct scaling regimes of bedform development. In the first regime, when the bed evolves from the flat bed condition to cross-hatch patterns, $\sigma(t)$ increases as $t^{0.5}$ (see figure 35). Subsequently, the chevron-shaped and subsequent features evolve much faster and $\sigma(t)$ grows rapidly as t^{10}, which is one order of magnitude larger than the previous stage. This trend continues until the entire bed surface is covered with sand

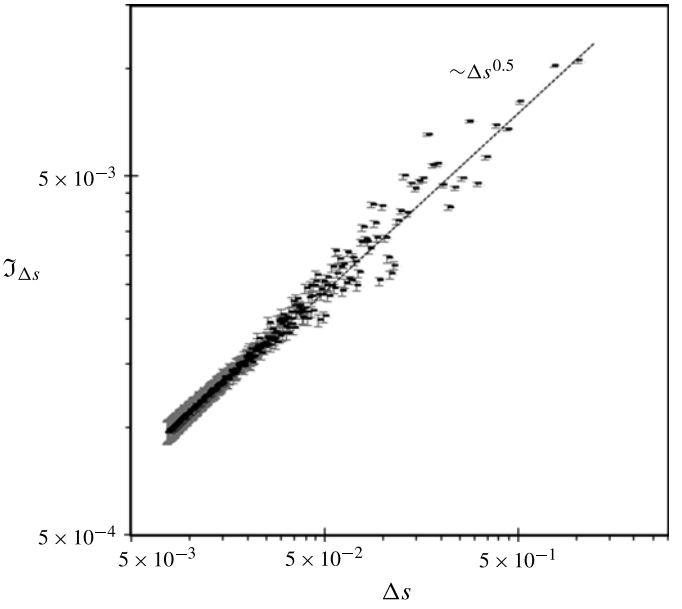

FIGURE 34. Statistics of bed elevation along the centreline that shows the fluctuation diagram averaged over time (5.5). The error bars are associated with the standard deviation of $\Im_{\Delta s}$ and spatial window size Δs is in metres. The straight line marks the 0.5 slope.

waves. Later a new regime appears at which self-similar 2D and/or 3D bedforms migrate downstream in a periodic manner. The much slower evolution of the standard deviation at this last regime explains the approximately constant slope of 0.5 in the fluctuation diagram shown in figure 35. Even though all four grid systems show a similar trend of sand wave development, the coarse grid simulation (grid A) exhibits a time lag of approximately 100 s, which has already been discussed and explained in a previous section. Overall, a figure like figure 35 can serve as a statistical measure for quantifying the grid sensitivity of the computed bedforms.

In figure 36 we also plot the frequency spectrum of bed elevation fluctuations at the centre of the channel. The figure shows that in the low frequency range, corresponding to the larger slowly migrating dunes, the spectrum exhibits -1 decay, while for the high frequency range, corresponding to small-scale sand waves, the spectrum coincides with the approximately -2 power-law relation. This rate of spectral decay for small-scale sand waves agrees reasonably well with what has been observed before in laboratory experiments and numerical simulations. Using experimental data, Hino (1968) showed that the frequency spectrum of bedforms has a power-law relation with a decay of f^{-2} for low frequencies near the peak of the spectrum, and argued that the -2 power law was mainly associated with the dynamics of ripples. The numerical simulations of Escauriaza & Sotiropoulos (2011*a*) showed the same -1 and -2 slopes for the high and low frequency ranges of the spectrum, respectively, for sand waves developing around a cylindrical pier. The recent experiments of Singh *et al.* (2010) also showed the -2 slope for bedforms in a large-scale gravel-bed experimental flume. We note that the reason our simulations cannot maintain the -2 slope spectrum at even higher frequencies is that the solution of the Exner–Polya equation in our model is based on a dissipative second-order scheme for the spatial derivatives, which, in the absence of a subgrid model for the

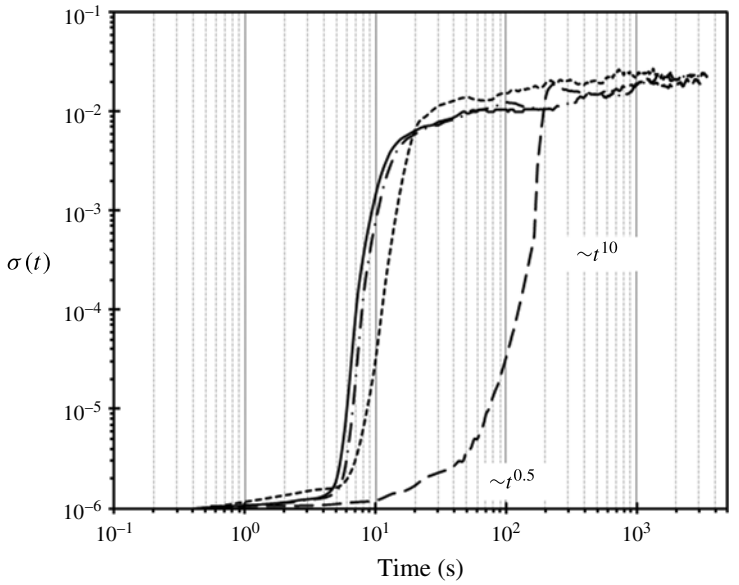

FIGURE 35. Evolution of the standard deviation of the bed elevation in time calculated along the channel centreline. The dashed, dotted, dotted-dashed and solid lines represent the simulation results on grid systems A, B, C and D, respectively.

fluctuations of the bed elevation, tends to smooth high-frequency features of the bed elevation.

Finally we turn our attention to the spectra of the velocity fluctuations in the flow that arise in a channel with slowly evolving bedforms. Compared to a turbulent flow over fixed roughness elements, in which turbulence is the only source of velocity fluctuations, a distinct characteristic of a turbulent flow over moving bedforms is that it is modulated by the very slowly evolving bed topography. In the present case, sand waves propagate with an average velocity that is less than 0.5 % of the bulk flow, and this slow evolution of the bed introduces additional velocity fluctuations at the very slow temporal scales associated with bedform migration. Singh *et al.* (2010) recently showed that the velocity spectra in a gravel mobile bed open channel exhibit a clear spectral gap delineating the low-frequency fluctuations associated with the migrating bedforms from the higher-frequency fluctuations associated with turbulence. The experiment of Singh *et al.* (2010) considered bedforms with amplitude as high as 10 cm developing in turbulent open channel flow with a very high Reynolds number $Re = 10^6$. They argued that the underlying physical causes for the spectral gap in their measurements are similar to the well-known spectral gap in atmospheric turbulent boundary layers (Van Der Hoven 1957), where the gap separates energy contributions due to turbulence from those due to very slow mesoscale and diurnal variability in the atmosphere. In figure 37 we plot the calculated velocity spectra at three elevations above the bed. It is seen that all three spectra exhibit scaling regimes separated by a region of a clearly defined flat spectral gap: (i) the low-frequency f^{-1} scaling due to migrating bedforms; and (ii) the characteristic spectrum of turbulence with the f^{-1} and $f^{-5/3}$ regions. It is also evident from figure 37 that in our simulations the width of the spectral gap increases with distance from the wall. Singh *et al.* (2010) reported velocity measurements at only one elevation above the bed but hypothesized

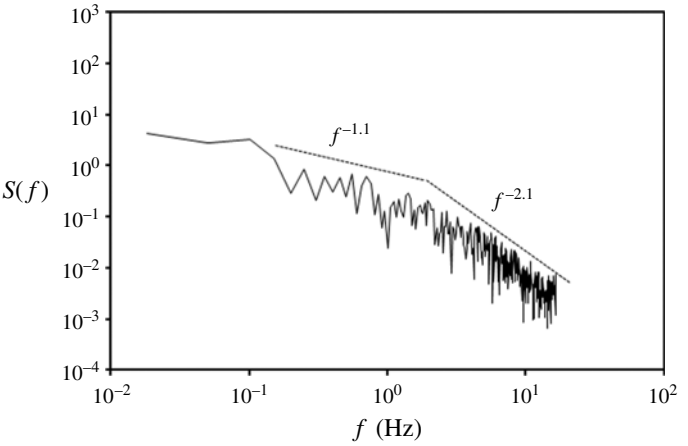

FIGURE 36. Frequency spectrum of bed elevation fluctuations at the centre point of the channel.

that the width of the spectral gap should increase with distance from the bed surface. This is because the right (high-frequency) end of the spectral gap is associated with the integral time scale of turbulence (the scale of the largest turbulent eddies in the flow) while the (left) low-frequency end of the spectral gap is associated with velocity fluctuations contributed by the smallest bedforms. For turbulent boundary layers, however, eddies of vertical size smaller than the distance to the surface z do not produce a signature in the velocity spectra at height z (Venugopal *et al.* 2003). Therefore, the smaller the distance from the bed at which the velocity sensor is placed, the better it is able to resolve velocity fluctuations by the smallest bedforms, thus extending the low-frequency end of the spectral gap to the right into higher frequencies as the bed is approached and causing the width of the gap to be reduced. This is clearly evident in the calculated spectra in figure 37, which show that, while the right end of the spectral gap is fixed at approximately 1 Hz (the frequency of the largest eddies in our case), its left end is displaced further to the right into higher frequencies as the distance from the bed is decreased. To the best of our knowledge, this is the first time that the experimentally observed spectral gap has been simulated numerically. Moreover, our simulations confirm the hypothesis of Singh *et al.* (2010) regarding the relationship between the width of the spectral gap and the distance of the velocity probe from the bed.

Regarding the spectra shown in figure 37, the apparent good resolution of the LES is due to the fact that the spectra shown in this figure have been computed at a time when very large-scale sand waves are present on the bed (during the 3D stage of sand wave evolution when $\Delta \sim H/3$). When bedforms grow to be so large, the large-scale energetic coherent structures shed from their crestlines dominate turbulence production and can be apparently resolved quite well on a grid like grid C that we have employed.

6. Summary and conclusions

We developed a LES approach for carrying out coupled hydro-morphodynamic simulations of turbulent flow in open channels with a mobile sand bed. The numerical formulation can handle sand waves of arbitrary geometrical complexity, accounts

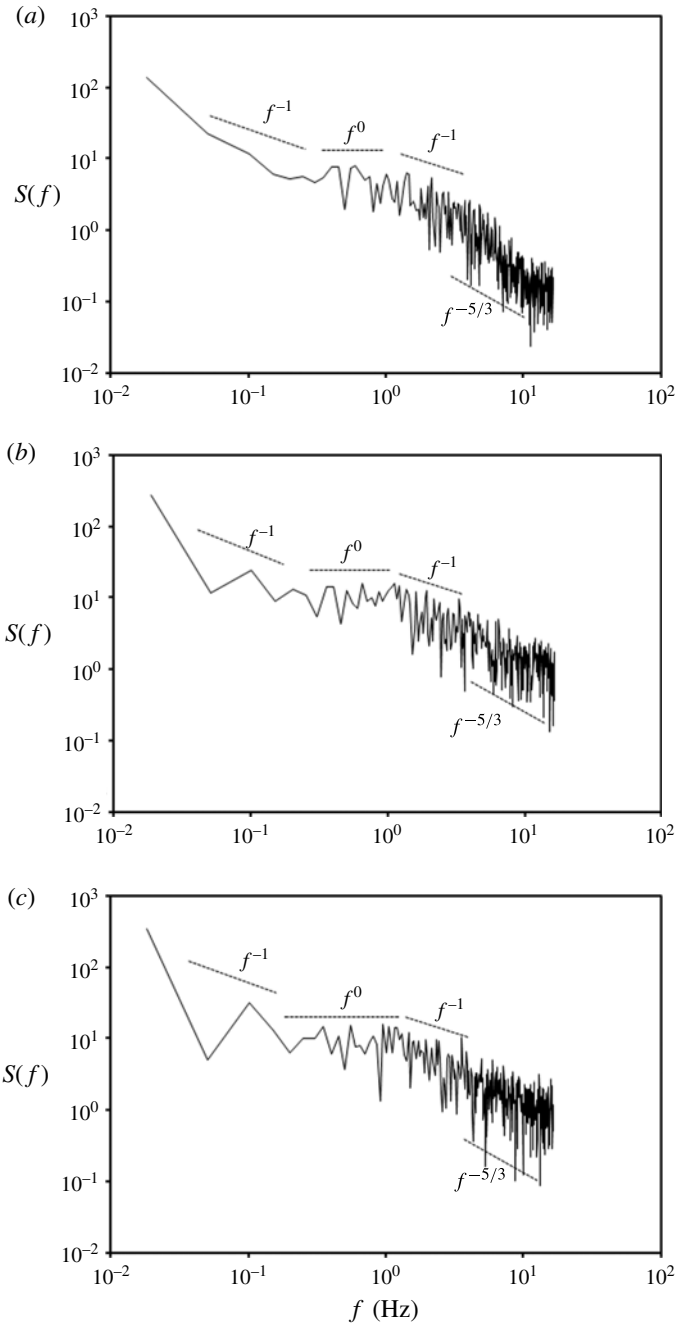

FIGURE 37. Calculated frequency spectrum of velocity fluctuations at (*a*) the leading edge of the bedload layer where $z = 2d_{50}$ above the bed surface, (*b*) $z = 5d_{50}$ above the bed surface and (*c*) $z = 10d_{50}$ above the bed surface. The time series are probed at the centre point of the channel during the 3D stage of the sand wave development when $\Delta \sim H/3$.

for stratified flow effects through the Boussinesq assumption, and can simulate both bedload and suspended sediment transport processes. The method was applied to simulate the case studied experimentally by Venditti & Church (2005), who

investigated sand wave initiation, growth and migration in a sand bed open channel with sediment recirculation.

We carried out systematic grid refinement studies and showed that a sufficiently refined mesh near the bed is required in order to correctly capture the sand wave dynamics, especially during the early stages of bed instability when small-scale features develop on the initially flat bed. The computed results reproduced with reasonable accuracy the various stages of sand wave initiation and development, including the initial appearance of linear cross-hatch patterns, the growth of chevron features, the emergence of incipient crestlines and the ultimate appearance of fully grown 2D and 3D bedforms.

One discrepancy between the simulation results and experimental observations is with regard to the time scale of various stages of sand wave development, which are slightly under-predicted in our simulations. We argued that one reason for the faster development of simulated sand waves is an important difference between the experimental and computational set-ups during the early stages of the process. In the former, the flow discharge was gradually increased over a period of 60 s from zero to the target experimental value, while in the simulations, the flow was assumed to be fully developed from the start of the simulation. Another difference between the observed and simulated bedforms was that in the simulation a 2D stage, with nearly straight crestlines perpendicular to the flow direction, was not observed as clearly as in the experiment. Even though in the experiments truly 2D bedforms were also never quite realized, a stage with rather organized spanwise structures did appear. We argued that this difference is due to the shorter domain that we used in the simulation, which did not allow sufficient distance for disturbances introduced at the inlet of the domain due to the continuous recirculation of sediment to diminish and triggered sooner the onset of the 3D phase. In other words, the discrepancy in capturing the 2D stage of the sand wave evolution in this work can also be attributed to the short length of the simulated channel (3.5 m) while the experimental facility is approximately 10 m long (Venditti & Church 2005). The reason for such a choice, however, is dictated by the enormous computational cost that would be required to simulate the entire length of the experimental channel. This important issue can be explored further via additional simulations with longer domains. These discrepancies notwithstanding, however, the computed sand waves captured most of the experimentally observed features with good accuracy, including the complex topologies emerging during the continuous rearrangement of crestlines.

Our simulations provided important insights into the coupling between migrating bedforms and the turbulent stratified flow in the open channel. By carrying out systematic numerical experiments, turning on and off the Boussinesq terms in the Navier–Stokes equations, we showed that, when the grid is sufficiently refined in the near-wall region, stratification effects do not play a role during the initial stages of the bed instability. Rather, the initial cross-hatch patterns that appear on the bed at the very start of the process are closely correlated with the structure of the fluctuating near-bed sweep events just before the bed is destabilized. Stratification effects do become important, however, at later stages of the process, when near-bed coherent structures are able to entrain sediment into suspension, creating a highly heterogeneous stratified layer above the bed, which modifies the structure of turbulence and the sediment dynamics. Our findings, therefore, are in agreement with and help explain the experimental measurements of Venditti & Church (2005), who showed that the size of near-bed coherent structures on the initially flat bed essentially coincides with the average length of the lines of cross-hatch that develop in the bed. They also help

reconcile previously presented arguments in the literature regarding the relative importance of near-bed coherent structures and stratification-related instabilities in destabilizing the bed (Grass 1970, 1971; Coleman & Melville 1994; Best & Kostaschuk 2002; Venditti *et al.* 2006). Both mechanisms are important at different stages of the process.

While recent numerical simulations of turbulent flow over frozen 3D dunes (Omidyeganeh & Piomelli 2013*a*,*b*) captured the previously hypothesized horseshoe vortical structures emanating from crestlines and rising up towards the surface, our work is the first to simulate the evolution of these structures starting from a flat bed condition. As bedforms develop and grow, spanwise vortical rollers form that are aligned with crestlines. As crestlines become distorted in the spanwise direction, these rollers evolve into horseshoes, which ultimately grow sufficiently strong to rise to the free surface. These structures transport both low-momentum near-bed fluid and suspended sediment giving rise to the distinct 'boils' that are observed on the water free surface. As a result of such rich coherent structure dynamics, the mean vorticity field (averaged over an interval long enough for obtaining turbulence statistics but short enough compared to the time scale of bed evolution) is shown to consist of rollers of spanwise vorticity aligned with crestlines with streamwise streaks of axial vorticity spanning the space between rollers. By analysing the instantaneous vorticity magnitude field at the free surface, we showed that it contains embedded in it distinct signatures associated with the characteristics of the migrating bedforms. This is also true for other flow quantities, such as the flow velocity field at the free surface, thus pointing to the conclusion that it may be possible to extract information about the characteristics and dynamics of bedforms from resolved velocity measurements at the free-surface.

Spectral and statistical analysis of the calculated time series of bed elevation demonstrate that the calculated bedforms exhibit scaling laws that are similar to those observed in experiments and in the field. The temporal variation of the standard deviation of bed elevation time series in particular revealed a triple regime of bedform development. During the first regime, the bed evolves from flat bed condition to cross-hatch pattern at a slow, $t^{0.5}$, rate. Afterwards the chevron-shaped features start to evolve in time at a rate that is approximately 20 times faster than in the previous stage. This trend continues until the organized quasi-2D bedforms appear, which gradually grow in amplitude and length until a new regime appears during which the self-similar 3D bedforms migrate downstream at a very slow rate.

Spectra of velocity fluctuations at various locations above the mobile bed revealed the existence of a distinct spectral gap that delineates the spectrum of turbulence in the flow from that associated with low-frequency energetic coherent motions modulated by the slowly migrating bedforms. These results confirm for the first time recent experimental findings of Singh *et al.* (2010), who reported the existence of a spectral gap in a flow with much higher Reynolds number ($Re = 10^6$) in an open channel with a mobile gravel bed. Our results also show that the width of the spectral gap increases with the distance from the bed, thus providing the first confirmation of the hypothesis first put forth by Singh *et al.* (2010). This is because, while the high-frequency end of the spectral gap is fixed, since it depends on the integral scale of turbulence, the low-frequency end depends on the ability of the velocity sensor to resolve fluctuations associated with the smallest bedforms, which decreases with the distance from the bed. The spectral gap was first observed in atmospheric flows (Van Der Hoven 1957) and was attributed to the large disparity of time scales between turbulent eddies in the boundary layer and very slow mesoscale and diurnal variations in the atmosphere.

In a turbulent boundary layer over a mobile bed with migrating bedforms, such clear separation of scales occurs because the average velocity of bedform migration is less than 1 % of the bulk velocity of the flow and thus the time scale of eddies modulated by the bedforms and the integral time scale of turbulence in the flow vary across two orders of magnitude. Therefore, our results suggest that LES over frozen bedforms, such as those reported by Omidyeganeh & Piomelli (2013*b*), constitutes a viable and more economical approach to study the structure of turbulence during various stages of bedform development. The coupled hydro-morphodynamic method we have developed herein can be used to obtain realistic 3D sand wave topologies, which can then be used as input to high-resolution LES to study the details of the turbulent flow over the frozen bed and during various stages of sand wave development.

A limitation of the morphodynamic model that we have developed herein is that it is based on sediment entrainment and bedload flux relations that have been empirically correlated to the mean shear stress. In our work, as in previous studies (Chou & Fringer 2010; Escauriaza & Sotiropoulos 2011*a*), we have assumed these correlations to be valid for instantaneous sediment and flow quantities. While there is no rigorous physical argument for supporting the validity of this assumption, the results we have obtained suggest that the proposed model can yield results that exhibit a great deal of physical realism. Models that can incorporate instantaneous flow quantities to calculate sediment entrainment have been proposed by Escauriaza & Sotiropoulos (2011*b*), who developed a transport equation for the sediment particle velocity within the bedload layer based on instantaneous forces acting on particles, and Coleman & Nikora (2008, 2009), who proposed a volumetric momentum balance approach. The hydro-morphodynamic model we have developed herein presents a framework within which the performance of such models can be systematically evaluated relative both to each other and to the empirical sediment transport relations we have incorporated in this paper. Such evaluation, however, needs to be accompanied by laboratory experiments able to resolve the effects of fluctuating flow forces on the motion of sediment grains (e.g. Diplas *et al.* 2008).

Acknowledgements

This work was supported by NSF Grants EAR-0120914 (as part of the National Center for Earth-Surface Dynamics) and EAR-0738726, and National Cooperative Highway Research Program Grant NCHRP-HR 24–33. Computational resources were provided by the University of Minnesota Supercomputing Institute. Valuable collaborations with Professor J. Venditti from Fraser University that provided us with the experimental data are also greatly appreciated.

REFERENCES

ALLEN, J. R. L. 1968 *Current Ripples: Their Relation to Patterns of Water and Sediment Motion*. p. 433. North-Holland.

ALLEN, J. R. L. 1971 Bed forms due to mass transfer in turbulent flows: a kaleidoscope of phenomena. *J. Fluid Mech.* **49**, 49–63.

ANDREOTTI, B., CLAUDIN, P., DEVAUCHELLE, O., DURÁN, O. & FOURRIÈRE, A. 2011 Bedforms in a turbulent stream: ripples, chevrons and antidunes. *J. Fluid Mech.* **690**, 94–128.

ANDREOTTI, B., CLAUDIN, P. & DOUADY, S. 2002 Selection of dune shapes and velocities, Part 1: Dynamics of sand, wind and barchans. *Eur. Phys. J.* B **28**, 321–329.

ANGELIS, V. D., LOMBARDI, P. & BANERJEE, S. 1997 Direct numerical simulation of turbulent flow over a wavy wall. *Phys. Fluids* **9**, 2429–2442.

ASHLEY, G. M. 1990 Classification of large-scale subaqueous bedforms: a new look at an old problem. *J. Sedim. Petrol.* **60**, 160–172.

BARABÁSI, A. L. & STANLEY, H. E. 1995 *Fractal Concepts in Surface Growth*. Cambridge University Press.

BARR, B. C., SLINN, D., PIERO, T. & WINTERS, K. 2004 Numerical simulation of turbulent, oscillatory flow over sand ripples. *J. Geophys. Res.* **109**, C09009.

BESIO, G., BLONDEAUX, P. & VITTORI, G. 2006 On the formation of sand waves and sand banks. *J. Fluid Mech.* **557**, 1–27.

BEST, J. 2005 The fluid dynamics of river dunes: a review and some future research directions. *J. Geophys. Res.* **119**, 1–21.

BEST, J. & KOSTASCHUK, R. A. 2002 An experimental study of turbulent flow over a low-angle dune. *J. Geophys. Res.* **107** (C9), 3135.

BLONDEAUX, P. 2001 Mechanics of coastal forms. *Annu. Rev. Fluid Mech.* **33**, 339–370.

BLONDEAUX, P. & VITTORI, G. 1991 Vorticity dynamics in an oscillatory flow over a rippled bed. *J. Fluid Mech.* **226**, 257–289.

BORAZJANI, I., GE, L. & SOTIROPOULOS, F. 2008 Curvilinear immersed boundary method for simulating fluid structure interaction with complex 3D rigid bodies. *J. Comput. Phys.* **227**, 7587–7620.

BUCHER, W. H. 1919 On ripples and related sedimentary surface forms and their paleogeographic interpretation. *Am. J. Sci.* **47**, 149–210.

CELIK, I. & RODI, W. 1988 Modeling suspended sediment transport in non-equilibrium situations. *J. Hydraul. Engng ASCE* **114** (10), 1157–1191.

CHANG, Y. S. & SCOTTI, A. 2003 Entrainment and suspension of sediments into a turbulent flow over ripples. *J. Turbul.* **4** (19), 1–22.

CHANG, Y. S. & SCOTTI, A. 2004 Modeling unsteady turbulent flows over ripples: Reynolds-averaged Navier–Stokes equations (RANS) versus large-eddy simulation (LES). *J. Geophys. Res.* **109**, C09012.

CHARRU, F., ANDREOTTI, B. & CLAUDIN, P. 2013 Sand ripples and dunes. *Annu. Rev. Fluid Mech.* **45**, 469–493.

CHAU, L. & BHAGANAGAR, K. 2012 Understanding turbulent flow over ripple-shaped random roughness in a channel. *Phys. Fluids* **24**, 115102.

CHOU, Y. J. & FRINGER, O. B. 2008 Modeling dilute sediment suspension using large-eddy simulation with a dynamic mixed model. *Phys. Fluids* **20**, 115103.

CHOU, Y. J. & FRINGER, O. B. 2010 A model for the simulation of coupled flow–bed form evolution in turbulent flows. *J. Geophys. Res.* **115**, C10041.

CHRISOHOIDES, A. & SOTIROPOULOS, F. 2003 Experimental visualization of Lagrangian coherent structures in aperiodic flows. *Phys. Fluids* **15**, L25–L28.

COCO, G., MURRAY, A. B., GREEN, M. O., THIELER, E. R. & HUME, T. M. 2007 Sorted bed forms as self-organized patterns: 1. Model development. *J. Geophys. Res.* **112**, F03015.

COLEMAN, S. E. & FENTON, J. D. 2000 Potential-flow instability theory and alluvial stream bed forms. *J. Fluid Mech.* **418**, 101–117.

COLEMAN, S. E. & MELVILLE, B. W. 1994 Bed form development. *J. Hydraul. Engng* **120**, 544–560.

COLEMAN, S. E. & NIKORA, V. I. 2008 A unifying framework for particle entrainment. *Water Resour. Res.* **44**, W04415.

COLEMAN, S. E. & NIKORA, V. I. 2009 Exner equation: a continuum approximation of a discrete granular system. *Water Resour. Res.* **45**, W09421.

COLEMAN, S. E., NIKORA, V. I., MCLEAN, S. R., CLUNIE, T. M., SCHLICKE, T. & MELVILLE, B. W. 2006 Equilibrium hydrodynamics concept for developing dunes. *Phys. Fluids* **18**, 105104.

COLOMBINI, R. M. 2004 Revisiting the linear theory of sand dune formation. *J. Fluid Mech.* **502**, 1–16.

COLOMBINI, M. & STOCCHINO, A. 2012 Three-dimensional river bed forms. *J. Fluid Mech.* **695**, 63–80.

DARGAHI, B. 1989 The turbulent flow field around a circular cylinder. *Exp. Fluids* **8**, 1–12.

DARGAHI, B. 1990 Controlling mechanism of local scouring. *J. Hydraul. Engng* **116** (10), 1197–1214.

DIPLAS, P., DANCEY, C. L., CELIK, A. O., VALYRAKIS, M., GREER, K. & AKAR, T. 2008 The role of impulse on the initiation of particle movement under turbulent flow conditions. *Science* **322** (5902), 717–720.

DREANO, J., VALANCE, A., LAGUE, D. & CASSAR, C. 2010 Experimental study on transient and steady-state dynamics of bedforms in supply limited configuration. *Earth Surf. Process. Landf.* **35** (14), 1730–1743.

ESCAURIAZA, C. & SOTIROPOULOS, F. 2011*a* Initial stages of erosion and bed-form development in turbulent flow past a bridge pier. *J. Geophys. Res.* **116**, F03007.

ESCAURIAZA, C. & SOTIROPOULOS, F. 2011*b* Lagrangian dynamics of bedload transport in turbulent junction flows. *J. Fluid Mech.* **666**, 36–76.

FREDSOE, J. 1974 On the development of dunes in erodible channels. *J. Fluid Mech.* **60**, 1–16.

GE, L. & SOTIROPOULOS, F. 2007 A numerical method for solving the 3D unsteady incompressible Navier–Stokes equations in curvilinear domains with complex immersed boundaries. *J. Comput. Phys.* **225**, 1782–1809.

GERMANO, M., PIOMELLI, U., MOIN, P. & CABOT, W. H. 1991 A dynamic subgrid-scale eddy viscosity model. *Phys. Fluids* A **3** (7), 1760–1765.

GILMANOV, A. & SOTIROPOULOS, F. 2005 A hybrid Cartesian/immersed boundary method for simulating flows with three-dimesional, geometrically complex, moving bodies. *J. Comput. Phys.* **207** (2), 457–492.

GIRI, S. & SHIMIZU, Y. 2006 Numerical computation of sand dune migration with free surface. *Water Resour. Res.* **42** (10), W10422.

GIRI, S. & SHIMIZU, Y. 2007 Validation of a numerical model for flow and bedform dynamics. *Annu. J. Hydraul. Engng, Jpn. Soc. Civ. Engng* **51**, 139–144.

GRASS, A. J. 1970 Initial instability of fine bed sand. *J. Hydraul. Div. ASCE* **HY3**, 619–632.

GRASS, A. J. 1971 Structural features of turbulent flow over smooth and rough boundaries. *J. Fluid Mech.* **50**, 233–255.

GYR, A. & SCHMID, A. 1989 The different ripple formation mechanism. *J. Hydraul. Res.* **27**, 61–74.

HANSEN, J., VAN HECKE, M., HAANING, A., ELLEGAARD, C., ANDERSEN, K., BOHR, T. & SAMS, T. 2001 Pattern formation: instabilities in sand ripples. *Nature* **410**, 324.

HAYASHI, T. 1970 Formation of dunes and antidunes in open channels. *J. Hydraul. Engng* **96**, 357–366.

HENN, D. & SYKES, R. I. 1999 Large-eddy simulation of flow over wavy surfaces. *J. Fluid Mech.* **383**, 75–112.

HINO, M. 1968 Equilibrium-range spectra of sand waves formed by flowing water. *J. Fluid Mech.* **34**, 565–573.

VAN DER HOVEN, I. 1957 Power spectrum of horizontal wind speed in the frequency range from 0.0007 to 900 cycles per hour. *J. Meteorol.* **14**, 160–194.

JACKSON, R. G. 1976 Sedimentological and fluid-dynamic implications of the turbulence bursting phenomenon in geophysical flows. *J. Fluid Mech.* **77**, 531–560.

JAIN, S. C. & KENNEDY, J. F. 1974 The spectral evolution of sedimentary bed forms. *J. Fluid Mech.* **63**, 301–314.

JEROLMACK, D. J. & MOHRIG, D. 2005*a* A unified model for subaqueous bedform dynamics. *Water Resour. Res.* **41**, W12421.

JEROLMACK, D. J. & MOHRIG, D. 2005*b* Formation of Precambrian sediment ripples. *Nature* **433**, 123–127.

JEROLMACK, D. J. & MOHRIG, D. 2005*c* Interactions between bed forms: topography, turbulence and transport. *J. Geophys. Res.* **110**, F02014.

JIANG, G. S. & SHU, C. W. 1996 Efficient implementation of weighted ENO schemes. *J. Comput. Phys.* **126** (1), 202–228.

DE JONG, B. 1989 Bed waves generated by internal waves in alluvial channels. *J. Hydraul. Engng* **115**, 801–817.

KANG, S., LIGHTBODY, A., HILL, C. & SOTIROPOULOS, F. 2011 High-resolution numerical simulation of turbulence in natural waterways. *Adv. Water Resour.* **34** (1), 98–113.

KANG, S. & SOTIROPOULOS, F. 2011 Flow phenomena and mechanisms in a field-scale experimental meandering channel with a pool–riffle sequence: insights gained via numerical simulation. *J. Geophys. Res.* **116**, F03011.

KANG, S. & SOTIROPOULOS, F. 2012 Assessing the predictive capabilities of isotropic, eddy-viscosity Reynolds-averaged turbulence models in a natural-like meandering channel. *Water Resour. Res.* **48**, W06505.

VON KÁRMÁN, T. 1947 Sand ripples in the desert. *Technion Yearbook* **6**, 52–54.

KENNEDY, J. F. 1969 The formation of sediment ripples, dunes and antidunes. *Annu. Rev. Fluid Mech.* **1**, 147–168.

KHELIFA, A. & OUELLET, Y. 2000 Prediction of sand ripple geometry under waves and currents ASCE. *J. Waterway Port Coast. Ocean Engng* **126** (1), 14–22.

KHOSRONEJAD, A. 2006 Three-dimensional numerical simulation of turbulent flow and sediment transport in dam reservoirs. PhD thesis, Tarbiat Modares University, Iran.

KHOSRONEJAD, A., HILL, C., KANG, S. & SOTIROPOULOS, F. 2013 Computational and experimental investigation of scour past laboratory models of stream restoration rock structures. *Adv. Water Resour.* **54**, 191–207.

KHOSRONEJAD, A., KANG, S., BORAZJANI, I. & SOTIROPOULOS, F. 2011 Curvilinear immersed boundary method for simulating coupled flow and bed morphodynamic interactions due to sediment transport phenomena. *Adv. Water Resour.* **34** (7), 829–843.

KHOSRONEJAD, A., KANG, S. & SOTIROPOULOS, F. 2012 Experimental and computational investigation of local scour around bridge piers. *Adv. Water Resour.* **37**, 73–85.

KHOSRONEJAD, A., KOZAREK, J. L. & SOTIROPOULOS, F. 2014 Simulation-based approach for stream restoration structure design: model development and validation. *J. Hydraul. Engng* **140** (7), 1–16.

KHOSRONEJAD, A., RENNIE, C., SALEHI, A. & TOWNSEND, R. 2007 3D numerical modeling of flow and sediment transport in laboratory channel bends. *J. Hydraul. Engng* **133** (10), 1123–1134.

KHOSRONEJAD, A., SALEHI, A. A. & RENNIE, C. 2008 Three dimensional numerical modeling of sediment release in a water reservoir. *J. Hydraul. Res.* **46** (2), 209–223.

KIDANEMARIAM, A. G. & UHLMANN, M. 2014 Direct numerical simulation of pattern formation in subaqueous sediment. *J. Fluid Mech.* **750**, 1–13.

KOSTASCHUK, R. A. 2000 A field study of turbulence and sediment dynamics over subaqueous dunes with flow separation. *Sedimentology* **47**, 519–531.

KRAFT, S., WANG, Y. & OBERLACK, M. 2011 Large eddy simulation of sediment deformation in a turbulent flow by means of level-set method. *J. Hydraul. Engng* **137** (11), 1394–1405.

LACY, J. R., RUBIN, D. M., IKEDA, H., MOKUDAI, K. & HANES, D. M. 2007 Bed forms created by simulated waves and currents in a large flume. *J. Geophys. Res.* **112**, C10018.

LIU, H. K. 1957 Mechanics of sediment-ripple formation. *J. Hydraul. Engng* **83**, 1–23.

MACVICAR, B. J., PARROTT, L. & ROY, A. G. 2006 A two-dimensional discrete particle model of gravel bed river systems. *J. Geophys. Res.* **111**, F03009.

MAZUMDER, B., PAL, D., GHOSHAL, K. & OJHA, S. 2009 Turbulence statistics of flow over isolated scalene and isosceles triangular-shaped bed forms. *J. Hydraul. Res.* **47** (5), 626–637.

DE MORAES FRANKLIN, E. 2013 Three-dimensional sand ripples as the product of vortex instability. *Appl. Math. Model.* **37**, 3193–3199.

MULLER, A. & GYR, A. 1986 On the vortex formation in the mixing layer behind dunes. *J. Hydraul Res.* **24**, 359–375.

NABI, M., DE VRIEND, H. J., MOSSELMAN, E., SLOFF, J. & SHIMIZU, Y. 2012 Detailed simulation of morphodynamics: 1. Hydrodynamic model. *Water Resour. Res.* **48**, W12523.

NEZU, L. & NAKAGAWA, H. 1993 *Turbulence in Open-Channel Flows*, IAHR Monograph. Balkema.

NIEMANN, S. L., FREDSØE, J. & JACOBSEN, N. G. 2011 Sand dunes in steady flow at low Froude numbers: dune height evolution and flow resistance. *J. Hydraul. Engng* **137** (1), 5–14.

NISHIMORI, H. & OUCHI, N. 1993 Formation of ripple patterns and dunes by wind-blown sand. *Phys. Rev. Lett.* **71**, 197–200.

NITTROUER, J. A., ALLISON, M. A. & CAMPANELLA, R. 2008 Bedload transport rates for the lowermost Mississippi River. *J. Geophys. Res.* **113**, F03004.

NITTROUER, J. A., MOHRIG, D. & ALLISON, M. A. 2011 Punctuated sand transport in the lowermost Mississippi River. *J. Geophys. Res.* **116**, F04025.

OMIDYEGANEH, M. & PIOMELLI, U. 2013*a* Large-eddy simulation of three-dimensional dunes in a steady, unidirectional flow. Part 1. Turbulence statistics. *J. Fluid Mech.* **721**, 454–483.

OMIDYEGANEH, M. & PIOMELLI, U. 2013*b* Large-eddy simulation of three-dimensional dunes in a steady, unidirectional flow. Part 2. Flow structures. *J. Fluid Mech.* **734**, 509–534.

PALMSTEN, M. L., KOZAREK, J. L., CALANTONI, J., KOONEY, T. & HOLLAND, K. 2011 Spatial and temporal evolution of stream bedforms. *AGU Fall Meeting Abstracts*, p. I1315.

PAOLA, C. & VOLLER, V. R. 2005 A generalized Exner equation for sediment mass balance. *J. Geophys. Res.* **110**, F04014.

RAUDKIVI, A. J. 1966 Bed forms in alluvial channels. *J. Fluid Mech.* **26**, 507–514.

RAUDKIVI, A. J. 2007 Transition from ripples to dunes. *J. Hydraul. Engng* **132**, 1316–1320.

RICHARDS, K. J. 1980 The formation of ripples and dunes on an erodible bed. *J. Fluid Mech.* **99**, 597–618.

VAN RIJN, L. C. 1984 Sediment transport, Part III: Bed forms and alluvial roughness. *J. Hydraul. Engng* **110** (12), 1733–1754.

VAN RIJN, L. C. 1993 *Principles of Sediment Transport in Rivers, Estuaries, and Coastal Seas*. Aqua Publications.

ROULUND, A., SUMER, B. M., FREDSOE, J. & MICHELSEN, J. 2005 Numerical and experimental investigation of flow and scour around a circular pile. *J. Fluid Mech.* **534**, 351–401.

SAGAUT, P. 1988 *Large Eddy Simulation for Incompressible Flows*. Springer.

SARKAR, S. & DEY, S. 2010 Double-averaging turbulence characteristics in flows over a gravel-bed. *J. Hydraul. Res.* **48**, 801–809.

SCANDURA, P. G., VITTORI, G. & BLONDEAUX, P. 2000 Three-dimensional oscillatory flow over steep ripples. *J. Fluid Mech.* **412**, 335–378.

SCHINDLER, R. J. & ROBERT, A. 2004 Suspended sediment concentration and the ripple–dune transition. *Hydrol. Process.* **18**, 3215–3227.

SEMINARA, G., COLOMBINI, M. & PARKER, G. 1996 Nearly pure sorting waves and formation of bedload sheets. *J. Fluid Mech.* **312**, 253–278.

SINGH, A., PORTÉ-AGEL, F. & FOUFOULA-GEORGIOU, E. 2010 On the influence of gravel bed dynamics on velocity power spectra. *Water Resour. Res.* **46**, 1–10.

SMAGORINSKY, J. S. 1963 General circulation experiments with the primitive equations. *Mon. Weath. Rev.* **91**, 99–164.

TJERRY, S. & FREDSØE, J. 2005 Calculation of dune morphology. *J. Geophys. Res.* **110**, F04013.

VENDITTI, J. G. & BAUER, B. O. 2005 Turbulent flow over a dune: Green River, Colorado. *Earth Surf. Process. Landf.* **30**, 289–304.

VENDITTI, J. G. & BENNETT, S. J. 2000 Spectral analysis of turbulent flow and suspended sediment transport over fixed dunes. *J. Geophys. Res.* **105**, 22035–22047.

VENDITTI, J. G. & CHURCH, M. A. 2005 Bed form initiation from a flat sand bed. *J. Geophys. Res.* **110**, F01009.

VENDITTI, J. G., CHURCH, M. A. & BENNETT, S. J. 2005*a* Morphodynamics of small-scale superimposed sand waves over migrating dune bed forms. *Water Resour. Res.* **41**, W10423.

VENDITTI, J. G., CHURCH, M. A. & BENNETT, S. J. 2005*b* On the transition between 2D and 3D dunes. *Sedimentology* **52**, 1343–1359.

VENDITTI, J. G., CHURCH, M. A. & BENNETT, S. J. 2006 On interfacial instability as a cause of transverse subcritical bed forms. *Water Resour. Res.* **42**, W07423.

VENUGOPAL, V., PORTÉ AGEL, F., FOUFOULA-GEORGIOU, E. & CARPER, M. 2003 Multiscale interactions between surface shear stress and velocity in turbulent boundary layers. *J. Geophys. Res.* **108** (D19), 4613.

WU, W., RODI, W. & WENKA, T. 2000 3D numerical modeling of flow and sediment transport in open channels. *J. Hydraul. Engng* **126** (1), 4–15.

YALIN, M. S. 1992 *River Mechanics*. Elsevier.

YUE, W., LIN, C. L. & PATEL, V. C. 2005 Coherent structures in open-channel flows over a fixed dune. *Trans. ASME: J. Fluids Engng* **127** (5), 858–864.

ZEDLER, E. A. & STREET, R. L. 2001 Large-eddy simulation of sediment transport: currents over ripples. *J. Hydraul. Engng* **127** (6), 444–452.

ZEDLER, E. A. & STREET, R. L. 2006 Sediment transport over ripples in oscillatory flow. *J. Hydraul. Engng* **132** (2), 1–14.

ZOU, L. Y., LIU, N. S. & LU, X. Y. 2006 An investigation of pulsating turbulent open channel flow by large eddy simulation. *Comput. Fluids* **35** (1), 74–102.